Synthese und Charakterisierung Morphologie-kontrollierter Cer-Zirconium Mischoxide

Synthesis and Characterization of Morphology-Controlled

Ceria-Zirconia Mixed Oxides

Kumulative Dissertation

zur Erlangung des akademischen Grades

„Doctor rerum naturalium“

– Dr. rer. nat. –

Eingereicht am Fachbereich

Biologie und Chemie

der

Justus-Liebig-Universität Gießen

von

Eric Prates da Costa

Gießen, Juli 2023

Man merkt nie, was schon getan wurde, man sieht immer nur, was noch zu tun bleibt.

Marie Curie

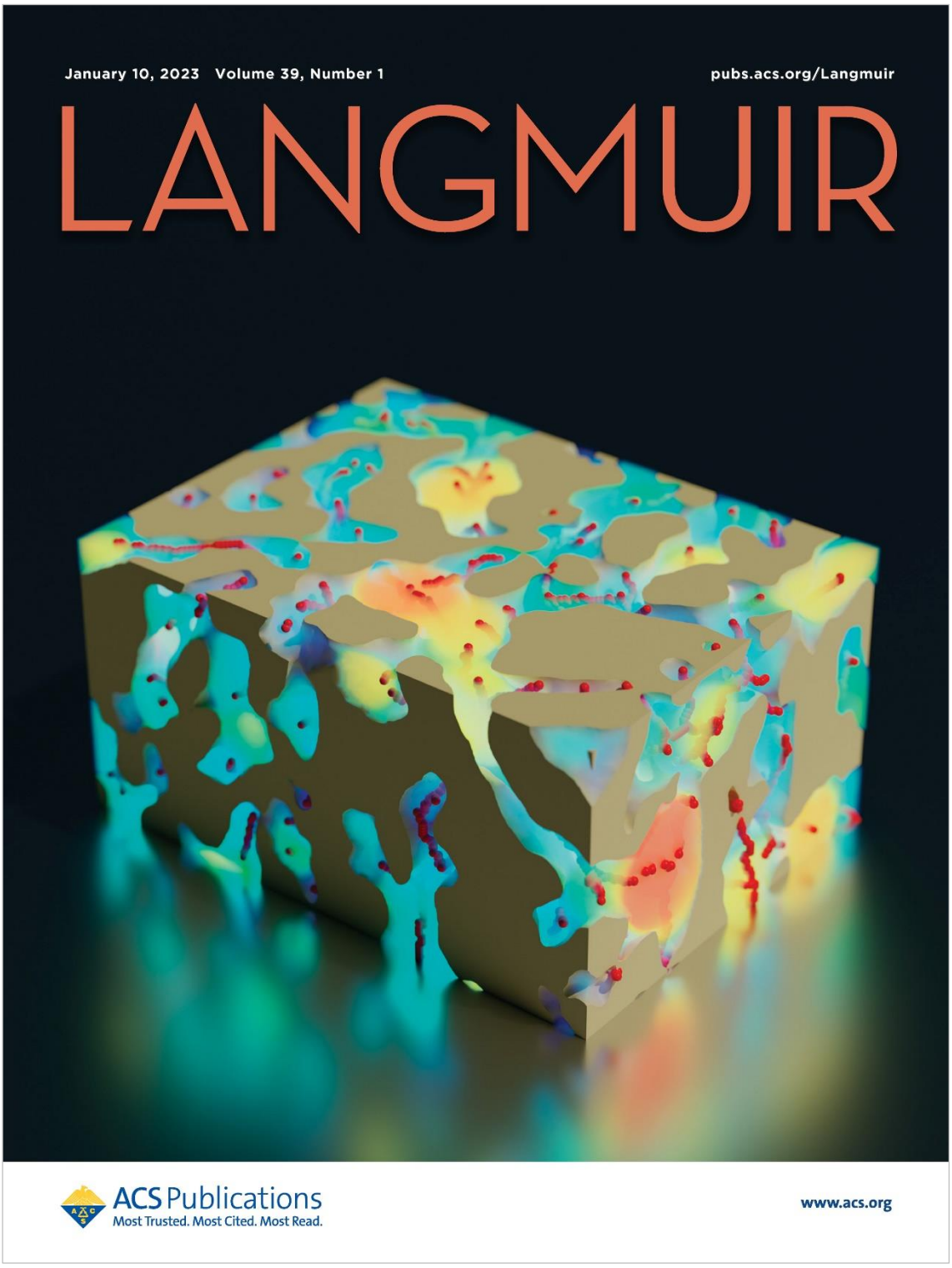

Erstgutachter: Prof. Dr. Bernd M. Smarsly

Zweitgutachter: Prof. Dr.-Ing. Maren Lepple

Selbstständigkeitserklärung

Ich erkläre:

Ich habe die vorgelegte Dissertation selbstständig und ohne unerlaubte fremde Hilfe und nur mit den Hilfen angefertigt, die ich in der Dissertation angegeben habe. Alle Textstellen, die wörtlich oder sinngemäß aus veröffentlichten Schriften entnommen sind, und alle Angaben, die auf mündlichen Auskünften beruhen, sind als solche kenntlich gemacht. Ich stimme einer evtl. Überprüfung meiner Dissertation durch eine Antiplagiat-Software zu. Bei den von mir durchgeführten und in der Dissertation erwähnten Untersuchungen habe ich die Grundsätze guter wissenschaftlicher Praxis, wie sie in der „Satzung der Justus-Liebig-Universität Gießen zur Sicherung guter wissenschaftlicher Praxis“ niedergelegt sind, eingehalten.

I declare:

I have completed this dissertation single-handedly without the unauthorized help of a second party and only with the assistance acknowledged therein. I have appropriately acknowledged and cited all text passages that are derived verbatim from or are based on the content of published work of others, and all information relating to verbal communications. I consent to the use of an anti-plagiarism software to check my thesis. I have abided by the principles of good scientific conduct laid down in the charter of the Justus Liebig University Giessen „Satzung der Justus-Liebig-Universität Gießen zur Sicherung guter wissenschaftlicher Praxis“ in carrying out the investigations described in the dissertation.

_____ _____

Ort, Datum Eric Prates da Costa

Danksagung

An dieser Stelle möchte ich mich bei all den Personen bedanken, die mich persönlich und fachlich auf meinem Werdegang unterstützt haben. Mein besonderer Dank gilt folgenden Personen:

- *Prof. Dr. Bernd Smarsly:* Ich danke Dir, dass ich seit 2017 Teil Deiner Arbeitsgruppe sein durfte und im Rahmen verschiedener Projekte, wie beispielsweise meine Bachelor- und Masterarbeit, viel lernen konnte. Ich bedanke mich für alle Deine Ideen, Ratschläge und Diskussionen, die mir bei meiner Forschung sehr geholfen und zum Entstehen dieser Dissertation beigetragen haben.
- *Dr. Ulrich Göbel:* Bei Dir möchte ich mich für die Umicore-seitige Betreuung meiner Promotion bedanken. Du warst mir mit Deiner Erfahrung ein wertvoller Ratgeber. Außerdem möchte ich mich dafür bedanken, dass Du stets alles ermöglicht hast, um meine Arbeit zu fördern.
- *Dr. Alexander Hofmann:* Ich möchte mich herzlich bei Dir für die Betreuung meiner Promotionsarbeit bedanken. Insbesondere Deine kritische Art nachzufragen und Dein kritisches aber stets konstruktives Feedback waren eine große Herausforderung aber auch eine wertvolle Hilfe.
- *Raoul „Rizzle" Brand:* Als mein langjähriger bester Freund möchte ich Dir für die letzten Jahre danken. Es war mir eine besondere Freude gemeinsam mit Dir zu studieren, nachdem wir uns nach der Grundschule für eine Weile aus den Augen verloren hatten. Ich werde die Zeit als Bürokollegen während der Promotion mit unseren winterlichen Teepausen und vielen Gesprächen über Filme und Videospiele sowie fachliches zur Physisorption sehr vermissen.
- *Sebastian Werner:* Bei Dir möchte ich mich für die vielen interessanten Gespräche über allerlei technische Dinge und die Physisorption bedanken. Du warst mit deiner Erfahrung immer eine Quelle für gute Ratschläge und Ideen, wodurch ich viel lernen konnte. Ich erinnere mich auch gerne an die endlos langen Nachtschichten auf der SAXS-Messzeit in Triest und unseren Kaffee mit Heinz nach dem „Beam Dump".

- *Kevin Turke:* Bei Dir möchte ich mich insbesondere für die Betreuung meiner Bachelor- und Masterarbeit bedanken. Als Mentor hast Du mir die Grundlagen der Physisorptionsanalyse beigebracht und so – wenn auch indirekt – zum Erfolg dieser Arbeit beigetragen.
- *Fabian Schmitz, Lysander Wagner, Aline Trommer, Paul Debes und Julia Schulze*: Euch danke ich für die vielen spannenden und oft lustigen Gespräche in den Mittagspausen oder bei anderen Gelegenheiten.
- *Dagmar Liebmann und Anja Stock:* Bei euch möchte ich mich für die angenehme Stimmung und die tatkräftige Unterstützung im Labor bedanken.

Außerdem möchte ich mich bei allen weiteren AG Mitgliedern und Kollegen bei Umicore für die angenehme Atmosphäre bedanken.

Auch meiner Familie, insbesondere meinen Eltern Maria und Nils und meiner Schwester Lena, möchte ich für die Unterstützung in allen Lebenslagen danken. Ohne euch wäre all dies nicht möglich gewesen.

Zuletzt möchte ich mich bei Lisa Brück (bald auch Prates da Costa) für unsere gemeinsamen 11 Jahre und all jene, die noch kommen werden, bedanken. Du hast mich immer unterstützt und mir auch in besonders schweren Zeiten viel Kraft, Halt und Motivation gegeben. Ich freue mich darauf, gemeinsam mit dir einen neuen Lebensabschnitt zu beginnen und mir bleibt an dieser Stelle nur noch zu sagen: „Ich liebe dich!“

Kurzfassung

Die Nachbehandlung von Abgasen aus Ottomotoren – die Drei-Wege Katalyse – stellt eines der größten Anwendungsgebiete mesoporöser CeO_2-basierter Sauerstoffspeichermaterialien dar. Deren Mesoporenmorphologie, welche maßgeblich über die zugrundeliegenden Syntheseparameter kontrolliert wird, hat dabei einen unmittelbaren Einfluss auf die katalytische Aktivität und thermische Stabilität der Katalysatoren. Die stattfindenden Reaktionen unterliegen diffusionskontrollierten Transportprozessen im Inneren des Porenraumes und hängen so direkt mit der Konnektivität der Poren im Netzwerk zusammen. Durch die starke thermische Beanspruchung der Materialien ist zudem eine hohe thermische Stabilität unerlässlich, um eine hohe Langzeitaktivität zu gewährleisten. Dies erfordert jedoch eine genaue Kenntnis der Zusammenhänge zwischen Syntheseparametern und resultierender Mesoporenstruktur und -konnektivität sowie der thermischen Degradierung. Um neue Synthesestrategien für mesoporöse Materialien mit hoher thermischer Stabilität zu entwickeln, beschäftigt sich diese Arbeit mit der Erforschung der Wirkung von Syntheseparametern auf die Mesoporenmorphologie komplexer CeO_2-basierter Mischoxide. Basierend auf einer literaturbekannten Hydrothermalsynthese wurden ungeordnet mesoporöse $Ce_xZr_{1-x-y-z}Y_yLa_zO_{2-\delta}$ Pulver hergestellt, und mittels „state-of-the-art“ Physisorptionsanalyse (inklusive Hysterese-Scanning) und Elektronentomographie in Abhängigkeit der Syntheseparameter und -schritte detailliert charakterisiert. Dabei konnte gezeigt werden, dass an die Oberfläche gebundene Nitratgruppen eine große Rolle bei der Entwicklung des Porenraumes während der Kalzinierung spielen. Bei niedrigen Temperaturen verlangsamen sie Sinterprozesse und verhindern so den Verlust von Porosität. Eine mildere Alternative zur Kalzinierung stellt eine zusätzliche hydrothermale Nachbehandlung der gebildeten Niederschläge in wässriger, basischer Lösung dar. Sie führt zu einer pH-abhängigen Erhöhung der thermischen Stabilität und Zugänglichkeit der Mesoporen durch Aufweitung der verbindenden Porenöffnungen. Die Interpretation der Ergebnisse aus Hysterese-Scanning Experimenten zur Konnektivitätsanalyse ungeordnet mesoporöser Festkörper stellt weiterhin eine besondere Herausforderung dar. Durch die Kombination mit Elektronentomographie liefert diese Arbeit jedoch einen Beitrag zu deren tiefergehendem Verständnis, welches die Basis für eine Etablierung der Methode als Standardverfahren darstellt.

Abstract

Aftertreatment of automotive exhausts of gasoline fueled engines – three-way catalysis – is a major field of application of mesoporous CeO_2-based oxygen storage materials. Their mesoporous structure, which is mainly controlled via the underlying synthesis parameters, has a direct impact on the catalyst's activity and thermal stability. The occurring reactions are governed by diffusion-controlled transport processes within the pore space and are, hence, directly affected by the pore connectivity. To withstand the high and fluctuating temperatures during operation high thermal stability is crucial to guarantee high long-time catalytic activity. However, this requires precise knowledge of the relationship between synthesis parameters and resulting mesopore morphology and connectivity as well as the behavior during thermal degradation. In order to develop novel synthesis strategies for mesoporous oxygen storage materials with high thermal stability, this work focuses on the investigation of the effect of synthesis parameters on the morphology of the mesopore space of complex CeO_2-based mixed oxides. Based on a literature known hydrothermal synthesis procedure, disordered mesoporous $Ce_xZr_{1-x-y-z}Y_yLa_zO_{2-\delta}$ powders were synthesized and characterized in detail by state-of-the-art physisorption analysis (including hysteresis scanning) and electron tomography in dependence of synthesis parameters and steps. The role of surface-bound nitrate groups in the development of the pore space during calcination was elucidated. It was shown that they slow down sintering processes at low temperatures, preventing the loss of porosity. As a mild alternative to calcination for the removal of remaining nitrates a hydrothermal aftertreatment process in aqueous ammonia solution was investigated. Such aftertreatment results in a pH-dependent increase of thermal stability and improved pore accessibility due to the widening of pore necks. The interpretation of hysteresis scanning experiments for the analysis of the pore connectivity in disordered mesoporous materials still is a challenge. Nonetheless, by combining hysteresis scanning with electron tomography this work provides a deeper understanding of the obtained scanning curves, presenting a basis for establishing this method as a standard procedure in material characterization.

Publikationen

Folgende Publikationen sind während meines Promotionsprojektes von 2019 bis 2023 entstanden:

1. **Prates da Costa, E.**, Hofmann, A., Göbel, U., Cop, P., Smarsly, B. M. Development of Pore Morphology During Nitrate Group Removal by Calcination of Mesoporous $Ce_xZr_{1-x-y-z}Y_yLa_zO_{2-\delta}$ Powders, *Langmuir* **2022**, *38*, 8342–8352. DOI: 10.1021/acs.langmuir.2c00875.

2. **Prates da Costa, E.**, Huang, X., Kübel, C., Cheng, X., Schladitz, K., Hofmann, A., Göbel, U., Smarsly, B. M. Effects of Hydrothermal Treatment on Mesopore Structure and Connectivity in Doped Ceria-Zirconia Mixed Oxides, *Langmuir* **2022**, 39, 177–191. DOI: 10.1021/acs.langmuir.2c02366.

3. **Prates da Costa, E.**, Huang, X., Kübel, C., Cheng, X., Schladitz, K., Hofmann, A., Göbel, U., Smarsly, B. M. Tuning Mesopore Accessibility of High Surface Area Doped Ceria-zirconia Mixed Oxides by Hydrothermal Posttreatment, s*ubmitted to Langmuir*.

4. Wagner, L. Q., **Prates da Costa, E.**, Glatthaar, C., Breckwoldt, F., Otto, S. K., Zecca, M., Centomo, P., Isse, A. A., Huang, X., Kübel, C., Schlaad, H., Kriechbaum, M., Amenitsch, H., Thommes, M., Smarsly, B. M. PEO-*b*-PHA Block Copolymers as Templates for Large Mesopore Sizes – a Detailed Porosity Analysis, *submitted to Chemistry of Materials*.

Die gewonnen Erkenntnisse wurden auf diesen Veranstaltungen vorgestellt:

Posterpräsentation

Prates da Costa, E., Göbel, U., Hofmann, A., Smarsly B. M., Synthesis and Characterization of $Ce_xZr_{1-x-y-z}Y_yLa_zO_{2-\delta}$ Oxygen Storage Materials for Application in Three-way Catalysis, Bunsentagung, Gießen, Deutschland. 2022

Posterpräsentation

Prates da Costa, E., Göbel, U., Hofmann, A., Smarsly B. M., Synthesis and Characterization of $Ce_xZr_{1-x-y-z}Y_yLa_zO_{2-\delta}$ Oxygen Storage Materials, Umicore Science and Technology Days, Antwerpen, Belgien. 2022

Posterpräsentation

Prates da Costa, E., Göbel, U., Hofmann, A., Smarsly B. M., Effects of Hydrothermal Treatment on Mesopore Structure and Connectivity in Doped Ceria Zirconia Mixed Oxides, Deutsche Zeolith Tagung, Wien, Österreich. 2023

Inhaltsverzeichnis

1 Einleitung

Cerdioxid-basierte (CeO_2) Mischoxide finden breite Anwendung in einer Vielzahl an chemischen Prozessen, wie der Wasser-Gas-Shift Reaktion, der Rückgewinnung von Chlor aus Chlorwasserstoff (Deacon Prozess) und der thermochemischen Wasserspaltung. Allen gemein ist die Verwendung von porösem CeO_2 als Sauerstoffspeicher in einem heterogenen, katalytischen Prozess.

Das bis heute größte Anwendungsgebiet stellt jedoch die in den 1970er-Jahren aufgekommene Abgasnachbehandlung mittels der Drei-Wege-Katalyse (engl. *three-way catalysis*, TWC) dar.[1,2] Diese beschäftigt sich mit der Vermeidung toxischer Emissionen, welche durch Schwankungen im Verbrennungsluftverhältnis entstehen. Hierbei werden poröse CeO_2-basierte Mischoxide als aktive Sauerstoffspeicher-komponenten und Trägermaterialien für die katalytisch aktiven Edelmetalle (z.B. Pt, Pd, Rh) eingesetzt. Die drei namensgebenden Schadstoffe sind Kohlenstoffmonoxid (CO), Stickoxide (NO_x) und unverbrannte Kohlenwasserstoffe (engl. *hydro carbons*, HCs). Das Gefahrenpotential reicht dabei von akut toxischen Wirkungen, wie durch NO_x verursachten Atemwegserkrankungen, zu erheblichen Einflüssen auf die Umwelt durch beispielsweise die als „Radikalsenken“ und somit als Beschleuniger des Klimawandels wirkenden HCs. In Gegenwart von Wasserdampf sind sie zudem an der photochemisch katalysierten, bodennahen Bildung von Ozon („Sommersmog“) beteiligt, welches ebenfalls Atemwegsbeschwerden verursacht.

Angesichts dieser Problematiken wurden 1970 die ersten einheitlichen Grenzwerte für CO- und HC-Emissionen von Personenkraftwagen (PKW) in der Europäischen Gemeinschaft (EG) festgelegt.[3] Im Laufe der folgenden Jahrzehnte wurden die Richtlinien um weitere Schadstoffe (NO_x und Rußpartikel) ergänzt, auf andere Fahrzeugklassen ausgeweitet sowie stetig herabgesetzt. Die historische Entwicklung der Grenzwerte ist in Tabelle 1 dargestellt. Mit der sogenannten EURO-7-Norm, welche voraussichtlich im Jahr 2025 in Kraft treten soll, wurde im Jahr 2022 von der EU-Kommission ein Vorschlag zur Verschärfung der Abgasgrenzwerte vorgelegt, dem jedoch vom Europäischen Parlament und vom Europäischen Rat noch zugestimmt werden muss.

Tabelle 1. Schadstoffemmissiongrenzwerte für PKW in der Europäischen Union.[4]

	Schadstoff g km^{-1}	Euro 1	Euro 2	Euro 3	Euro 4	Euro 5	Euro 6
Einführung		1992	1996	2000	2005	2009	2014
Benzin	CO	2,72	2,2	2,3	1	1	1
	HC+NO_x	0,97	0,5	–	–	–	–
	THC	–	–	0,2	0,1	0,1	0,1
	NO_x	–	–	0,15	0,08	0,06	0,06
	Partikelmasse	–	–	–	–	0,0045	0,0045
	Partikelanzahl	–	–	–	–	–	$6{,}0 \cdot 10^{11}$
	NMHC	–	–	–	–	0,068	0,068
Diesel	CO	2,72	1	0,64	0,5	0,5	0,5
	HC+NO_x	0,97	0,7	0,56	0,3	0,23	0,17
	NO_x	–	–	0,5	0,25	0,18	0,08
	Partikelmasse	0,14	0,08	0,05	0,025	0,0045	0,0045
	Partikelanzahl	–	–	–	–	$6{,}0 \cdot 10^{11}$	$6{,}0 \cdot 10^{11}$

Getrieben durch die stetigen Absenkungen der Emissionsgrenzwerte, sind die technologischen Anforderungen an moderne Drei-Wege-Katalysatoren gestiegen. Eine maßgebliche Eigenschaft ist dabei die Temperaturstabilität der eingesetzten Sauerstoffspeicherkomponente, welche hohen Betriebstemperaturen, mit Temperaturspitzen bis zu 1100 °C, und schnell wechselnd reduzierenden und oxidierenden Bedingungen ausgesetzt ist. Da reines, poröses CeO_2 jedoch keine ausreichend hohe Temperaturstabilität aufweist,[5] welche zur Erhaltung einer hohen Porosität und damit einhergehender hoher Reaktivität unabdingbar ist, wurde ein erhebliches Maß an Entwicklungsarbeit in die chemische Zusammensetzung und die Beschaffenheit der Morphologie aufgewendet.[2] Besondere Meilensteine in der Entwicklung waren dabei die Erhöhung der thermischen Stabilität durch die in den 1980er Jahren aufkommende Verwendung von Mischoxiden mit Zirconiumdioxid (ZrO_2)[6] und später die Dotierung mit Metallen der Seltenen Erden wie beispielsweise Yttrium (Y) und Lanthan (La).

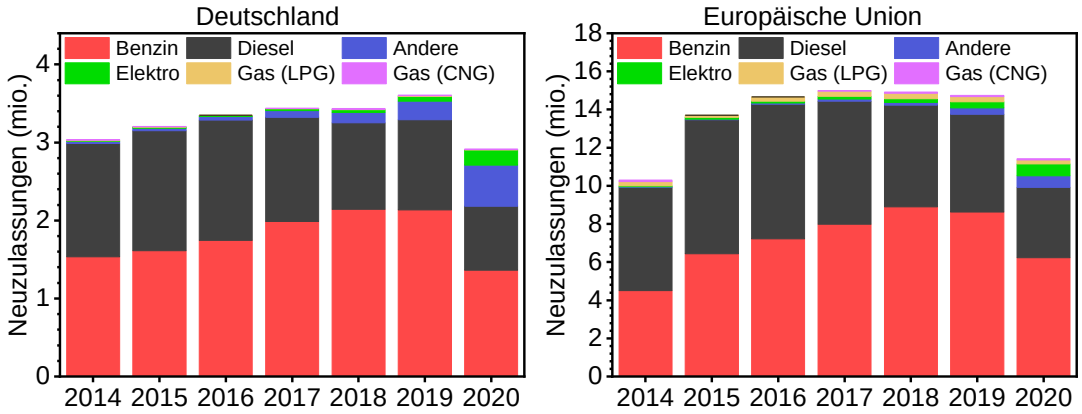

Abbildung 1. Neuzulassungen nach Antriebsart in Deutschland und in der EU.[7] (Der starke Rückgang an Neuzulassungen im Jahr 2020 ist bedingt durch die COVID-19-Pandemie.)

Wie am nach wie vor hohen Anteil an PKW mit Verbrennungsmotor an den Neuzulassungen in Deutschland und der EU erkennbar ist (Abbildung 1), wird die Entwicklung und Optimierung von Drei-Wege-Katalysatoren, trotz der voranschreitenden Elektrifizierung der Mobilität, auch im nächsten Jahrzehnt voraussichtlich einen wichtigen Beitrag zur Reduktion akut toxischer Emissionen leisten. Aber auch darüber hinaus ist die Weiterentwicklung von CeO_2-basierten Sauerstoffspeichermaterialien (engl. *oxygen storage materials*, OSMs) für weitere vielversprechende, zukünftige Anwendungen relevant, da diese ähnlichen Anforderungen, wie hoher Temperaturstabilität und hoher Zugänglichkeit des Porennetzwerkes, unterliegen. Ein Beispiel dafür ist die eingangs erwähnte thermochemische Wasserspaltung zur Herstellung von Wasserstoff mithilfe von Sonnenlicht, bei der die thermische Stabilität der Materialien direkt die Anzahl der möglichen Reaktorzyklen sowie deren Ausbeute beeinflusst.[8–11]

Da die Morphologie dieser Materialien maßgeblich durch die verwendete Syntheseroute bestimmt wird,[2] ist eine genaue Kenntnis der Beziehungen zwischen eingestellten Syntheseparametern und den daraus resultierenden Strukturen von großer Bedeutung, um hochleistungsfähige Katalysatormaterialien herzustellen. Aufgrund häufig ähnlicher Anforderungen an Temperaturstabilität und Porosität der Katalysatormaterialien in unterschiedlichen Anwendungsgebieten, ist ebendieser anwendungsübergreifende Aspekt das Kernthema dieser Arbeit, welcher am Beispiel der Synthese und Charakterisierung dotierter Cer-Zirconium Mischoxide (CZOs) für die TWC untersucht wurde. Besonderes Augenmerk wurde derweil auf die Konnektivität

der Poren gelegt, welche ein wichtiges Kriterium bei der Anwendung in der heterogenen Katalyse ist, da sie die Zugänglichkeit der katalytisch wirksamen Oberfläche beeinflusst. Der Begriff Konnektivität umfasst dabei sowohl die Anzahl verbundener Poren als auch die Durchmesser der verknüpfenden Porenhälse. Hierarchische Porennetzwerke haben sich hierbei als besonders geeignet für heterogene Katalyse erwiesen, da solche Strukturen auf die unterschiedlichen Transportprozesse im Inneren der Katalysatormaterialien optimiert sind. In der Literatur zur Synthese von CZOs werden hauptsächlich das mithilfe von Physisorptionsmessungen bestimmte Porenvolumen und die spezifische Oberfläche (BET-Oberfläche) als Parameter zur Beschreibung des Porenraumes angegeben. Diese erlauben jedoch nicht Aussagen über die Konnektivität der Poren zu treffen. Auch lässt sich durch diese Parameter allein die Ursache unterschiedlicher thermischer Stabilität nicht hinreichend erklären. Dafür ist eine tiefergehende Analyse notwendig, die es ermöglicht die Auswirkung spezifischer Syntheseparameter auf die Struktur des Porenraumes sowie die durch hohe Temperaturen verursachten Änderungen sichtbar und schlussendlich kontrollierbar zu machen.

Die Kernziele dieser Arbeit umfassen die Weiterentwicklung physisorptionsbasierter Charakterisierungsmethoden zur Strukturaufklärung ungeordneter Mesoporen-netzwerke und die Aufklärung von Zusammenhängen zwischen zugrundeliegenden Syntheseparametern und -schritten. Strukturelle Änderungen sollen dabei auf die während der Synthese stattfindenden chemischen Prozesse zurückgeführt werden. Dies soll anhand von eigens hergestellten, dotierten CZOs untersucht werden. Die besondere Herausforderung liegt darin, dass es sich dabei um ungeordnet mesoporöse Materialien mit einer komplexen, aber in der Industrie etablierten, Zusammensetzung handelt. Die gewonnenen Erkenntnisse sollen zu einem besseren Verständnis der für die Anwendung wichtigen strukturellen Eigenschaften beitragen und aufklären, wie diese entstehen, um so künftig gezielt Porenstrukturen mit hoher thermischer Stabilität und gut zugänglichen Poren herstellen zu können.

2 Stand der Wissenschaft und Technik

In den folgenden Kapiteln wird der wissenschaftliche Stand zur Synthese von CZOs sowie der eingesetzten Charakterisierungsmethoden beleuchtet, welche die Grundlage, der im Rahmen dieser Promotion entstandenen Veröffentlichungen, darstellen.

2.1 Die Chemie der Drei-Wege-Katalyse

2.1.1 Wirkungsprinzip und Aufbau eines Drei-Wege-Katalysators

Die Aufgabe eines Drei-Wege-Katalysators besteht darin die Emission der drei namensgebenden Schadstoffe CO, NO_x sowie HCs zu minimieren. Diese entstehen bei der Verbrennung des Kraftstoffes im Motor, wobei die Konzentration der einzelnen Komponenten von der verfügbaren Menge an Sauerstoff zum Verbrennungszeitpunkt abhängig ist. Das Verhältnis von Kraftstoffmenge zu Sauerstoffmenge wird mit dem λ-Wert (auch Luftzahl) beschrieben, welcher die tatsächlich vorhandene Sauerstoffmenge ins Verhältnis zur für die vollständige Verbrennung benötigten Sauerstoffmenge setzt (Gleichung (1)).

$$\lambda = \frac{n_{\text{verfügbar}}(O_2)}{n_{\text{benötigt}}(O_2)} \tag{1}$$

Für λ>1, liegt demnach ein Überschuss an Sauerstoff vor, was zwar einerseits die Oxidation von CO und HCs begünstigt, jedoch andererseits den Ausstoß von NO_x erhöht. Diese entstehen hauptsächlich aufgrund der hohen Temperaturen im Motorinneren aus dem Stickstoff, welcher mit der für die Verbrennung angesaugten Luft eingebracht wird.[12] Im Falle von λ<1, liegt ein Überschuss an Kraftstoff vor, was einen erhöhten Ausstoß an CO und HCs zur Folge hat, da der Sauerstoff nicht für die vollständige Oxidation ausreicht. Zur Minimierung von Schadstoffemissionen ist es also notwendig stets einen λ-Wert von λ≈1 beizubehalten. Unter Betriebsbedingungen wird dies mithilfe von zwei unterschiedlichen Strategien erreicht.[6] Einerseits findet eine Überwachung der Abgaszusammensetzung mittels λ-Sonden statt. Über eine Regelelektronik wird basierend darauf permanent die Zufuhr von Kraftstoff und Luft angepasst. Andererseits findet eine chemische Nachbehandlung des Abgases über dem Katalysator statt. Dieser besteht aus zwei wichtigen Komponenten: einem aktiven Edelmetall (z.B. Pt, Pd und/oder Rh) und einer CeO_2-basierten Sauerstoffspeicher-

komponente, welche sowohl kurzzeitige Schwankungen im λ-Wert ausgleicht als auch neben Aluminiumoxid (Al_2O_3) als Trägermaterial für das Edelmetall dient. Abbildung 2 zeigt die dabei katalysierten Reaktionen und deren λ-Wert abhängigen Umsatz sowie den optimalen Regelbereich. Die besondere Herausforderung besteht dabei darin, simultan die Oxidation von CO und HCs sowie die Reduktion von NO_x zu gewährleisten.

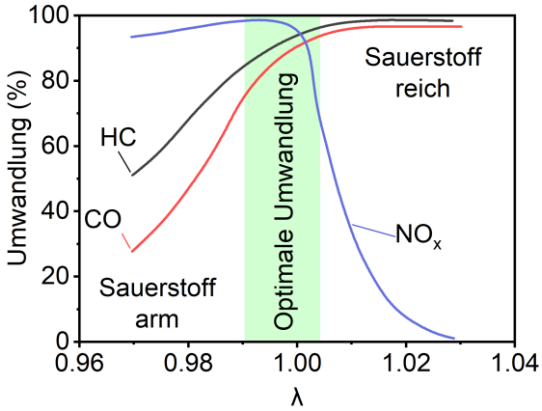

$$2NO + 2CO \rightarrow N_2 + 2CO_2$$

$$2CO + O_2 \rightarrow 2CO_2$$

$$2C_nH_{2m} + (2n + m)O_2 \rightarrow (2n)CO_2 + (2m)H_2O$$

Abbildung 2. λ-Wert abhängiger Umsatz[13] und Reaktionsgleichungen[12] der Drei-Wege-Katalyse.

Der allgemeine Aufbau eines TWC ist in Abbildung 3 gezeigt. Das mit dem Edelmetall beladene poröse Sauerstoffspeichermaterial Al_2O_3 wird als sogenannter „Wash-Coat" auf einen Keramikträger aufgebracht. Dieser Träger besteht in der Regel aus Cordierit und weist eine wabenförmige Struktur aus parallelen Kanälen auf, durch welche der Abgasstrom geleitet wird.[13] Der Keramikträger wird in ein Stahlgehäuse eingebettet, welches schlussendlich im Fahrzeug verbaut wird.

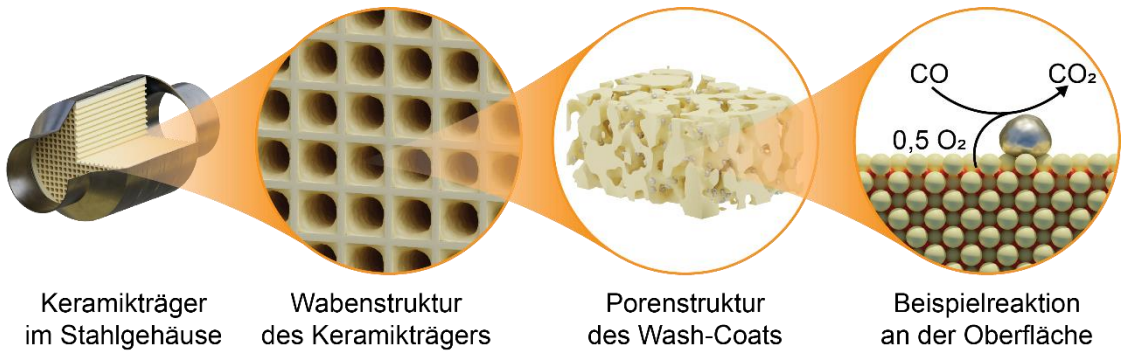

Abbildung 3. Schematischer Aufbau eines Drei-Wege-Katalysators.

Zwar liegen die Betriebstemperaturen eines Ottomotors mit 200–600 °C bei vergleichsweise niedrigen Temperaturen, doch aufgrund der baulichen Nähe zum Motor kann es zu kurzzeitigen Temperaturspitzen von bis zu 1100 °C kommen.[14] Daher ist eine hohe thermische Stabilität der OSMs notwendig, um eine lange Lebensdauer der Katalysatoren zu ermöglichen. Aus Kostengründen wird zudem zunehmend mit möglichst geringen Edelmetallbeladungen gearbeitet. Insbesondere das Einschließen von Edelmetall durch das Kollabieren von Poren stellt demnach eine der Hauptursachen für die Aktivitätsabnahme über die Gesamtbetriebsdauer eines Katalysators dar.

2.1.2 Sauerstoffspeicherkapazität

Die katalytische Aktivität von CeO_2 in der TWC, wie auch in anderen Anwendungsgebieten, beruht auf dessen Fähigkeit, abhängig vom umgebenden Sauerstoffpartialdruck, reversibel Sauerstoff aus dem Kristallgitter abzugeben. Die Sauerstoffspeicherkapazität (engl. *oxygen storage capacity*, OSC) bezeichnet dabei die Menge an Sauerstoff, die abgegeben werden kann. Wie in Gleichung (2) gezeigt ist, kann durch die Reduktion von zwei Ce^{4+}-Ionen zu zwei Ce^{3+}-Ionen ein Sauerstoffatom aus dem Kristallgitter abgegeben werden.[15] Die Zusammensetzung des Oxids reicht demnach von der vollständig oxidierten Form CeO_2 hin zur vollständig reduzierten Form Ce_2O_3.

$$2\mathrm{CeO_2} \leftrightharpoons \mathrm{Ce_2O_3} + 0{,}5\mathrm{O_2} \tag{2}$$

Abhängig vom Reduktionsgrad des Oxids, welcher häufig über das Sauerstoffdefizit δ angegeben wird, bilden sich auch defektreiche nicht-stöchiometrische Oxide ($CeO_{2-\delta}$), die ein komplexes Phasendiagramm zur Folge haben.[16] Dieser Sachverhalt wird häufig durch die in Gleichung (3) wiedergegebene Kröger-Vink-Schreibweise der Sauerstoff-fehlstellenbildung beschrieben.[15,17] Infolge der Abgabe eines Sauerstoffatoms kommt es zur Bildung einer neutralen Sauerstoffvakanz $V_O^{\bullet\bullet}$ in Oberflächennähe.

$$2\mathrm{Ce}_{Ce} + \mathrm{O_O} \leftrightharpoons 2\mathrm{Ce}'_{\mathrm{Ce}} + \mathrm{V}_{\mathrm{O}}^{\bullet\bullet} + 0{,}5\mathrm{O_2} \tag{3}$$

Aufgrund der Leitfähigkeit für Sauerstoff-Ionen kann diese anschließend durch Sauerstoff-Ionen aus der Bulkphase gefüllt werden und somit letztlich in die Bulkphase migrieren, wodurch der Sauerstoffspeicher sukzessive geleert oder gefüllt werden

kann. Welche OSC unter realen Bedingungen tatsächlich vorliegt, ist jedoch abhängig von vielen unterschiedlichen Faktoren, wie beispielsweise der Temperatur, der Zusammensetzung, der Mobilität[18] der Sauerstoff-Ionen im Kristallgitter, der Konzentration[19] an Sauerstofffehlstellen sowie der Nano- und Mesostruktur der Materialien[17,20,21].

Bei der quantitativen Charakterisierung der OSC wird zwischen der gesamt OSC (engl. *complete oxygen storage capacity*, cOSC) und der dynamischen OSC (engl. *dynamic oxygen storage capacity*, dOSC) unterschieden. Letztere zeichnet sich insbesondere dadurch aus, dass bei der Messung Anwendungsbedingungen (z.B. im schnellen Wechsel reduktive und oxidative Bedingungen) simuliert werden. Die gemessene dOSC spiegelt daher eine temperaturabhängige Teilentleerung des Sauerstoffspeichers wider, die üblich als relevanter als die cOSC erachtet wird.

Zur Bestimmung der OSC haben sich maßgeblich zwei Methoden etabliert: die Temperaturprogrammierte Reduktion[22] (TPR) und Puls-Injektions-Methoden[23–25]. Bei der TPR wird die Aufnahme von Wasserstoff (H_2-TPR) oder Kohlenstoffmonoxid (CO-TPR) in Abhängigkeit eines Temperaturprogramms mithilfe eines Wärmeleitfähigkeitsdetektors gemessen. Aus der aufgenommenen Gesamtmenge lässt sich direkt die cOSC als Integral der Messkurve bestimmen. Darüber hinaus beinhaltet die Form der TPR-Kurve Informationen über die temperaturabhängige Reduzierbarkeit des Materials. Bei CeO_2 werden dabei meist zwei charakteristische Signale beobachtet, die der Reduktion der Oberfläche (engl. *low-temperature* – LT, ca. 400–500 °C) und der Reduktion der *bulk*-Phase (engl. *high-temperature* – HT, ca. 700 °C) zugeordnet werden.[26,27] Für die Bestimmung der cOSC ist dieses einfache Experiment zwar gut geeignet, jedoch kann damit, aufgrund des Ausbleibens einer Gleichgewichtseinstellung, einerseits nicht die cOSC bei einer festen Temperatur, wie sie beispielsweise durch einen Prozess vorgegeben sein könnte oder die dOSC bei dynamisch wechselnden Zusammensetzungen der Gasatmosphäre bestimmt werden. Dies ist jedoch mit sogenannten Puls-Injektions-Methoden möglich, bei denen kurze Pulse eines Messgases (z.B. H_2, CO, oder O_2) auf die Probe gegeben werden, um so bei konstanter Temperatur die cOSC oder dOSC zu bestimmen. Für die dOSC wird dabei abwechselnd mit H_2 (oder CO) und O_2 gepulst.

2.1.3 Die Rolle der Dotierungselemente in OSMs

Da reines CeO_2 eine niedrige thermische Stabilität aufweist, bestehen moderne OSMs für die Anwendung in der TWC heutzutage aus komplexen Mischungen verschiedener Metalloxide. Häufig beinhalten diese Mischoxide neben dem für die Sauerstoffspeicherfähigkeit benötigten CeO_2 die Oxide ZrO_2, Y_2O_3 und La_2O_3, deren spezifische Rollen im folgenden Abschnitt erläutert werden.

Der größte Fortschritt in der Entwicklung von OSC-Materialien für die TWC wurde durch die Bildung fester Lösungen des CeO_2 mit ZrO_2 erzielt. So konnte eine maßgebliche Erhöhung der thermischen Stabilität, aber auch der OSC, insbesondere durch die erhöhte Reduzierbarkeit des *bulk*-Materials, festgestellt werden, wie mittels TPR-Analyse gezeigt werden konnte.[28–30] Da sich die Oxidationsstufe der Zr^{4+}-Ionen im Verlauf der Katalysereaktionen nicht ändert, beruht die beobachtete Erhöhung der OSC ausschließlich auf in Bezug auf die Katalysereaktion passiven Effekten, welche häufig dem im Vergleich zu Ce^{4+}-Ionen (0,97 Å) kleineren Ionenradius der Zr^{4+}-Ionen (0,84 Å) zugeschrieben werden.[6,15,31,32] Die unterschiedlichen Ionenradien haben gravierende Auswirkungen auf die Kristallstruktur und sind Ursache für das komplexe Phasendiagramm[33] des binären Mischoxides. Bei Erhöhung des ZrO_2-Anteils auf bis zu 50 mol% führt dies zu einer sukzessiven Abnahme des Volumens der Einheitszelle sowie einer Verzerrung des Sauerstoff-Gitters ausgehend von der kubischen Fluorit-Struktur. Dies hat eine Erhöhung der Mobilität der Sauerstoff-Ionen zur Folge und begünstigt die Bildung von Sauerstofffehlstellen.[15,34] Darüber hinaus wurde bei reinem CeO_2 eine durch den größeren Ionenradius der Ce^{3+}-Ionen verursachte Zunahme des Volumens der Einheitszelle bei Reduktion beobachtet. Die deutlich kleineren Zr^{4+}-Ionen ermöglichen es dadurch verursachte Verspannungen zu mindern und so die thermische Stabilität des Materials zu erhöhen. Zwar gelang es durch die Verwendung des binären Mischoxides die thermische Stabilität der OSC-Materialien signifikant zu erhöhen, jedoch wurde beobachtet, dass bei langer Verwendungsdauer eine Segregation in eine Cer-reiche und eine Cer-arme Mischphase stattfindet, welche eine Abnahme der OSC und den Verlust von Porosität zur Folge hat. Die Neigung zur Segregation hängt dabei unter anderem stark von der synthesebedingten Homogenität des Mischoxides ab.[5]

Weitere Erhöhungen der thermischen Stabilität und OSC sowie eine Unterbindung der Entmischung der festen Lösung konnten durch die zusätzliche Dotierung mit trivalenten Dotierungselementen wie beispielsweise Y^{3+} und La^{3+} erreicht werden.[32,35–37] Der größte Unterschied liegt jedoch in der Oxidationsstufe der Dotierungselemente, aufgrund derer intrinsische Sauerstofffehlstellen im Kristallgitter erzeugt werden. Da sich die Oxidationsstufen des Y^{3+} und des La^{3+} nicht ändern, wirken auch diese sich hauptsächlich durch die erhöhte Mobilität der Sauerstoff-Ionen im Kristallgitter positiv auf die OSC aus.

2.2 Synthesemethoden für mesoporöse CeO_2-basierte Mischoxide

Neben der Zusammensetzung des Mischoxids stellt die zugrundeliegende Synthese eine wichtige Stellschraube zur Verbesserung der physiko-chemischen Eigenschaften dar.[2] Aufgrund des direkten Einflusses auf die Textur der Mischoxide wird die thermische Stabilität und katalytische Aktivität unmittelbar durch die ausgewählte Route, die verwendeten Präkursoren und die eingestellten Parameter, wie beispielsweise pH und Temperatur, kontrolliert. Um den steigenden Anforderungen an OSMs gerecht zu werden, wurden in den letzten Jahrzehnten zahlreiche Routen zur Synthese nanoporöser CeO_2-basierter Mischoxide entwickelt, die zu einer allgemeinen Optimierung der Eigenschaften sowie zu einem besseren Verständnis darüber, wie diese durch gezielte Manipulation der Parameter erreicht werden können, beigetragen haben. Für eine industrielle Anwendbarkeit ist es zudem relevant, dass die gewählte Synthese im großen Maßstab kostengünstig durchgeführt werden kann. Zu den verbreitetsten Methoden im Bereich der CZOs zählen deshalb die Co-Fällung und die Solvo-/Hydrothermalsynthese.[2,5]

2.2.1 Co-Fällung

Die Co-Fällung stellt die simpelste nasschemische Methode zur Herstellung von Mischoxiden dar. Bei ihr werden die Edukte – zumeist Nitrate oder Halogenide der gewünschten Metalle – gelöst, homogenisiert und durch Zugabe einer Base, wie Natronlauge oder wässriger Ammoniaklösung, als Hydroxide gefällt und durch anschließende Kalzinierung in das Oxid umgewandelt. Die Kontrolle über die Textur des Mischoxides geschieht hierbei über die für die Fällung gewählte Base, die Reaktionstemperatur, die Rührgeschwindigkeit, den pH-Wert der Lösung sowie die Ausgangskonzentration der Edukte. Diese Parameter beeinflussen in erster Linie die Prozesse der Nukleation und des Partikelwachstums durch Ostwald-Reifung oder Agglomeration und steuern so die Größe und Morphologie der gebildeten Partikel. Grundvoraussetzung für die Co-Fällung ist jedoch ein ähnliches Löslichkeitsverhalten der einzelnen Präkursoren, um eine hohe Homogenität der zu bildenden festen Lösung und so eine hohe Stabilität gegen eine Phasensegregation zu gewährleisten.[5] Auch die Wahl des eingesetzten Cer-Präkursoren (z.B. $Ce(NO_3)_3 \bullet 6H_2O$ *vs.* $(NH_4)_2[Ce(NO_3)_6]$) hat einen großen Einfluss auf die Homogenität und somit Phasenstabilität des gebildeten

Mischoxides.[38] Die thermische Stabilität und katalytische Aktivität der Materialien wurde in der Literatur weitgehend anhand der Zusammensetzung, spezifischer Oberflächen und OSCs diskutiert.[20,39,40] Eine nähere Charakterisierung des Porenraumes und des Einflusses der Syntheseparameter auf diesen bleibt jedoch zumeist aus.

2.2.2 Solvo-/Hydrothermalsynthese

Eine Alternative zur Co-Fällung stellt die Solvo- oder Hydrothermalsynthese dar, bei der die gelösten Präkursoren in einem Autoklav bei Temperaturen oberhalb der Standardsiedetemperatur des Lösungsmittels unter hohem Druck behandelt werden und die Mischoxide direkt aus der Lösung kristallisieren.[41] Der allgemeine Begriff Solvothermalsynthese deutet bereits an, dass solche Reaktionen in einer Vielzahl an Lösungsmitteln durchgeführt werden können. Findet die Reaktion in wässriger Lösung statt, wird von Hydrothermalsynthese gesprochen.

In einer Studie der Synthesebedingungen konnten Hirano *et al.* mithilfe systematischer Variation der Temperatur, Konzentration und Zusammensetzung die Einflüsse auf die thermische Stabilität und kristallinen Phasen der gebildeten CZOs erörtern.[42] Die aus saurer, wässriger Lösung synthetisierten Nanopartikel waren auch nach Kalzinierung bei 1000 °C phasenrein und wiesen eine hohe spezifische Oberfläche auf. Die Autoren führen dies auf die sehr ähnliche Hydrolysegeschwindigkeit der eingesetzten Präkursoren – $(NH_4)_2[Ce(NO_3)_6]$ und $ZrOCl_2 \bullet 8H_2O$ – zurück. Durch kontrollierte Agglomeration der gebildeten Primärpartikel konnten Ohtake *et al.* in einem hydrothermalen Prozess mesoporöses CeO_2 mit hoher spezifischer Oberfläche und thermischer Stabilität herstellen.[43] Das hergestellte Material wies bei Kalzinierung bei hohen Temperaturen nur ein geringes Kristallitwachstum auf, was die Autoren auf eine Inhibierung von Sinterprozessen durch die hohe Mesoporosität und die Verknüpfung der Primärpartikel über kleine Kontaktflächen zurückführen. Dieser Ansatz wurde von Özkan *et al.* aufgegriffen und eine ausführliche Studie des Mesoporenraumes der frisch hergestellten sowie thermisch gealterten Pulver durchgeführt.[44] Mittels detaillierter Physisorptionsanalyse und Elektronentomographie konnte die dreidimensionale Anordnung der Primärpartikel als Ursache für die thermische Stabilität der Mesoporen

nachgewiesen werden. Darüber hinaus wurde eine zusätzliche Inhibierung der Sinterprozesse durch an die Oberfläche gebundene Nitratgruppen nachgewiesen.

2.2.3 Nachträgliche Modifikation des Mesoporenraumes

Neben der initialen Synthese des Mischoxides mittels Co-Fällung oder Hydrothermalsynthese kann auch eine zusätzliche hydrothermale Nachbehandlung der Niederschläge zu einer weiteren Stabilisierung und Erhöhung der OSC beitragen. Der Einfluss einer solchen Nachbehandlung in basischer, wässriger Lösung wurde von Chuah *et al.* an über eine Fällung hergestelltem, mesoporösem ZrO_2 untersucht.[45] Die nachbehandelten Pulver wiesen dabei größere Mesoporen, eine höhere Porosität sowie eine höhere thermische Stabilität auf als die nicht nachbehandelten Referenzproben. Die Autoren vermuten eine Verstärkung des Mesoporenskeletts durch Ostwald-Reifung und Auflösung und Wiederausfällung der gefällten Hydroxide als Ursache für die erhöhte thermische Stabilität. Di Monte *et al.* konnten mit einer vergleichbaren Nachbehandlung von binären CZOs unterschiedlicher Zusammensetzungen denselben Effekt nachweisen und zeigen, dass dieser unabhängig von der Zusammensetzung des Mischoxides ist.[46] Raju *et al.* konnten weiterhin an binären CZOs zeigen, dass eine längere Nachbehandlungsdauer die spezifische Oberfläche erhöht.[47] In einer Analyse mittels TPR konnten sie zudem eine Erhöhung der Reduzierbarkeit der Materialien durch die Nachbehandlung aufzeigen.

2.2.4 Mesostrukturierung

Die in den Abschnitten 2.2.1 und 2.2.2 beschriebenen Methoden resultieren in Materialien mit ungeordneter Mesoporenstruktur. Auch wenn die industrielle Relevanz von strukturierten OSMs aufgrund der aufwändigen Herstellung derzeit nicht groß ist, soll an dieser Stelle dennoch kurz auf diese eingegangen werden, da sie als Modellmaterialien wertvolle Einblicke in die Materialeigenschaften bieten können. Der Vorteil daran ist, dass die Materialien eine definierte Porenform und -größe sowie Porosität erhalten, die sich leicht charakterisieren lassen.

Grundsätzlich wird zwischen zwei unterschiedlichen Templatierungsverfahren unterschieden: Hardtemplating und Softtemplating. Beim Hardtemplating werden beispielsweise Silicamaterialien, oder monodisperse, kugelförmige Polymethyl-

methacrylat(PMMA)-Partikel als strukturgebende Template verwendet,[48,49] welche anschließend herausgelöst oder herausgebrannt werden. Beim Softtemplating werden hingegen vornehmlich organische Polymere eingesetzt, die unter den für die Synthese gewählten Bedingungen Mizellen ausbilden und so die Struktur des resultierenden Oxides vorgeben. Cop *et al.*, zum Beispiel, haben anhand von mit einem Diblockcopolymer strukturiertem CeO_2 den Einfluss von Dotierungselementen auf die katalytische Aktivität und Stabilität in der HCl Oxidations-Reaktion untersucht.[50] Die hoch definierte Struktur der hergestellten Pulver ermöglichte eine detaillierte Beurteilung der Stabilität der Materialien unter den harschen Reaktionsbedingungen.

2.3 Charakterisierung ungeordneter mesoporöser Materialien

Während die Charakterisierung von Materialien mit geordneter Mesoporenstruktur mittels Physisorptionsanalyse etabliert ist und durch bildgebende Methoden (z.B. Raster-Elektronenmikroskopie) gestützt werden kann, stellen Materialien mit ungeordneter Mesoporenstruktur hierbei eine besondere Herausforderung dar. Die nicht-einheitliche Form der Mesoporen sowie deren Lage und Verknüpfung zu einem Porennetzwerk lässt sich durch einfache bildgebende Methoden kaum erfassen und die Interpretation von Physisorptionsmessungen, insbesondere im Hinblick auf die Konnektivität der Mesoporen, ist bisher wenig erforscht. In Katalyseanwendungen sind Materialen mit ungeordneter Mesoporenstruktur jedoch weit verbreitet. Die Ursache hierfür ist, dass für die Synthese geordneter Materialien aufwändige Templatierungs-verfahren notwendig sind. Aus wirtschaftlicher Sicht ist die Verwendung simpler und leicht skalierbarer Syntheserouten jedoch attraktiver. Wie im vorherigen Abschnitt beschrieben, resultieren diese jedoch meist in wenig strukturierten, bis völlig ungeordneten Mesoporennetzwerken. Obwohl eine 3D-Analyse des Porenraumes mittels Elektronentomographie (Abschnitt 2.3.2) alle benötigten Informationen über das Porennetzwerk liefern kann und darüber hinaus eine detaillierte Analyse der festen Phase ermöglicht, eignet sich diese Methode aufgrund des hohen Zeit- und Kostenaufwandes nicht für eine routinemäßige Analyse im industriellen Umfeld. Diese Tatsache und der große Einfluss der zugrundeliegenden Synthesemethode auf die Porosität der Materialien zeigen auf, dass geeignete physisorptionsbasierte Mess- und Auswertungsmethoden dringend benötigt werden, die es erlauben feine Änderungen

in der Konnektivität des Porenraumes detektierbar, auf die Synthesebedingungen rückführbar und schlussendlich erklärbar zu machen. Diese Methoden werden im nachfolgenden Abschnitt, zusammen mit den etablierten Methoden, erläutert.

2.3.1 Physisorptionsanalyse

Die Physisorptionsanalyse stellt eine bewährte und weit verbreitete Methode zur Charakterisierung mesoporöser Materialien dar. Sie ermöglicht die Bestimmung zahlreicher Deskriptoren des Porenraumes, wie zum Beispiel spezifische Oberflächen, Porenvolumina sowie Porengrößen. Moderne Methoden, die auch einen Schwerpunkt dieser Arbeit darstellen, erlauben es darüber hinaus, weiterhin die Konnektivität des Porenraumes zu analysieren.

Physisorption basiert auf der Anreicherung (Adsorption) eines Analysegases (Adsorptiv) auf der Oberfläche eines Feststoffes (Adsorbens) aufgrund schwacher physikalischer Wechselwirkungen, wie beispielsweise Van-der-Waals-Wechselwirkungen und unterscheidet sich somit von der Chemisorption, welche auf der Ausbildung kovalenter Bindungen basiert (z.B. CO auf Pt zur Bestimmung der Platindispersion auf einem Trägermaterial). Im Verlauf einer Messung wird bei konstanter Temperatur, meist am Siedepunkt des Adsorptivs, das adsorbierte Volumen des Adsorptivs in Abhängigkeit des Relativdrucks über dem Adsorbens aufgezeichnet, wobei die Form der resultierenden Isotherme maßgeblich durch die Struktur des Porenraumes und die Stärke der Wechselwirkungen vorgegeben ist.

Eine erste Klassifizierung der häufig anzutreffenden Isothermentypen wurde 1985 im technischen IUPAC Bericht zur Physisorptionsanalyse getroffen, welcher im Jahre 2015 aktualisiert wurde.[51] Die aktualisierte Klassifizierung ist in Abbildung 4 gezeigt und erlaubt bereits erste Aussagen über die Beschaffenheit des Porenraumes eines Materials zu treffen. So deutet eine Isotherme vom Typ I auf ein mikroporöses Material (Porendurchmesser $d_{Pore} < 2$ nm) hin, wohingegen eine Isotherme des Typen IV bei mesoporösen Materialien ($2 \text{ nm} < d_{Pore} < 50$ nm) vorzufinden ist.

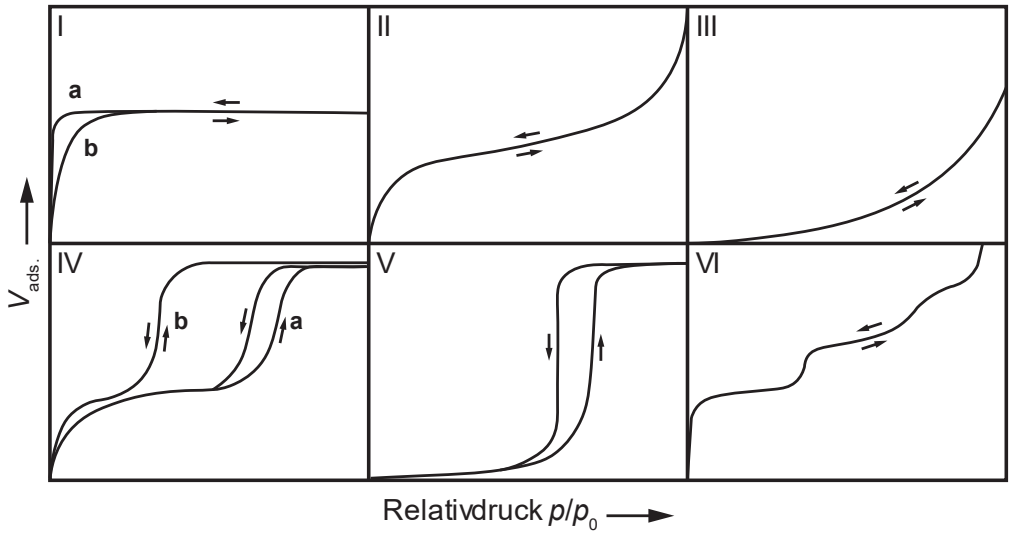

Abbildung 4. Klassifizierung häufig auftretender Isothermen. Adaptiert nach dem aktualisierten IUPAC Bericht.[51]

Um aus gemessenen Isothermen quantitative Informationen über die Struktur des Porenraumes zu erhalten, sind geeignete Modelle und Auswertungsmethoden erforderlich, die seit Beginn des 20. Jahrhunderts erdacht und stetig weiterentwickelt wurden. Die ersten Beschreibungen der Adsorption von Gasen auf Oberflächen gehen auf Irving Langmuir zurück, der erstmals die Adsorption einer Monolage nachweisen und so die spezifische Oberfläche von Festkörpern ermitteln konnte.[52,53] Die heutzutage gebräuchliche Methode zur Bestimmung spezifischer Oberflächen ist die sogenannte Brunauer-Emmett-Teller (BET) Methode.[54] Diese stellt eine Verallgemeinerung der Langmuir-Theorie dar und erweitert diese um eine Beschreibung der stattfindenden Multilagenadsorption. Beide Verfahren nutzen die durch spezielle linearisierte Auftragungen berechnete Stoffmenge adsorbierter Gasteilchen einer Monolage n_{mono} und den spezifischen Flächenbedarf σ eines einzelnen Gasteilchens zur Berechnung der spezifischen Oberfläche $A_{\text{spezifisch}}$ über den in Gleichung (4) gezeigten Zusammenhang zur Probenmasse m.

$$A_{spezifisch} = \frac{n_{mono} \cdot N_A \cdot \sigma}{m} \tag{4}$$

Seit dem IUPAC Bericht aus dem Jahre 2015 wird hierfür die Verwendung einatomiger Gase, wie Argon oder Krypton (bei sehr kleinen spezifischen Oberflächen), empfohlen, da diese im Gegensatz zum weit verbreiteten Stickstoff nicht über ein Quadrupolmoment verfügen. Dieses kann bei Stickstoff zu einer durch die

Oberflächenchemie, z.B. durch Hydroxy-Gruppen an der Oberfläche von Metalloxiden, hervorgerufene Vorzugsorientierung der Stickstoffmoleküle und so zu einer Fehlerbehaftung des bestimmten Wertes führen, da $\sigma(N_2)$ einen Mittelwert der zwei Extrempositionen darstellt.

Neben der spezifischen Oberfläche spielt auch die Porosität von Festkörpern eine große Rolle. Insbesondere das Porenvolumen und die Porendurchmesserverteilung (engl. *pore size distribution,* PSD) sind kritische Parameter für Katalyseanwendungen. Das weit verbreitete Standardverfahren zur Bestimmung von PSDs und Porenvolumina ist dabei die Barrett-Joyner-Halenda (BJH) Methode,[55] welcher die in Gleichung (5) (gültig für Desorption aus zylindrischen Poren) gezeigte modifizierte Kelvingleichung zugrunde liegt, die den Druck eines Gases über einer gekrümmten Oberfläche beschreibt. Sie setzt damit den Porenradius r_m mit dem Relativdruck p/p_0 über dem Adsorbens in Zusammenhang. Es gilt:

$$ln\left(\frac{p}{p_0}\right) = -\frac{2\gamma V_m}{RT(r_m - t_c)} \tag{5}$$

mit der Grenzflächenspannung γ, dem molaren Volumen V_m und der Dicke des adsorbierten Multilagenfilms t_c.

In Kombination mit dem in einem Desorptionsschritt desorbierten Volumen lässt sich so eine differentielle PSD sowie das kumulative Porenvolumen berechnen. Die Gültigkeit der Kelvingleichung ist jedoch für kleine Mesoporen (d_{Pore} < 20 nm) fragwürdig, insbesondere, da die für die Berechnung der Höhe (engl. *thickness*, t_c) des adsorbierten Filmes verwendeten „*thickness curves*“ die Krümmung und stärkeren Oberflächenkräfte nicht korrekt beschreiben.

Nicht-lokale Dichtefunktionaltheoriebasierte (NLDFT) Methoden können diese Limitierungen überwinden und ermöglichen somit eine korrekte Bestimmung der Porengrößen über einen großen Bereich. Sie beruhen auf einer Anpassung eines sogenannten Kernels – eine Sammlung theoretischer Isothermen für ein Paar aus Adsorptiv und Adsorbens bei einer festgelegten Temperatur und Porengeometrie – an eine gemessene Isotherme. Jede dieser theoretischen Isothermen $N(p/p_0, w)$ beschreibt die Ad- oder Desorption in einer Pore mit der Weite w. Über Gleichung (6)

lässt sich mit dem Kernel und der gemessenen Isotherme $N(p/p_0)$ die PSD als Verteilungsfunktion $f(w)$ bestimmen.

$$N\left(\frac{p}{p_0}\right) = \int_{w_{min}}^{w_{max}} N\left(\frac{p}{p_0}, w\right) f(w) dw \qquad (6)$$

Einige der in Abbildung 4 gezeigten Isothermen, wie zum Beispiel Isothermen des Typs IV, zeichnen sich insbesondere durch das Vorkommen einer ausgeprägten Hystereseschleife aus, welche durch die Form und Größe der Poren sowie Netzwerkeffekte beeinflusst wird. Nach der IUPAC Klassifikation wird zwischen sechs charakteristischen Typen unterschieden, welche in Abbildung 5 dargestellt sind. Grundsätzlich gilt hierbei, dass der Adsorptionsast Aufschluss über die Verteilung der Porengrößen und der Desorptionsast über die Porenöffnungen – also das Verbindungsfenster zu benachbarten Poren – gibt.

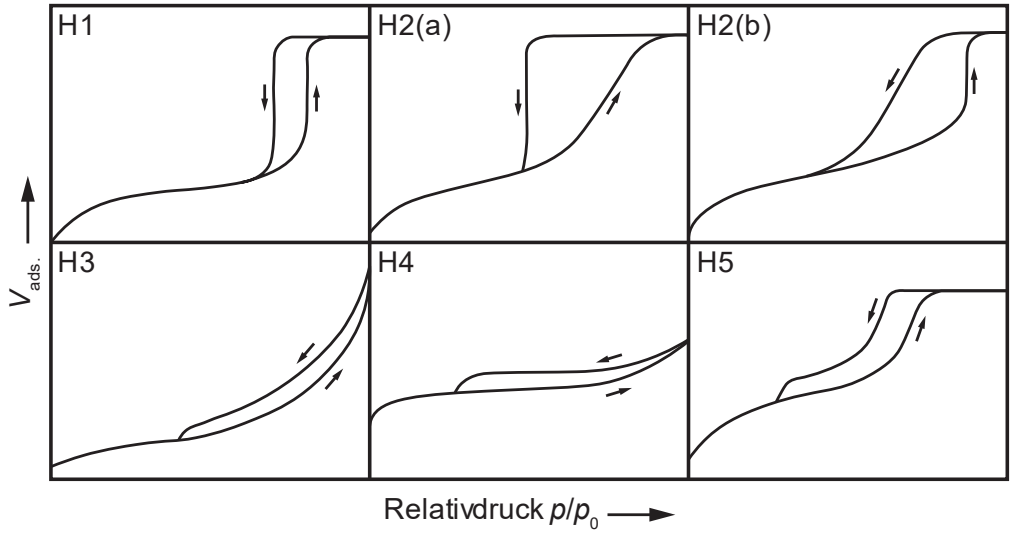

Abbildung 5. Klassifizierung häufig auftretender Hystereseschleifen. Adaptiert nach dem aktualisierten IUPAC Bericht.[51]

Materialien mit einer schmalen PSD und einheitlicher Porengeometrie, wie beispielsweise SBA-15, weisen ein Hystereseverhalten vom Typ H1 auf, welches sich durch sehr steile Sorptionsäste auszeichnet. Netzwerkeffekte spielen bei Materialien dieses Typs in der Regel keine Rolle, jedoch können auch Materialien mit ungeordneten Mesoporennetzwerken diese Gestalt annehmen, wenn die Größenverteilungen der Poren sowie der Porenöffnungen identisch sind. In ungeordneten Mesoporennetzwerken hingegen spielen Netzwerkeffekte meist eine große Rolle, welche zu Hystereseschleifen des Typs H2 führen. Unterschieden wird

zusätzlich zwischen den Subtypen H2(a) und H2(b), die sich in der Konnektivität zwischen Poren unterscheiden. Ersterer zeichnet sich durch einen moderat ansteigenden Adsorptionsast und einen sehr steilen Desorptionsast aus. Hervorgerufen wird diese Form durch eine breite PSD bei gleichzeitig sehr schmaler PSD der Porenöffnungen. Abhängig vom Größenunterschied zwischen Pore und Porenöffnung treten zwei unterschiedliche Desorptionsmechanismen auf: Pore-Blocking oder Kavitation.

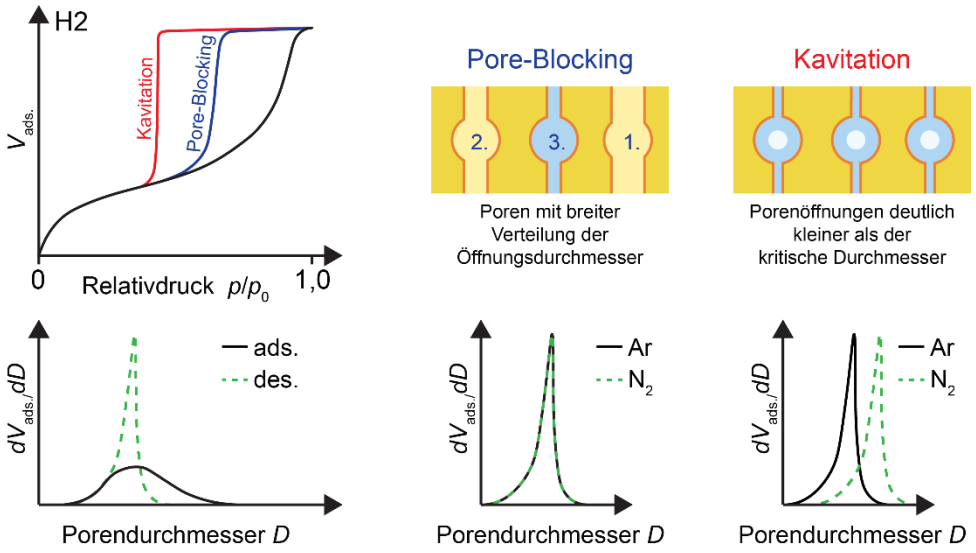

Abbildung 6. Schematische Darstellung des Einflusses von Pore-Blocking oder Kavitation auf den Desorptionsast und die desorptionsbasierte PSD.

Beim Pore-Blocking wird die Desorption aus großen Poren durch kleinere Poren, welche erst bei geringen Relativdrücken entleert werden, verzögert. Ist der Größenunterschied sehr groß, kann es während der Desorption zur Bildung einer Gasblase im Inneren der Pore kommen, weil das flüssige Adsorbat in den Poren instabil wird und eine sprungartige Entleerung dieser stattfindet (vgl. Abbildung 6).[56,57] Dieser Prozess wird Kavitation genannt. Der Subtyp H2(b) unterliegt ebenfalls dem Pore-Blocking und tritt dann auf, wenn die PSD der Porenöffnungen im Gegensatz zum Subtyp H2(a) breit ist. Dies äußert sich in einer moderaten Steigung des Desorptionsastes. Um zu untersuchen, ob eine Hinderung in der Entleerung der Poren durch Netzwerkeffekte vorliegt, können die adsorptions- und desorptionsbasierte PSD verglichen werden (Abbildung 6).[58] Sind die PSDs identisch, liegt keine Hinderung in der Desorption vor. Wird die Desorption hingegen durch kleine Porenöffnungen verzögert, so ist die PSD der Porenöffnungen gegenüber der PSD der Poren zu kleineren Durchmessern verschoben.

Um zwischen den Desorptionsmechanismen zu unterscheiden, die als Maß für die Zugänglichkeit von Poren dienen können, und somit die Konnektivität eines Porennetzwerkes zu analysieren, wurden unterschiedliche Verfahren entwickelt. Einerseits ist dies über einen Vergleich der PSDs der Porenöffnungen möglich, welche unter Verwendung unterschiedlicher Adsorptive, wie zum Beispiel Argon und Stickstoff, ermittelt wurden, wie zum Beispiel von Thommes *et. al* an mikro- und mesoporösen Silicamaterialien demonstriert wurde.[58] Da es sich bei Kavitation um einen thermodynamischen Effekt handelt, welcher vom Sättigungsdampfdruck des verwendeten Adsorptivs abhängig ist, führt dies im Vergleich der desorptions-basierten PSDs zu einer Verschiebung dieser zueinander (Abbildung 6). Pore-Blocking hingegen ist ein rein geometrischer Effekt, bei dem die desorptions-basierten PSDs identisch sind. Eine weitere Möglichkeit stellt das sogenannte (Desorptions-)Hysterese-Scanning dar, bei dem eine Reihe an zusätzlichen Desorptionskurven ausgehend von einem partiell gefüllten Porennetzwerk aufgezeichnet wird. Die typischerweise zu erwartenden Desorptionsisothermen für die Hysteresetypen H1 und H2 sind beispielhaft in Abbildung 7 illustriert.

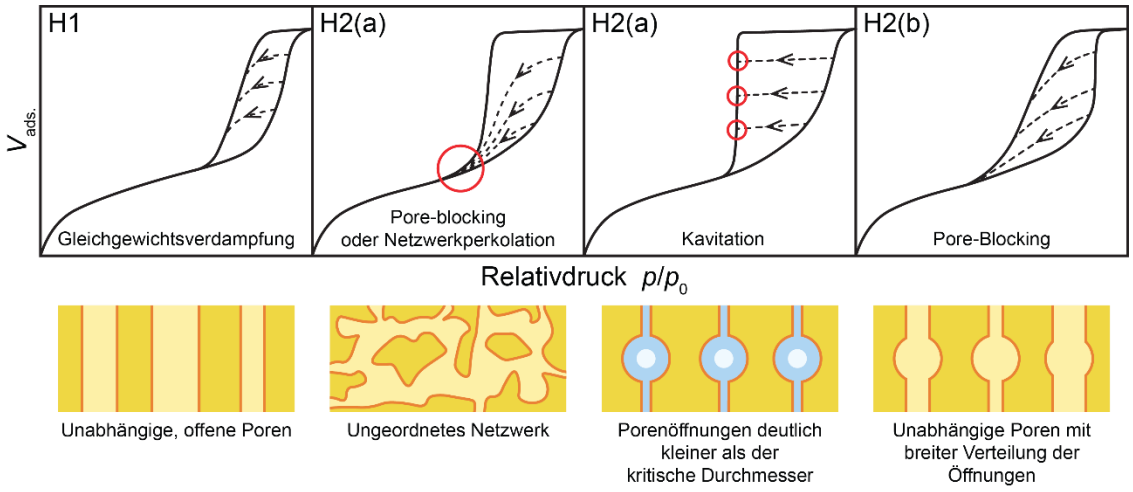

Abbildung 7. Schematische Darstellung der erwarteten Scanning-Desorptionsisothermen und zugehörige Desorptionsmechanismen. Adaptiert nach Kube *et. al*.[59]

Eine qualitative Analyse der Form der resultierenden Desorptionsisothermen gibt weiterhin Aufschluss über die Konnektivität von Poren im Material.[57,59–62] Im Fall von unabhängigen, offenen Poren oder beim Auftreten von Kavitation kreuzen die Desorptionsisothermen die Hystereseschleife parallel zum Plateau in der einhüllenden Desorptionsisotherme, bis sie auf diese treffen. Liegt Pore-Blocking oder Netzwerk-

perkolation vor, unterscheiden sich die Desorptionsisothermen stark von der Einhüllenden. Ihre Form hängt hierbei maßgeblich von der Konnektivität der Poren ab. In ungeordneten Netzwerken, beispielsweise, konvergieren die Desorptionsisothermen meist in dem Punkt, an dem auch die einhüllende wieder auf die Adsorptionsisotherme trifft. In solch komplexen Porennetzwerken besteht zudem die Möglichkeit, dass eine Kombination unterschiedlicher Netzwerkeffekte vorliegt, was eine Interpretation der Porenkonnektivität erheblich erschwert und sie zum Gegenstand aktueller Forschung macht. So konnten Kube *et al.* etwa synthesebedingte Inhomogenitäten in der räumlichen Verteilung von Porengrößen mithilfe von Physisorptionsanalyse in Kombination mit *in situ* SAXS an mesoporösen Silicamaterialien nachweisen und ihren Einfluss auf die Desorptionsisothermen erörtern.[59] Neben einer qualitativen Analyse der Netzwerkkonnektivität existieren auch Ansätze zur Quantifizierung, die, wie das von Cimino *et al.* beschriebene Verfahren, auf mittels Monte-Carlo-Simulation erstellten Perkolationsmodellen beruhen.[60] Diese erlauben unter gewissen Voraussetzungen die Ermittlung einer mittleren Koordinationszahl der Mesoporen.

2.3.2 Elektronentomographie

Die Elektronentomographie ist eine Methode, um die dreidimensionale Struktur unterschiedlichster Proben zu untersuchen. Sie findet breite Anwendung in Forschungsfragen der Biologie und Medizin sowie in der Materialforschung und ermöglicht es Zusammenhänge zwischen dreidimensionaler Struktur und Funktion zu erörtern, die über die Möglichkeiten einer zweidimensionalen Betrachtung mittels Raster- oder Transmissionselektronenmikroskopie (TEM) weit hinausgehen.[63,64] So lassen sich aus den gewonnenen Rekonstruktionen beispielsweise die Dimensionen von Poren und deren räumliche Anordnung zueinander sowie die Verknüpfung[44,65,66] untereinander ermitteln und deren Einflüsse auf Transportprozesse[65,67] in porösen Katalysatormaterialen erklären. Die Rekonstruktionen werden dabei aus einer Serie an zweidimensionalen TEM-Bildern – zweidimensionale Projektionen der dreidimensionalen Struktur – berechnet, welche aus unterschiedlichen Betrachtungswinkeln aufgenommen werden (Abbildung 8). Diese ermöglichen eine direkte Visualisierung der Nanostruktur der Probe.

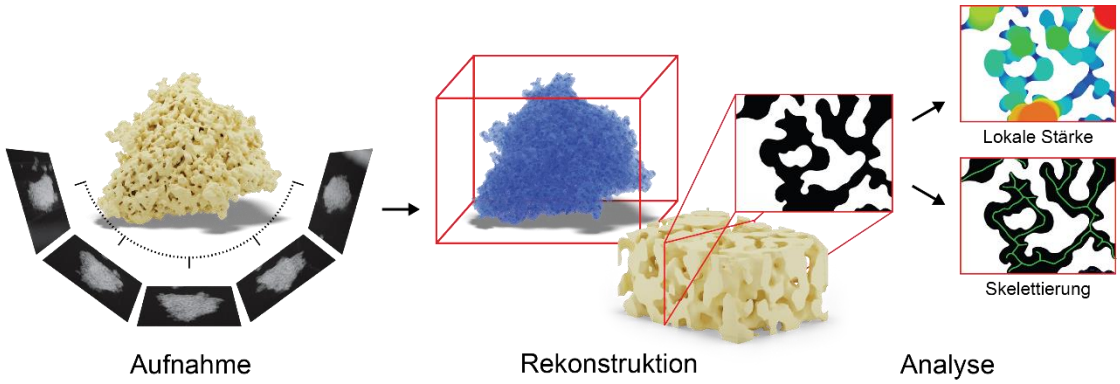

Abbildung 8. Schematische Darstellung des Analyseprozesses mittels Elektronentomographie.

Neben einem besseren Verständnis der dreidimensionalen Struktur durch diese Visualisierung stellt die quantitative morphologische Analyse der Rekonstruktionen einen weiteren wichtigen Bestandteil der Analyse mittels Elektronentomographie dar. So lässt sich zum Beispiel anhand zahlreicher unterschiedlicher Methoden eine detaillierte quantitative Charakterisierung des Porenraumes durchführen.

Eine bewährte Methode ist dabei die sogenannte Skelettierung, ein Verfahren aus der Bildbearbeitung, bei dem der Porenraum iterativ auf eine einen Bildpunkt breite Mittellinie reduziert wird.[68] Das so entstehende Skelett stellt eine topologische Repräsentation des Porenraumes dar. Es besteht aus Knotenpunkten und Ästen, anhand derer zahlreiche Parameter, wie beispielsweise die Koordinationszahl,[69] Porenlängen und -durchmesser sowie die Tortuosität, bestimmt werden können. Ein weiteres Verfahren aus der Bildbearbeitung, welches zur Bestimmung von Porendurchmessern eingesetzt werden kann, ist die „Local Thickness“-Methode.[70] Diese beschreibt die lokale Stärke einer Struktur als den größten Durchmesser einer Kugel, welche in die Struktur hinein passt und den betrachteten Bildpunkt enthält. Ein besonderer Vorteil der Elektronentomographie ist dabei, dass die Rekonstruktionen die Informationen beider Phasen beinhaltet. Da die beschriebenen Bildverarbeitungsverfahren mit binären Daten – typischerweise weiß für die feste Phase und schwarz für den Hintergrund beziehungsweise die Poren – arbeiten, lässt sich so neben dem Porenraum auch die feste Phase analysieren. Die lokale Stärke beschreibt dann anstatt des Porendurchmessers die Wandstärke.

In der Materialforschung ist die Elektronentomographie insbesondere für die Charakterisierung ungeordnet mesoporöser Materialien von Bedeutung. Ein Beispiel

dafür ist die Arbeit von Stöckel *et al.*, in der die Mesoporenkonnektivität von meso- und makroporösen Silicamonolithen untersucht wurde.[66] Die Autoren präsentieren ein Charakterisierungsverfahren, in dem sie Struktureigenschaften der hierarchisch porösen Silicamonolithe mit Transporteigenschaften, wie beispielsweise der effektiven Diffusion, verknüpfen. Hochstrasser *et al.* untersuchten Transporteigenschaften in SBA-15 und KIT-6 mittels Elektronentomographie.[67] Mithilfe numerischer Simulation konnte eine quantitative Größe ermittelt werden, welche die Hinderung der Diffusion innerhalb des Porenraumes in Bezug zur Bulkdiffusion setzt. Das Verfahren soll so einen direkten Vergleich zwischen ungeordnet und geordnet mesoporöser Materialien ermöglichen. Özkan *et al.*[44] kombinieren in ihrer in Abschnitt 2.2.2 erwähnten Publikation zu mittels Hydrothermalsynthese synthetisiertem mesoporösem CeO_2 zudem eine detaillierte Physisorptionsanalyse einschließlich Hysterese-Scanning mit morphologischer Analyse des Mesoporenraumes mithilfe von Elektronentomographie.

3 Publikationen

Das Ziel der vorliegenden Dissertation ist die Aufklärung von Zusammenhängen zwischen Syntheseparametern und der Struktur des Mesoporenraumes dotierter CZOs und die Weiterentwicklung geeigneter Charakterisierungsverfahren. Strukturelle Änderungen im Mesoporenraum sollen mit Syntheseparametern verknüpft werden und durch ein verbessertes Verständnis ablaufender Prozesse, zum Beispiel beim Sintern bei hohen Temperaturen, dazu genutzt werden Materialeigenschaften gezielt zu steuern und zu optimieren. Um dieses Ziel zu erreichen, wurde der Ansatz von Özkan *et al.*[44] gewählt und auf eine industriell relevante und komplexe Zusammensetzung des Mischoxides übertragen.

Besonderes Augenmerk sollte zudem auf die Konnektivität der Mesoporen gelegt werden, welche einen maßgeblichen Einfluss auf die im Inneren des Porenraumes stattfindenden Transportprozesse haben. Mithilfe von mittels Elektronentomographie erzeugter dreidimensionaler Rekonstruktionen des Mesoporenraumes sollte ein besseres Verständnis der durch Hysterese-Scanning ermittelten Desorptions-Scanning Isothermen erreicht und ihre Interpretation in Zukunft vereinfacht werden.

Die dieser Dissertation zugrundeliegenden Publikationen stellen eine schrittweise Bearbeitung dieser Fragestellung dar und thematisieren die Synthese und Charakterisierung von industriell relevanten Katalysatormotiven sowie die Einflüsse der zugrundeliegenden Syntheseparameter auf den Mesoporenraum. Die erste Publikation (3.1) befasst sich dabei mit der Übertragung der Synthese nach Ohtake *et al.*[43] auf ein quaternäres Mischoxidsystem und der Entwicklung des Porenraumes während Kalzinierung und Alterung. Zusätzlich wurde der Einfluss von an die Oberfläche gebundenen Nitratgruppen auf das Sinterverhalten der Primärpartikel und damit auf das Mesoporennetzwerk untersucht. Im Rahmen der zweiten Publikation (3.2) wurde die Synthese um einen hydrothermalen Nachbehandlungsschritt in wässriger Ammoniaklösung ergänzt und eine detaillierte Untersuchung dessen Effekts auf die Konnektivität des Mesoporennetzwerkes mithilfe von Hysterese-Scanning Experimenten durchgeführt. Die Interpretation der Daten wurde mit mittels Elektronentomographie erzeugter dreidimensionaler Rekonstruktionen des Mesoporenraumes untermauert. Die dritte Publikation (3.3) beschäftigt sich

tiefergehend mit dem Einfluss der Bedingungen während der hydrothermalen Nachbehandlung auf die Entwicklung des Porenraumes. Die Mesoporenkonnektivität und thermische Stabilität der Mischoxide wurde durch systematische Variation der Parameter in Abhängigkeit der Synthesebedingungen studiert. Besonderes Augenmerk lag dabei auf den chemischen Prozessen während der Synthese, die zu einem veränderten Sinterverhalten und so zu einer erhöhten thermischen Stabilität der Materialien führen.

3.1 Development of Pore Morphology During Nitrate Group Removal by Calcination of Mesoporous $Ce_xZr_{1-x-y-z}Y_yLa_zO_{2-\delta}$ Powders

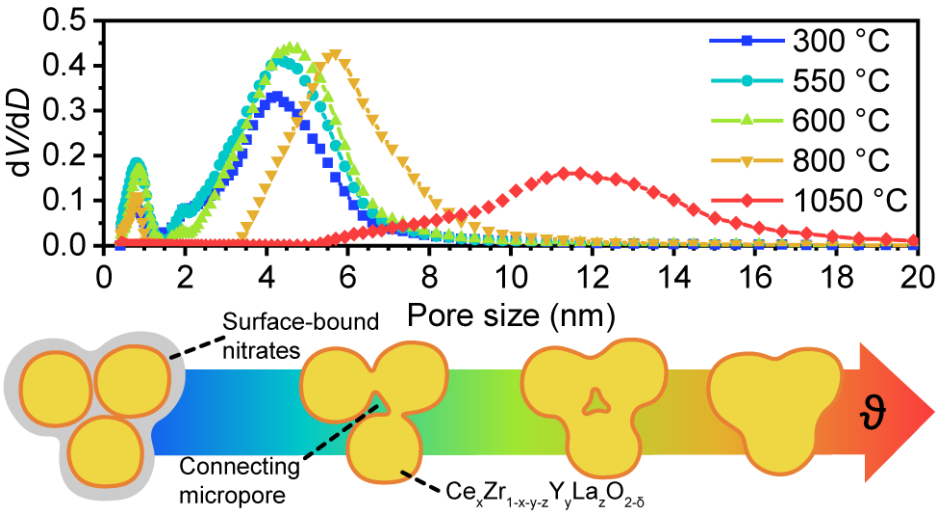

Reprinted with permission from

Prates da Costa, E., Hofmann, A., Göbel, U., Cop, P., Smarsly, B. M. Development of Pore Morphology During Nitrate Group Removal by Calcination of Mesoporous $Ce_xZr_{1-x-y-z}Y_yLa_zO_{2-\delta}$ Powders, *Langmuir* **2022,** *38*, 8342–8352.

DOI: 10.1021/acs.langmuir.2c00875

LANGMUIR

pubs.acs.org/Langmuir Article

Development of Pore Morphology During Nitrate Group Removal by Calcination of Mesoporous $Ce_xZr_{1-x-y-z}Y_yLa_zO_{2-\delta}$ Powders

Eric Prates da Costa, Alexander Hofmann, Ulrich Göbel, Pascal Cop, and Bernd M. Smarsly*

Cite This: *Langmuir* 2022, 38, 8342−8352 Read Online

ACCESS | Metrics & More | Article Recommendations | Supporting Information

ABSTRACT: Here, we present a study of the development of the micro- and mesoporosity of a $Ce_xZr_{1-x-y-z}Y_yLa_zO_{2-\delta}$ oxygen storage material upon treatment at temperatures up to 1050 °C. The investigated powder, obtained from nitrate-based metal oxide precursors in a specially developed hydrothermal synthesis, is highly crystalline, features a high surface area and does not show phase segregation at high temperatures. By employing an advanced methodology, consisting of state-of-the-art argon physisorption, thermogravimetric analysis coupled with mass spectrometry (TG-MS) and X-ray powder diffraction (XRD) along with Raman spectroscopy, we correlate the stability of the mesopore system to the presence of surface-bound nitrate groups introduced during synthesis, which prevent sintering up to a temperature of 600 °C. In addition, the connectivity of mesopores was further studied by hysteresis scanning within the argon physisorption measurements. These advanced physisorption experiments suggest a three-dimensionally interconnected pore system and, in turn, a 3D network of the material itself on the nanometer scale which appears to be beneficial to endow the mesopore space with enhanced stability against sintering and mesopore collapse once the removal of nitrate groups is completed.

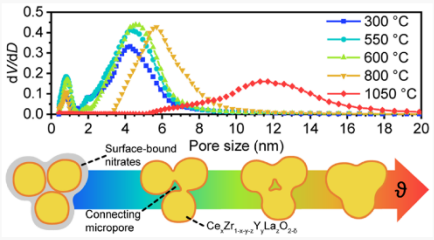

INTRODUCTION

Ceria-based materials find broad application in many catalytic processes,[1] ranging from CO oxidation and solar thermochemical hydrogen production[2] to water gas shift reaction, but they are most commonly found as oxygen storage materials (OSM) in three-way catalysis (TWC). There they are employed to compensate for fluctuations in exhaust gas composition, in order to ensure optimum conversion of hazardous gases.[3] This property originates from the highly reversible redox chemistry of cerium, which allows for reversible and fast switching between the Ce^{3+} and Ce^{4+} oxidation states upon incorporation or release of oxygen from its fluorite type crystal lattice. Commonly pure ceria suffers from severe sintering and therefore loss of surface area upon exposure to high temperatures.[4] Enhanced stability can be achieved for instance by using mixed oxides instead of pure ceria, for example, with ZrO_2, while simultaneously decreasing the enthalpy for oxygen vacancy formation and increasing the mobility of oxygen-ions due to the smaller Zr^{4+} ions.[5] Unfortunately, the resulting materials, although being more resilient against sintering and loss of surface area, suffer from phase segregation at elevated temperatures. To mitigate this phase segregation trivalent dopants like Y^{3+} or La^{3+} are commonly added. Besides the composition the synthetic route is a crucial factor for the properties of the resulting mixed oxides. Hence, many procedures, like mechanical ball-milling,[6] hard-[7] and soft-templating, coprecipitation[8−10] or hydrothermal synthesis,[11−13] have been developed to finetune the obtained materials for their intended application. Often high specific surface areas are desired to improve catalytic capabilities, which must withstand elevated temperatures (up to 1100 °C) to prevent losses in catalyst activity over long-term operation. For example, this demand is of special concern in TWC, where platinum group metals (PGMs) are dispersed on the OSMs as the catalytically active compound. The high and strongly fluctuating prices due to availability of those metals (e.g., Rhodium) make low PGM contents favorable from a cost perspective. However, due to reduction of porosity upon exposure to high temperatures and harsh conditions in the exhaust gas stream, the risk of entrapment of those PGMs in collapsing pores arises, resulting in an unwanted eventual reduction of accessible active sites (cf. Scheme 1). These circumstances require a deep understanding of the processes involved in thermal alteration and possibly even degradation of the mixed metal oxides for the design of highly performant and long-lasting catalyst materials. However, common analyses performed in literature are limited to simple comparisons of specific surface area determined by the Brunauer−Emmett−Teller (BET) method and mean pore diameters of ternary mixed oxides before and after exposure to high temper-

Received: April 4, 2022
Revised: June 10, 2022
Published: June 30, 2022

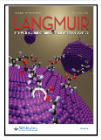

https://doi.org/10.1021/acs.langmuir.2c00875
Langmuir 2022, 38, 8342−8352

Scheme 1. Interplay of High BET Areas and Pore Connectivity in a Three-Way Catalytic Converter[a]

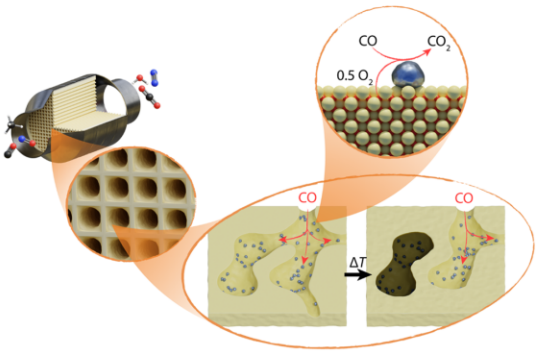

[a]High BET areas are required for an optimal precious metal (metallic blue dots) dispersion, and good pore interconnectivity is beneficial for the accessibility of catalytically active sites.

atures,[11,12,14−16] neglecting the importance of pore connectivity and accessibility.

In a previous study on pure ceria, obtained by thermal hydrolysis of ammonium cerium(IV) nitrate, the influence of surface-bound nitrate groups introduced during synthesis and their removal by calcination was found to be a crucial factor in the development of the material's mesopore space and thermal stability.[17] For complex mixed oxides like they are commonly applied in TWC, however, the role of surface-bound nitrate groups introduced during synthesis has not yet been studied in detail. Here, due to possibly different bond-strengths between the nitrate groups and the various metal oxides, the effects on the development of the pore space might differ drastically, resulting in a different sintering behavior. Hence, the importance of surface-bound nitrate moities could also be relevant to other mixed oxides typically accessed by wet-chemical procedures based on nitrate-precursors. Subject of this work are quaternary $Ce_xZr_{1-x-y-z}Y_yLa_zO_{2-\delta}$ mixed oxides, which are compositionally equivalent to commercially available oxygen storage materials applied in TWC. The nanocrystalline and mesoporous powders featuring a disordered pore network were obtained via thermal hydrolysis of ammonium cerium-(IV) nitrate, zirconium oxynitrate and yttrium and lanthanum nitrate based on the method described by Ohtake et al.[12] The materials were analyzed by X-ray diffraction (XRD) and Raman spectroscopy to elucidate the phase composition and crystallite size. Scanning electron microscopy (SEM) was performed to analyze the materials' microscale morphology. The mesoporosity was analyzed by state-of-the-art argon physisorption to calculate surface areas and pore size distributions. In particular, advanced hysteresis scanning was performed to investigate the mesopore connectivity. This method allows for identifying restriction in the mesopore connectivity (pore blocking, cavitation), thus providing invaluable insight into fine alterations in the mesopore space. Thermogravimetric analysis coupled with mass spectrometry (TG-MS) was used to track the removal of nitrate groups, and a detailed study on its effects on the morphology was conducted in combination with the aforementioned methods at different stages during calcination. This combination of methods allows for the direct correlation of chemical processes like the removal of surface-bound -NO_3 to sintering processes, morphological changes, changes in the mesopore space and phase transformations occurring throughout calcination. This conceptual methodology and the gained insights into the calcination behavior of nanocrystalline quaternary mixed oxides should provide the deep understanding required to optimize synthesis procedures to yield highly stable and performant oxygen storage materials, keeping significant mesoporosity even at high temperatures up to 1100 °C.

MATERIALS AND METHODS

Preparation of $Ce_xZr_{1-x-y-z}Y_yLa_zO_{2-\delta}$ Powders. The synthesis procedure for the mixed oxides was adapted from Ohtake et al.[12] and modified with respect to the metal compounds used as precursors for the metal oxides. An aqueous solution of $(NH_4)_2[Ce(NO_3)_6]$ (99.1%, Treibacher Industrie AG), $ZrO(NO_3)_2$ (20 wt % aq. Solution, >98%, Luxfer MEL Technologies), $Y(NO_3)_3 \cdot 6H_2O$ (>99%, Treibacher Industrie AG), and $La(NO_3)_3{\cdot}6H_2O$ (≥99.99%, Carl Roth GmbH + Co. KG) with a molar ratio of Ce^{4+}:ZrO^{2+}:Y^{3+}:La^{3+} = 0.18:0.64:0.15:0.03 and a total metal ion concentration of 0.464 mol·L^{-1} was heated to 150 °C for 8 h in a stirred autoclave preloaded with compressed air at a pressure of 2 bar. Following the hydrothermal treatment of the solution the pH was adjusted to 8 by the addition of aqueous ammonia (25 wt %) and the obtained precipitate was filtered and subsequently dried at 80 °C for 18 h. The resulting pale-yellow powder was calcined in air at 400 °C for 10 h (10A400). Subsequent aging of the powders was performed at 1050 °C for 4 h in ambient air (4A1050). The heating rate during calcination and aging was 5 °C min^{-1}. Also, a binary mixed oxide was produced analogously with a molar ratio of Ce^{4+}:ZrO^{2+}(:Y^{3+}:La^{3+}) = 0.18:0.72(:0:0).

Characterization. *Physisorption.* Measurements of argon physisorption isotherms and hysteresis scans were performed at 87 K on an autosorb iQ2 automated gas sorption analyzer (Quantachrome Instruments). Before measuring, all samples were degassed under vacuum at 80 °C for 18 h without further pretreatment. Surface areas and pore size distributions were calculated by the accompanying software ASiQwin (Version 4.0, Quantachrome Corporation). The specific surface area was calculated by Brunauer−Emmett−Teller (BET) method in a pressure range of p/p_0 = 0.05−0.30. Pore size distributions and also specific surface areas were determined by the application of a nonlocalized density functional theory (NLDFT) kernel of argon on zeolites/silica at 87 K to the adsorption/desorption branch of the isotherm, assuming a cylindrical pore geometry.

ICP-OES. The chemical composition of the powders was determined by inductively coupled plasma optical emission spectrometry on a Varian 725-ES (Agilent Technologies). Therefore, the powders were solubilized in different acids (HCl, HNO_3, HF) and the elemental concentration was measured against a matrix-adjusted standard solution of the analyte.

TGA-MS. Thermogravimetric analysis was conducted on a STA409 PC Luxx thermogravimetric analyzer (Netzsch) over a temperature range from 25 to 1050 °C with a heating rate of 5 have °C min^{-1} in synthetic air (80% N_2, 20% O_2). Mass spectra were recorded simultaneously on a QMS 403 Aëolos Quadro quadrupole mass spectrometer (Netzsch) in a m/z range of 12−100.

XRD. Powder diffraction was performed with Cu−Kα radiation on an Empyrean diffractometer (PANalytical), operated at a voltage of 40 kV and an output current of 40 mA. The diffractograms were fitted with HighScore Plus (Version 3.0.5, PANalytical) and Crystallite sizes were calculated by Scherrer equation.

Raman Spectroscopy. Raman spectra were recorded on a Senterra Raman spectrometer (Bruker) with a Nd:YAG laser (λ = 532 nm, 2 mW) and a resolution of 3−5 cm^{-1}.

SEM. Scanning electron microscopy was carried out on a MERLIN electron microscope (Carl Zeiss) with an acceleration voltage of 3 kV and a sample current of 78 pA. All samples were sputtered with platinum for 60 s prior to the measurement.

https://doi.org/10.1021/acs.langmuir.2c00875
Langmuir 2022, 38, 8342−8352

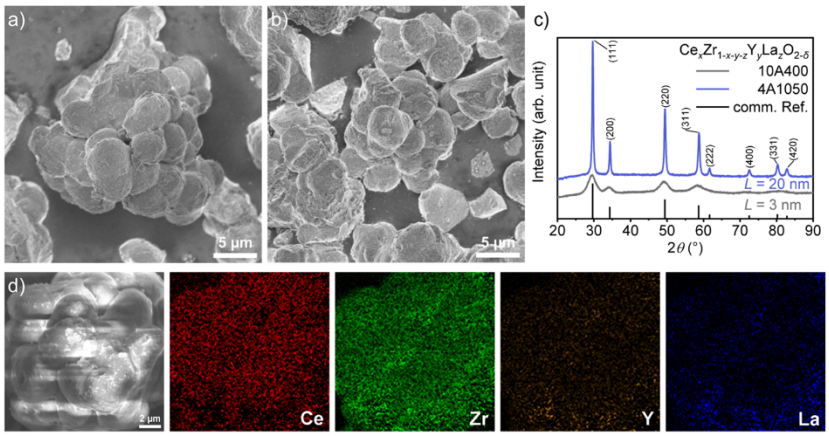

Figure 1. SEM images of the 10A400 (a) and 4A1050 (b) particles, revealing the spherical shape of the agglomerated secondary particles. (c) XRD patterns of the powder calcined at 400 °C (10A400) and subsequently aged at 1050 °C (4A1050), as well as the position of the reflections of the commercial reference. (d) Distribution maps of the contained metal ions obtained from EDX of a 10A400 particle.

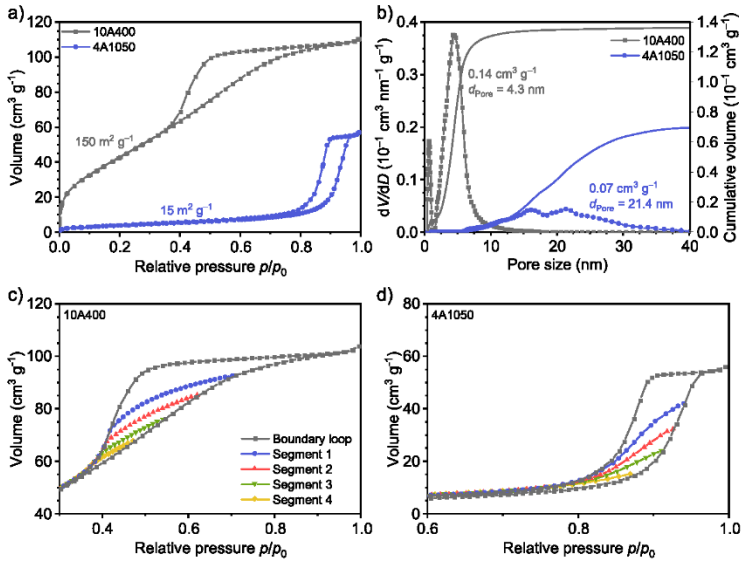

Figure 2. Argon isotherms (87 K) of the calcined and aged powders (a) and the corresponding pore size distributions (b) obtained by NLDFT and the corresponding Ar-hysteresis scans (c) and (d).

EDX. Energy-dispersive X-ray spectroscopy was performed with an X-Max 50 detector (Oxford Instruments) at a working distance of 5 mm, an acceleration voltage of 10 keV and a sample current of 2.2 nA.

XPS. X-ray photoelectron spectroscopy was conducted on a PHI 5000 VersaProbe II (Physical Electronics GmbH). For the samples heated to specific temperatures which were to be analyzed for the content of Ce^{3+} a short measurement time of 20 min was chosen, to mitigate the possible release of oxygen from the oxygen storage material during measurement. Compositional analysis was performed on the sample calcined for 10 h at 400 °C, by fitting the corresponding signals of the contained metals in the survey-spectrum. The molar ratio was calculated from the ratio of peak areas to the total peak area of all signals. All recorded spectra were calibrated to the binding energy of the Ce^{4+} 3d u‴ signal at 916.7 eV with CasaXPS (Ver. 2.3.18, Casa Software Ltd.). To determine the Ce^{3+} content the spectra were subsequently fitted by considering six Ce^{4+} 3d (v, v″, v‴ and u, u″, u‴) and four Ce^{3+} 3d (v_0, v′, and u_0, u′) signals.[18] A combination of two fits was employed to improve the fit quality of the u and v signals, based on Skála et al.[19]

■ RESULTS AND DISCUSSION

The synthesized powder was analyzed by ICP-OES, XPS, and EDX measurements, from which a composition of $Ce_{0.20}Zr_{0.63}Y_{0.14}La_{0.03}O_{2-\delta}$ was determined, being in agreement with the targeted composition of a commercial reference material of $Ce_{0.18}Zr_{0.64}Y_{0.15}La_{0.03}O_{2-\delta}$. The uniform distribution of the colors shown in Figure 1d evidence a homogeneous distribution of the different metals. Investigating on the morphology of the synthesized material, SEM images (Figure 1a,b) reveal a special microstructure of agglomerated spherical

https://doi.org/10.1021/acs.langmuir.2c00875
Langmuir 2022, 38, 8342−8352

particles with diameters of ca. 5 μm. XRD patterns (Figure 1c) feature the reflections of a fluorite-type cubic phase, which even after aging at high temperatures do not indicate any phase segregation, proving the stabilizing effect of adding La and Y to the Ce−Zr mixed oxide. Furthermore, the material is comprised of small primary particles with an average crystallite size of about 3 nm, as calculated by the Scherrer equation applied on the (220) reflection. Hence, broad reflections are observed prior to high temperature treatment. According to XPS data (Supporting Information (SI) Figure S1) Ce is predominantly present as Ce^{4+}, while the total amount of Ce^{3+} is on the order of the detection limit (ca. 1−2 at%), as the fits of the observed bands in the Ce 3d region prove.[20]

Argon physisorption (87 K) was employed to characterize the porosity of the powders (Figure 2 and SI Table S1). The isotherm can be assigned to a type IV isotherm according to IUPAC.[21] It features a hysteresis loop of type H2, indicating the presence of pronounced network effects. A BET area of 150 $m^2\ g^{-1}$ was calculated for the calcined (10A400) powder. The pore size distribution ranges from 1−10 nm with a mean pore size of 4.3 nm and a mesopore volume of 0.14 $cm^3\ g^{-1}$. Upon aging (4A1050), the spherical secondary structure remains intact, as the comparison of SEM images reveals. Mesoporosity, however, is affected drastically as the BET area is reduced by 90% to a value of 15 $m^2\ g^{-1}$ and the mesopore volume by 50% to 0.07 $cm^3\ g^{-1}$. The pore size distribution shows an increase in mesopore sizes and distribution width, ranging from 5−30 nm with a mean pore diameter of 21.4 nm. This change in pore dimension is accompanied by an increase in average crystallite size to 20 nm as determined from XRD. Furthermore, a change in pore connectivity after aging is observed from advanced physisorption experiments (Figure 2c,d), as described in detail below.

TG-MS was performed using synthetic air to analyze the removal of different chemical species during calcination (Figure 3). The only relevant signal intensities were found among various nitrous oxide species, also depicted in Figure 3. Besides the nitrous oxides a relevant fraction of the mass loss is related to the loss of water or ammonium-ions. Here, significant amounts of CO_2 (m/z = 44) or CO (m/z = 28), possibly originating from carbon-based species, could be excluded, as no intensity was observed for the C^+-fragment-ion (m/z = 12), which forms during electron impact ionization of CO_2 or CO. The total mass loss during heat treatment can be divided into four different regions. In the first phase below 200 °C mostly physiosorbed water is removed from the sample, accounting for a 6% loss in mass. Between 250 and 300 °C, the second region, a strong signal of N_2O^+ and NO^+ was detected, which is most likely related to the decomposition of NH_4NO_3, which is accompanied by a mass loss of 2−3%. In the third phase, ranging from 300 to 600 °C, a broad signal originating from NO^+ and NO_2^+ was observed. These correspond to the desorption and decomposition of -NO_3, related to a mass loss of 9%. The last region is characterized by a decrease in sample mass by approximately 1% at temperatures above 600 °C. No signal intensity for NO^+ and NO_2^+ ions was detected in this range, indicating that nitrate desorption is completed at 600 °C. To investigate the influence of the nitrate group decomposition on crystallite growth and the pore structure during calcination, the samples were heated in air with the same heating rate as in the TG-MS experiment and removed from the oven once the targeted temperature was reached. The samples were then each analyzed by XRD, Raman spectroscopy, and argon physisorption, thus providing insight into the alterations in structure, composition and pore space occurring at the different temperatures.

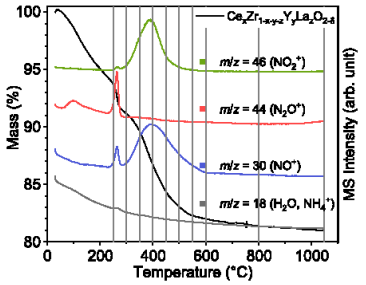

Figure 3. TG-MS analysis of the powder dried at 80 °C without calcination. The intensities of the MS signals are normalized to the maximum. The vertical lines indicate the temperatures, at which the samples were subjected to detailed analyses (see Figure 4 and SI Table S2).

Figure 4 shows the obtained argon isotherms at selected temperatures normalized to the actual mass of metal oxide, as determined from the end point of the TG-MS experiment. All isotherms can be assigned to the type IV isotherm with a hysteresis loop of type H2. Upon increase in temperature a rise in the total adsorbed volume is observed, which reaches a maximum at a temperature of 600 °C. From this point on, the total adsorbed volume starts to decrease, accompanied by a shift of the hysteresis loop, originally located between a relative pressure of 0.4−0.8, to higher relative pressures between 0.7 and 0.9 at a temperature of 1050 °C.

Also shown in Figure 4 are the corresponding NLDFT pore size distributions, revealing two pore populations in the micro- and mesopore range. The mesopore sizes range from ca. 2−6 nm with some pores ranging up to 10 nm. This population has the highest contribution to the pore volume, as the NLDFT analysis reveals after separation into pores smaller and larger than 2 nm (Figure 4, bottom right). The majority of the micropores is located in a range of 0.5−1.5 nm. This population shows a strong increase in pore volume upon heat treatment up to 500 °C, where a maximum is reached and the micropore volume starts to reduce and is eventually removed completely at temperatures above 800 °C. Simultaneously, the mesopore volume grows until a temperature of 600 °C is reached. At this point the mesopore dimension starts to shift to larger pore sizes of 3−12 nm at 800 °C and finally 5−20 nm at 1050 °C. Similar behavior is found in the calculated BET areas shown in SI Table S2 and in Figure 4. Here it should be noted that—unlike the NLDFT-derived surface area—the BET-method does not allow the separation between micro- and mesopores, based on the underlying pore diameter as shown in Figure 6 (bottom left). However, it is commonly reported as a fingerprint parameter, and since for the examined samples both methods provide well matching results the BET area forms the basis of the following discussion. First an enlargement of the BET area to 170 $m^2\ g^{-1}$ is observed up to a temperature of 500 °C, followed by a strong reduction to 40 $m^2\ g^{-1}$. These developments of the pore sizes and BET area correlate strongly with the decomposition of -NO_3 observed in TG-MS. It is suggested that the -NO_3

https://doi.org/10.1021/acs.langmuir.2c00875
Langmuir 2022, 38, 8342−8352

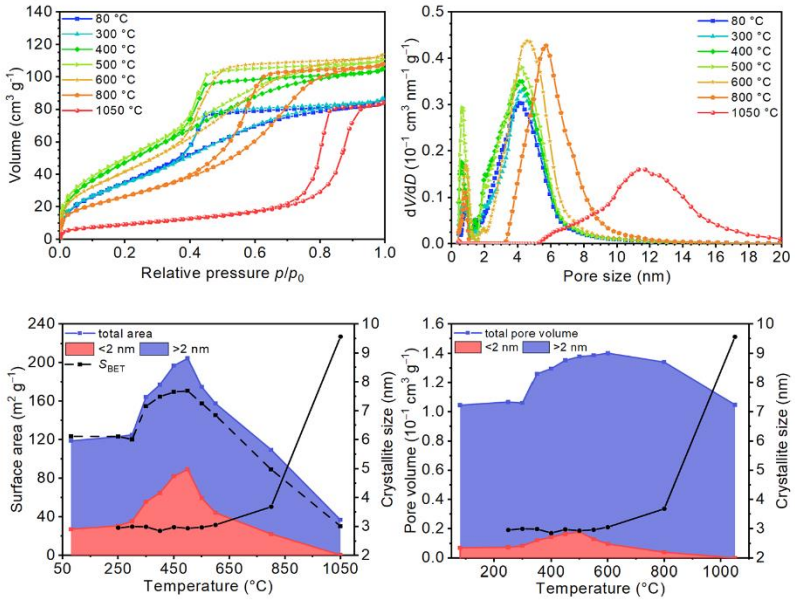

Figure 4. Selected argon isotherms (87 K) and NLDFT pore size distributions of the samples heated to different temperatures. Contribution of micropores pores (<2 nm) and mesopores (>2 nm) to the total surface area and pore volume calculated by NLDFT in comparison to the temperature-dependent crystallite size.

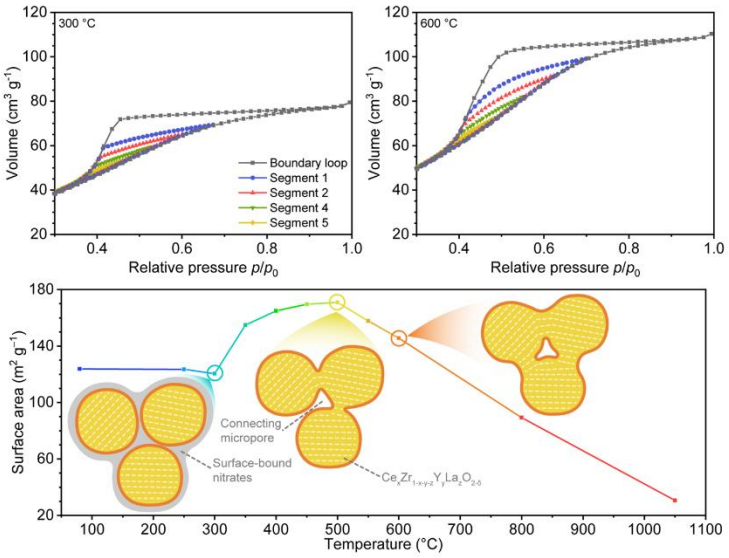

Figure 5. Argon hysteresis scans (87 K) of the samples heated to (a) 300 °C and (b) 600 °C. (c) Schematic representation of micropore generation, development of BET area, and sintering during and after -NO_3 removal.

groups prevent sintering processes, as an increase in crystallite size is only observed after the removal is completed. Note that the mass fraction of NO_x-species is quite significant, amounting to ca. 10 wt % (Figure 3), which means that the removal exerts a significant impact on the material. This is in agreement with previously reported results[17] on ceria powders prepared under similar conditions. Figure 5 depicts a schematic representation of the processes of nitrate removal, pore evolution, and the onset of sintering and their connection to the BET area and pore connectivity, determined by physisorption measurements. The development of the micropore population and the initial increase in BET area suggest that most of the nitrate groups are located in micropores and their removal hence increases the micropore volume, which in fact can also be interpreted as the void volume between the primary particles. Once the nitrate groups are removed, small

https://doi.org/10.1021/acs.langmuir.2c00875
Langmuir 2022, 38, 8342−8352

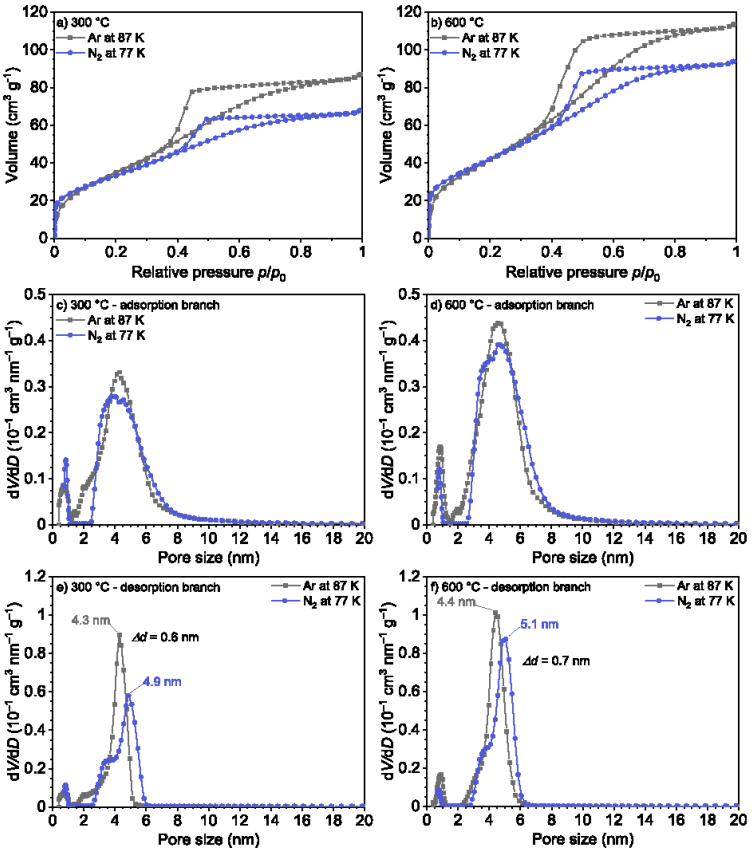

Figure 6. Nitrogen (77 K) and argon (87 K) isotherms of the samples heated to (a) 300 °C and (b) 600 °C and resulting pore size distributions for the adsorption (c,d) and desorption branches (e,f), obtained by application of the corresponding NLDFT kernel. See SI Figure S3 for a comparison of the NLDFT fit quality.

pores collapse and mass transport between particles is no longer hindered, resulting in the observed growth and fusion of pores and crystallites.

To investigate on the mesopore connectivity hysteresis scanning was employed. In this special type of physisorption experiment multiple cycles of adsorption and desorption are performed. Therefore, the relative pressure at which desorption is started is lowered in a stepwise fashion and the desorption branch is measured. By the shape of the desorption branches the underlying desorption mechanism can be deduced.[22,23] This method was applied to the samples heated to 300 and 600 °C, which correspond to the temperatures and states before and after nitrate group decay and removal. The resulting isotherms (Figure 5a,b) are evidence for a drastic change in desorption behavior and hence indicative for changes in the connectivity between mesopores. In the sample heated to 300 °C the scanning segments reveal only moderate desorption upon the decrease of the relative pressure until the boundary loop is met. From this point on the scanning curve follows the boundary isotherm. This kind of behavior is expected from materials either featuring independent pores, like in SBA-15 or MCM-41 type materials,[22] or materials where desorption from pores is hindered by cavitation. It differs significantly from the desorption behavior in the sample heated to 600 °C. Here, the scanning curves show a stronger desorption upon decreasing p/p_0. The curves meet the boundary isotherm almost in a single point as expected for materials in which network effects like pore blocking or percolation occur.[22] As both samples exhibit behavior characteristic for cavitation and network percolation, it is suggested that both are involved in the desorption to different extends and that the removal of -NO_3s from the mesopores introduces additional connections between pores, enabling the desorption through neighboring, already emptied pores. After heating to 1050 °C the scanning isotherms (SI Figure S2) qualitatively possess the same shape as the aged sample's (4A1050) isotherms in Figure 2d. The major difference is the lower overall adsorbed volume due to the longer holding time of the actual aging procedure. The sample heated to 600 °C, after complete removal of nitrate groups, is almost identical to the sample calcined for 10 h at 400 °C (see SI Figure S2 for a direct comparison of the scanning experiments).

The involved mechanisms of desorption can be distinguished by comparison of physisorption data from measurements with different adsorptives.[24] In essence, the comparison of the pore size distribution (PSD) calculated from the adsorption as well as the desorption branches, derived, for example, from nitrogen and argon, allows for a discrimination

https://doi.org/10.1021/acs.langmuir.2c00875
Langmuir 2022, 38, 8342−8352

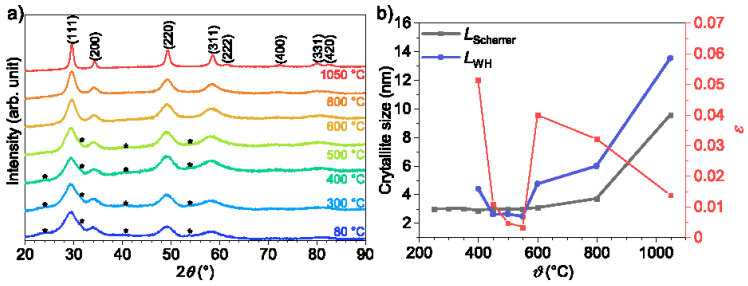

Figure 7. XRD patterns of the samples at different heating stages (a). Development of crystallite sizes calculated by Scherrer equation and separation of crystallite size and strain (b) over increasing temperatures.

between pore emptying mechanisms and, hence, the corresponding connection between mesopores. In Figure 6 the argon and nitrogen isotherms of the scanned samples are shown along with the calculated pore size distributions. The calculated BET area for the sample heated to 300 °C is 120 m^2 g^{-1} with both adsorptives. For the sample treated at 600 °C the BET area calculated from the measurement with nitrogen is 155 m^2 g^{-1} and therefore 10 m^2 g^{-1} higher than the BET area calculated from the argon isotherm. This difference, however, is not an uncommon observation when comparing BET areas of metal oxides measured with Ar or N_2. The PSDs of the sample heated to 300 °C obtained from the adsorption branch are expectedly almost identical for both adsorptives (Figure 6c). In contrast to that, the PSDs calculated from the desorption branches for both, nitrogen and argon, are a lot sharper and shifted slightly to smaller pore sizes (Figure 6e) compared to the respective pore size distribution from the adsorption branch. This feature is indicative for mesopores the emptying of which upon decreasing relative pressure is hindered, for example, by very narrow pore necks. A maximum is found in the desorption-derived PSD from argon physisorption at a pore size of 4.3 nm, which is 0.6 nm smaller than in the PSD obtained from nitrogen desorption (4.9 nm). Although the difference between the maxima of the desorption-based PSDs of 0.6 nm is rather small, this difference is significant and characteristic for cavitation, where the apparent neck size depends on the adsorptive, rather than on pore geometry alone. However, cavitation in pores of this size range can only be explained by very small connecting pores, which means the majority of mesopores must empty through micropores. In comparison to that, the sample heated to 600 °C features maxima in the desorption-derived PSDs at 4.4 nm (Ar) and 5.1 nm (N_2), as shown in Figure 6f. Here, the difference in shape of the desorption-derived PSDs is also present, however, it is less pronounced (see SI Table S2). Furthermore, the removal of nitrate groups generates additional micropores which in turn provide additional desorption pathways, explaining the steeper slope of the scanning segments. Hence, the physisorption analysis, using different adsorptives, supports the previous suggestions of involvement of both cavitation and network percolation effects with different magnitude based on the treatment temperature.

The XRD patterns of the samples heated to different temperatures are shown in Figure 7a. The sample heated to 1050 °C exhibits the reflection pattern of the fluorite type phase (*c*-phase) or *t*″-phase, which is stabilized by trivalent dopants like Y^{3+} and La^{3+}.[11] The samples subjected to temperatures lower than 550 °C also feature broad low-intensity reflections, indicating the presence of an additional monoclinic phase. With increasing temperature, the width of the reflections assigned to the *c*- or *t*″-phase decreases, indicating the growth of the crystallites after -NO_3 removal. At the same time the reflections assigned to the *m*-phase disappear. The crystallite sizes were calculated by application of the Scherrer equation (eq 1) on the (220) reflection at $2\theta = 49°$ (SI Table S2) on fitted XRD patterns.

$$L_{Scherrer} = \frac{K \cdot \lambda}{FWHM \cdot \cos\theta} \tag{1}$$

As the Scherrer equation does not take line broadening due to crystallite strain into account, a separation of crystallite size and strain was performed by a Willamson-Hall-plot. Therefore, the integral breadth β_{hkl} of the reflections is determined from the XRD patterns and plotted against the corresponding scattering vector s_{hkl}, according to eq (2).

$$\frac{\cos\theta \cdot \beta_{hkl}(S_{hkl})}{\lambda} = \beta_{hkl,0} + \Delta\varepsilon \cdot s_{hkl} \tag{2}$$

with

$$s = \frac{2}{\lambda}\sin\theta \tag{3}$$

Linear regression of the data points provides the strain $\Delta\varepsilon$ as the slope of the line and the true crystallite size L can be calculated from the reciprocal of the intercept (eq 4).

$$L = \frac{1}{\beta_{hkl,0}} \tag{4}$$

Due to the broadness of the reflections caused by the small crystallite size the evaluation was only performed on the (111) and (220) reflections, as these are the only reliably separable reflections. Furthermore, the presence of the monoclinic phase below 550 °C causes a shoulder on the (111)-reflection, which also prevents a reliable separation at lower temperatures. The resulting plot of $\Delta\varepsilon$ along with the average crystallite size against temperature, obtained from the samples heated to 400 °C and above, is shown in Figure 7b.

For all samples a positive $\Delta\varepsilon$ is observed with an overall decrease at higher temperatures, indicating a decrease in strain. Below 600 °C the crystallite size remains constant with minimal strain, which is in good agreement with the size determined by the Scherrer method (see Figure 7b). At 600 °C $\Delta\varepsilon$ increases in a sharp step reaching a maximum and at the same time the crystallites start to grow, which corresponds to

https://doi.org/10.1021/acs.langmuir.2c00875
Langmuir 2022, 38, 8342−8352

the point where all nitrate groups are eliminated. Likely, the reorganization at the particle surface causes the particles to grow together, hence, resulting in the sudden increase in strain. As the decrease of $\Delta\varepsilon$ with increasing temperature indicates, this strain is subsequently reduced. An explanation for this could be an accelerated mass transport at higher temperatures and therewith sintering of the particles. Since the strain contributes to the broadness of the reflections the crystallite sizes obtained via the separation method are slightly larger than via the Scherrer method but follow the same trend.

In the preceding discussion it was assumed that the material remains spatially homogeneous in the composition, that is, that the evolution of the pore space upon temperature treatment is not partially attributable to the segregation of the constituting oxides. To prove the materials' stability against phase segregation a binary mixed oxide without trivalent dopants, whose fractions were substituted by Zr, was prepared under the same conditions and also subjected to aging at 1050 °C. Figure 8a shows the comparison of the XRD patterns and Raman spectra of the investigated $Ce_xZr_{1-x-y-z}Y_yLa_zO_{2-\delta}$ and $Ce_xZr_{1-x}O_2$ after aging at 1050 °C. It is seen that the binary mixed oxide's XRD pattern contains multiple splitting reflections. These are characteristic of the tetragonal zirconia phase, supporting the high stability against phase segregation due to doping of the $Ce_xZr_{1-x-y-z}Y_yLa_zO_{2-\delta}$ with trivalent metal ions. The existence of the tetragonal phase in the binary mixed oxide is proven by the high intensity characteristic Raman modes at 142, 253, 315, 369, 458, and 630 cm^{-1} (Figure 8b).[25]

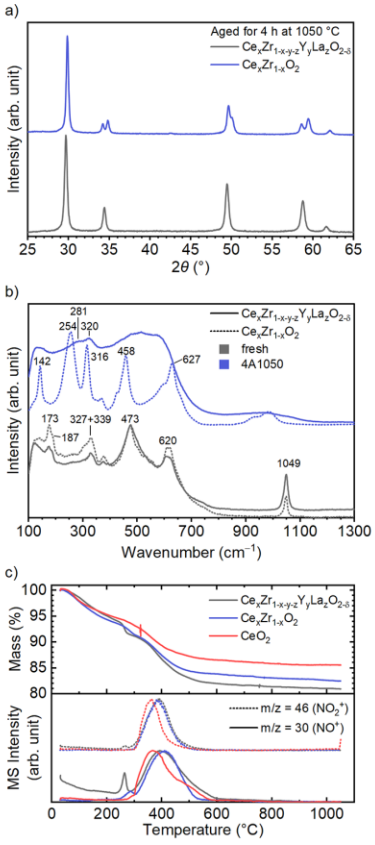

Figure 8. Comparison of the (a) XRD patterns and (b) Raman spectra of the *t*- and metastable *t*''-phase formed during thermal aging of $Ce_xZr_{1-x-y-z}Y_yLa_zO_{2-\delta}$ and $Ce_xZr_{1-x}O_2$ (x = 0.18) at 1050 °C. (c) TG-MS curves of the differently composed mixed oxides and the corresponding MS-intensities of NO^+ and NO_2^+.

Raman spectra (Figure 9) were also recorded for each of the samples which were heated to different temperatures to support the assignment of present phases by XRD. Multiple changes in the Raman bands can be observed during heat treatment, suggesting a phase transformation. First, the strong mode at 1049 cm^{-1} results from the symmetrical stretching of nitrates[26,27] and decreases in intensity with increasing treatment temperature. After a temperature of 550 °C is reached, it vanishes from the Raman spectra. This agrees with TG-MS and corresponds to the temperature, at which the removal of nitrates is completed. The samples treated at temperatures at and below 550 °C exhibit Raman modes at 173, 187, 327, 339, and 379 cm^{-1}, which are indicative of the *m*-phase. Their intensity likewise decreases with increasing temperature, suggesting the transformation of the *m*-phase into the *c*- or *t*''-phase. These findings are in accordance with the XRD analysis (Figure 7). At temperatures above 550 °C five distinct bands are located at 138, 260, 320, 473, and 610 cm^{-1}, which can be assigned to the *t*''-phase.[11,25,28] The bands at 260 and 610 cm^{-1} can be attributed to defects introduced by trivalent doping with Y^{3+} and La^{3+}, the former being the result of the blue-shift of the surface mode due to subsurface oxygen vacancies[29] and the latter resulting from bulk defects.[30] The pronounced mode at 473 cm^{-1}, which is blue-shifted to 479 cm^{-1} at 800 °C and 493 cm^{-1} at 1050 °C belongs to the F_{2g} mode. The origin of this blue shift is likely related to the strong crystallite growth, rather than a change in defect concentration, which generally both affect the position and width of Raman bands.[29,31] Along with this phenomenon a general broadening of the Raman bands takes place at 600 °C and above. However, according to XPS data (Figure 9) ca. 10% of the contained Ce after the nitrate removal is present in the form of Ce^{3+}, which means only a minor amount of additional oxygen vacancies—besides the intrinsic oxygen vacancies present due to the trivalent dopants—is introduced to the material during heating. Due to the low total Ce content of 18%, the overall change in Ce^{3+} content and hence oxygen vacancy concentration is very small, primarily supporting the assumption of a size effect.

Finally, to investigate on the influence of the dopants on the removal of nitrates a TG-MS experiment (Figure 8c) was performed with the corresponding undoped $Ce_xZr_{1-x}O_2$ and pure CeO_2 synthesized under the same conditions. The TG curves differ in their total mass loss depending on the materials composition. While $Ce_xZr_{1-x-y-z}Y_yLa_zO_{2-\delta}$ shows a total mass loss of ~20%, $Ce_xZr_{1-x}O_2$ loses only 18% of its initial mass. The pure CeO_2 sample has the lowest mass loss, amounting to only ~15%. In all samples the mass loss primarily occurs in the temperature range of 150−600 °C, assigned to the decomposition of the -NO_3 groups, as shown above. The MS signals, however, show a clear difference between the pure CeO_2 sample and the zirconium-containing samples in regard to the temperature at which the rate of nitrate removal is highest. While MS-intensities of the quaternary and binary mixed oxides are superimposed and reach their maximum at a temperature of 390 °C, the maximum rate of nitrate removal in

https://doi.org/10.1021/acs.langmuir.2c00875
Langmuir 2022, 38, 8342−8352

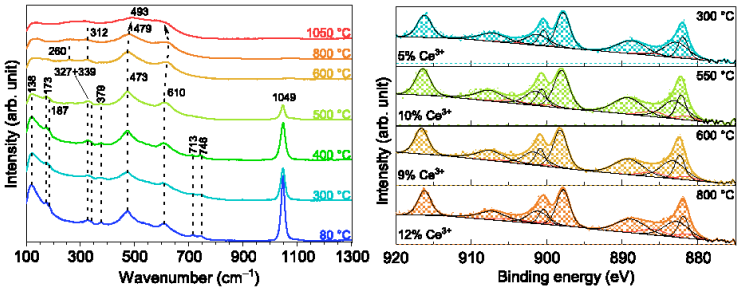

Figure 9. Raman (left) and XPS (right) spectra of the mixed oxides after heating to different temperatures. For the assignment of the bands see SI Figure S1.

the pure CeO_2 sample is shifted by 30 °C to lower temperatures. This suggests a stronger bond between the nitrate groups and zirconium atoms than between nitrate groups and cerium atoms contained in the surface layer. Furthermore, the superimposition of the MS-intensities of the mixed oxides reveals that although Y^{3+} and La^{3+} contribute almost 20% to the total number of metal ions, their presence does not affect the removal temperature.

■ CONCLUSIONS

In this study the chemical and morphological changes induced by thermal treatment at high temperatures of high surface area, nanocrystalline $Ce_xZr_{1-x-y-z}Y_yLa_zO_{2-\delta}$ powders, obtained via a hydrothermal synthesis, were analyzed in-depth with state-of-the-art Ar-physisorption (87 K), SEM, TG-MS, XRD and Raman spectroscopy. Furthermore, advanced physisorption measurements, so-called hysteresis scanning, were performed to investigate on changes in mesopore connectivity upon high temperature treatment.

The obtained material calcined at 400 °C features a high BET area (150 $m^2\ g^{-1}$) and pronounced mesoporosity. XRD combined with Raman spectroscopy evidence the formation of a cubic phase solid solution and a small fraction of a monoclinic phase, which is incorporated into the cubic main phase at elevated temperatures. On the micrometer scale agglomerated spherical secondary particles form, assembled from the single-crystallite primary particles, which remain intact even after prolonged treatment at 1050 °C. The materials' mesoporosity however changes drastically during this treatment. Pores undergo significant growth and a severe loss in BET area is observed—a reduction to 15 $m^2\ g^{-1}$—which is further accompanied by an alteration in the connectivity of the mesopores. While the calcined materials' (10A400) mesopores are connected through small micropores, accessibility of the pores is restricted due to the narrow pore openings, which was observed in the hysteresis scans in the occurrence of cavitation. This effect is diminished upon treatment at temperatures up to 1050 °C, resulting in a highly interconnected and therefore probably more accessible mesopore space. A strong relationship between the beginning of crystallographic and morphological alterations in the mesopore space and the removal of surface-bound nitrates was found in a TG-MS study of the uncalcined dried material. Comparison to pure CeO_2 and $Ce_xZr_{1-x}O_2$ shows that the removal of nitrate moities occurs at higher temperatures in the mixed oxide samples than in pure CeO_2, suggesting a stronger bond of the nitrates to zirconium than to cerium. Trivalent dopants, here yttrium, and lanthanum were investigated; however, they did not affect the temperature at which the removal of the nitrates takes place. Correlating the results from Ar-physisorption, XRD, and Raman spectroscopy to the -NO_3 content, the detailed analysis reveals that nitrate groups are initially located in the micropores, interstitial space between the nanoscale particles, and at the primary particles' surface. There they act as an inhibiting agent impeding sintering processes during early stages of thermal treatment, effectively shielding the crystallites from each other and preventing interparticular mass-transport. Subsequently, upon removal, they leave behind dangling bonds, causing rearrangement at the particle surface, concomitant sintering, and ultimately complete loss of micro- and mesoporosity. Concluding, this study provides valuable insights into the formation and development of mesopores at high temperatures in complex quaternary mixed oxides. The applied methodology, developed previously in our working group, was successfully validated and improved by the use of argon as main adsorptive in physisorption analysis, allowing a detailed analysis of the microporosity and the interconnection of the mesopore space of such irregular mesopore space. This methodology, therefore, was proven to be a powerful tool in the characterization of complex pore morphologies.

■ ASSOCIATED CONTENT

Supporting Information

The Supporting Information is available free of charge at https://pubs.acs.org/doi/10.1021/acs.langmuir.2c00875.

XPS-spectrum of the sample after calcination at 400 °C; tabular porosity data of the powders; tabular comparison of the PSD maxima positions from argon and nitrogen desorption; NLDFT-Fit comparison of the sample calcined at 400 °C for 10 h and the sample heated to 600 °C measured with argon and nitrogen; direct comparison of the hysteresis scans of the sample heated to 600 °C vs calcined at 400 °C (each after the completion of the nitrate-removal) for 10 h and the sample heated to 1050 °C vs aged at 1050 °C for 4 h; Williamson-Hall-plots for the samples heated to different temperatures obtained from the separable (111) and (220)-reflections (PDF)

■ AUTHOR INFORMATION

Corresponding Author

Bernd M. Smarsly − *Institute of Physical Chemistry, Justus-Liebig University, 35392 Giessen, Germany; Center for*

https://doi.org/10.1021/acs.langmuir.2c00875
Langmuir 2022, 38, 8342−8352

Materials Research, 35392 Giessen, Germany; orcid.org/0000-0001-8452-2663; Email: bernd.smarsly@phys.chemie.uni-giessen.de

Authors

Eric Prates da Costa – *Institute of Physical Chemistry, Justus-Liebig University, 35392 Giessen, Germany; Umicore AG & Co. KG, 63457 Hanau, Germany;* orcid.org/0000-0001-8163-7828

Alexander Hofmann – *Umicore AG & Co. KG, 63457 Hanau, Germany;* orcid.org/0000-0001-9872-2156

Ulrich Göbel – *Umicore AG & Co. KG, 63457 Hanau, Germany*

Pascal Cop – *Institute of Physical Chemistry, Justus-Liebig University, 35392 Giessen, Germany*

Complete contact information is available at: https://pubs.acs.org/10.1021/acs.langmuir.2c00875

Author Contributions

The manuscript was written through contributions of all authors. All authors have given approval to the final version of the manuscript.

Notes

The authors declare no competing financial interest.

■ ACKNOWLEDGMENTS

Financial support was provided by Umicore AG & Co. KG. Further acknowledgement goes to the Center of Materials Research (LaMa) at Justus-Liebig University Giessen for the support of this project. Additionally, we acknowledge Tim Weber for the measurement of XPS-spectra.

■ REFERENCES

(1) Devaiah, D.; Reddy, L. H.; Park, S.-E.; Reddy, B. M. Ceria–zirconia mixed oxides: Synthetic methods and applications. *Catal. Rev. Sci. Eng.* **2018**, *60*, 177–277.

(2) Le Gal, A.; Abanades, S.; Bion, N.; Le Mercier, T.; Harlé, V. Reactivity of Doped Ceria-Based Mixed Oxides for Solar Thermochemical Hydrogen Generation via Two-Step Water-Splitting Cycles. *Energy Fuels* **2013**, *27*, 6068–6078.

(3) Farrauto, R. J.; Deeba, M.; Alerasool, S. Gasoline automobile catalysis and its historical journey to cleaner air. *Nat. Catal* **2019**, *2*, 603–613.

(4) Di Monte, R.; Kašpar, J. On the Role of Oxygen Storage in Three-Way Catalysis. *Top. Catal.* **2004**, *28*, 47–57.

(5) Kašpar, J.; Fornasiero, P.; Graziani, M. Use of CeO_2-based oxides in the three-way catalysis. *Catal. Today* **1999**, *50*, 285–298.

(6) Trovarelli, A.; Zamar, F.; Llorca, J.; Leitenburg, C. de; Dolcetti, G.; Kiss, J. T. Nanophase Fluorite-Structured CeO_2–ZrO_2Catalysts Prepared by High-Energy Mechanical Milling. *J. Catal.* **1997**, *169*, 490–502.

(7) Li, H.; Zhang, L.; Dai, H.; He, H. Facile synthesis and unique physicochemical properties of three-dimensionally ordered macroporous magnesium oxide, gamma-alumina, and ceria-zirconia solid solutions with crystalline mesoporous walls. *Inorganic chemistry* **2009**, *48*, 4421–4434.

(8) Reddy, B. M.; Katta, L.; Thrimurthulu, G. Novel Nanocrystalline $Ce_{1-x}La_xO_{2-\delta}$ ($x = 0.2$) Solid Solutions: Structural Characteristics and Catalytic Performance. *Chem. Mater.* **2010**, *22*, 467–475.

(9) Deshpande, A. S.; Pinna, N.; Beato, P.; Antonietti, M.; Niederberger, M. Synthesis and Characterization of Stable and Crystalline $Ce_{1-x}Zr_xO_2$ Nanoparticle Sols. *Chem. Mater.* **2004**, *16*, 2599–2604.

(10) Deshpande, A. S.; Pinna, N.; Smarsly, B.; Antonietti, M.; Niederberger, M. Controlled assembly of preformed ceria nanocrystals into highly ordered 3D nanostructures. *Small* **2005**, *1*, 313–316.

(11) Si, R.; Zhang, Y.-W.; Wang, L.-M.; Li, S.-J.; Lin, B.-X.; Chu, W.-S.; Wu, Z.-Y.; Yan, C.-H. Enhanced Thermal Stability and Oxygen Storage Capacity for $Ce_xZr_{1-x}O_2$ ($x = 0.4–0.6$) Solid Solutions by Hydrothermally Homogenous Doping of Trivalent Rare Earths. *J. Phys. Chem. C* **2007**, *111*, 787–794.

(12) Ohtake, N.; Katoh, M.; Sugiyama, S. High thermal-stability ceria synthesized via thermal-hydrolysis route and methane-combustion performance. *J. Ceram. Soc. Japan* **2017**, *125*, 57–61.

(13) Si, R.; Zhang, Y.-W.; Li, S.-J.; Lin, B.-X.; Yan, C.-H. Urea-Based Hydrothermally Derived Homogeneous Nanostructured $Ce_{1-x}Zr_xO_2$ ($x = 0–0.8$) Solid Solutions: A Strong Correlation between Oxygen Storage Capacity and Lattice Strain. *J. Phys. Chem. B* **2004**, *108*, 12481–12488.

(14) Esteves, P.; Wu, Y.; Dujardin, C.; Dongare, M. K.; Granger, P. Ceria–zirconia mixed oxides as thermal resistant catalysts for the decomposition of nitrous oxide at high temperature. *Catal. Today* **2011**, *176*, 453–457.

(15) Aneggi, E.; Leitenburg, C. de; Dolcetti, G.; Trovarelli, A. Promotional effect of rare earths and transition metals in the combustion of diesel soot over CeO_2 and CeO_2–ZrO_2. *Catal. Today* **2006**, *114*, 40–47.

(16) Li, M.; Liu, Z.; Hu, Y.; Wang, M.; Li, H. Effect of doping elements on catalytic performance of CeO_2-ZrO_2 solid solutions. *Journal of Rare Earths* **2008**, *26*, 357–361.

(17) Özkan, E.; Hofmann, A.; Votsmeier, M.; Wang, W.; Huang, X.; Kübel, C.; Badaczewski, F.; Turke, K.; Werner, S.; Smarsly, B. M. Comprehensive Characterization of a Mesoporous Cerium Oxide Nanomaterial with High Surface Area and High Thermal Stability. *Langmuir* **2021**, *37*, 2563–2574.

(18) Cop, P.; Celik, E.; Hess, K.; Moryson, Y.; Klement, P.; Elm, M. T.; Smarsly, B. M. Atomic Layer Deposition of Nanometer-Sized CeO_2 Layers in Ordered Mesoporous ZrO_2 Films and Their Impact on the Ionic/Electronic Conductivity. *ACS Appl. Nano Mater.* **2020**, *3*, 10757–10766.

(19) Skála, T.; Šutara, F.; Prince, K. C.; Matolín, V. Cerium oxide stoichiometry alteration via Sn deposition: Influence of temperature. *J. Electron Spectrosc. Relat. Phenom.* **2009**, *169*, 20–25.

(20) Bêche, E.; Charvin, P.; Perarnau, D.; Abanades, S.; Flamant, G. Ce 3d XPS investigation of cerium oxides and mixed cerium oxide ($Ce_xTi_yO_z$). *Surf. Interface Anal.* **2008**, *40*, 264–267.

(21) Thommes, M.; Kaneko, K.; Neimark, A. V.; Olivier, J. P.; Rodriguez-Reinoso, F.; Rouquerol, J.; Sing, K. S. Physisorption of gases, with special reference to the evaluation of surface area and pore size distribution (IUPAC Technical Report). *Pure Appl. Chem.* **2015**, *87*, 1051–1069.

(22) Cimino, R.; Cychosz, K. A.; Thommes, M.; Neimark, A. V. Experimental and theoretical studies of scanning adsorption–desorption isotherms. *Colloids Surf., A* **2013**, *437*, 76–89.

(23) Kube, S. A.; Turke, K.; Ellinghaus, R.; Wallacher, D.; Thommes, M.; Smarsly, B. M. Pore Size Gradient Effect in Monolithic Silica Mesopore Networks Revealed by In-Situ SAXS Physisorption. *Langmuir* **2020**, *36*, 11996–12009.

(24) Cychosz, K. A.; Guillet-Nicolas, R.; García-Martínez, J.; Thommes, M. Recent advances in the textural characterization of hierarchically structured nanoporous materials. *Chem. Soc. Rev.* **2017**, *46*, 389–414.

(25) Zhang, F.; Chen, C.-H.; Hanson, J. C.; Robinson, R. D.; Herman, I. P.; Chan, S.-W. Phases in Ceria-Zirconia Binary Oxide ($1-x$)CeO_2-$xZrO_2$ Nanoparticles: The Effect of Particle Size. *J. Am. Ceram. Soc.* **2006**, *89*, 1028–1036.

(26) Mestl, G.; Rosynek, M. P.; Lunsford, J. H. Decomposition of Nitric Oxide over Barium Oxide Supported on Magnesium Oxide. 2. In Situ Raman Characterization of Phases Present during the Catalytic Reaction. *J. Phys. Chem. B* **1997**, *101*, 9321–9328.

https://doi.org/10.1021/acs.langmuir.2c00875
Langmuir 2022, 38, 8342–8352

(27) Filtschew, A.; Stranz, D.; Hess, C. Mechanism of NO2 storage in ceria studied using combined in situ Raman/FT-IR spectroscopy. *Physical chemistry chemical physics PCCP* **2013**, *15*, 9066−9069.
(28) Sun, Y.; Li, C.; Djerdj, I.; Khalid, O.; Cop, P.; Sann, J.; Weber, T.; Werner, S.; Turke, K.; Guo, Y.; Smarsly, B. M.; Over, H. Oxygen storage capacity versus catalytic activity of ceria−zirconia solid solutions in CO and HCl oxidation. *Catal. Sci. Technol.* **2019**, *9*, 2163−2172.
(29) Schilling, C.; Hofmann, A.; Hess, C.; Ganduglia-Pirovano, M. V. Raman Spectra of Polycrystalline CeO_2: A Density Functional Theory Study. *J. Phys. Chem. C* **2017**, *121*, 20834−20849.
(30) Ikryannikova, L.; Aksenov, A.; Markaryan, G.; Murav'eva, G.; Kostyuk, B.; Kharlanov, A.; Lunina, E. The red−ox treatments influence on the structure and properties of M_2O_3−CeO_2−ZrO_2 (M = Y, La) solid solutions. *Applied Catalysis A: General* **2001**, *210*, 225−235.
(31) Özkan, E.; Cop, P.; Benfer, F.; Hofmann, A.; Votsmeier, M.; Guerra, J. M.; Giar, M.; Heiliger, C.; Over, H.; Smarsly, B. M. Rational Synthesis Concept for Cerium Oxide Nanoparticles: On the Impact of Particle Size on the Oxygen Storage Capacity. *J. Phys. Chem. C* **2020**, *124*, 8736−8748.

https://doi.org/10.1021/acs.langmuir.2c00875
Langmuir 2022, 38, 8342−8352

3.2 Effects of Hydrothermal Treatment on Mesopore Structure and Connectivity in Doped Ceria-Zirconia Mixed Oxides

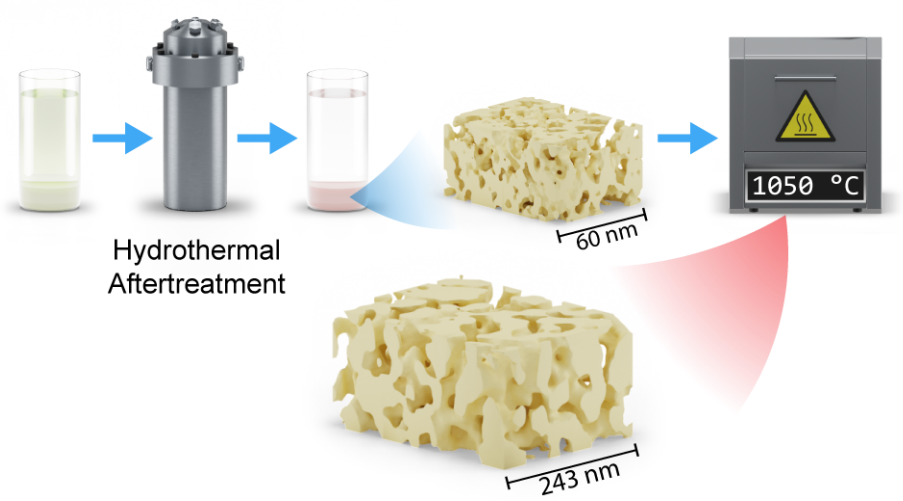

Prates da Costa, E., Huang, X., Kübel, C., Cheng, X., Schladitz, K., Hofmann, A., Göbel, U., Smarsly, B. M. Effects of Hydrothermal Treatment on Mesopore Structure and Connectivity in Doped Ceria-Zirconia Mixed Oxides, *Langmuir* **2022**, 39, 177–191.

DOI: 10.1021/acs.langmuir.2c02366

LANGMUIR

pubs.acs.org/Langmuir Article

Effects of Hydrothermal Treatment on Mesopore Structure and Connectivity in Doped Ceria-Zirconia Mixed Oxides

Eric Prates da Costa, Xiaohui Huang, Christian Kübel, Xiaoyin Cheng, Katja Schladitz, Alexander Hofmann, Ulrich Göbel, and Bernd M. Smarsly*

Cite This: *Langmuir* 2023, 39, 177−191 Read Online

ACCESS | Metrics & More | Article Recommendations | Supporting Information

ABSTRACT: Pore size and pore connectivity control diffusion-based transport in mesopores, a crucial property governing the performance of heterogeneous catalysts. In many cases, transition-metal oxide catalyst materials are prepared from molecular precursors involving hydrothermal treatment followed by heat treatment. Here, we investigate the effects of such a hydrothermal aftertreatment step, using an aqueous ammonia solution, on the disordered mesopore network of $Ce_xZr_{1-x-y-z}Y_yLa_zO_{2-\delta}$ mixed oxides. This procedure is a common synthesis step in the preparation of such ceria-based oxygen storage materials applied in three-way catalysis, employed to improve the materials' thermal stability. We perform state-of-the-art Ar-physisorption analysis, especially advanced hysteresis scanning, to paint a detailed picture of the alterations in mesopore space caused by the hydrothermal aftertreatment and subsequent aging at 1050 °C. Furthermore, we investigate the network characteristics by electron tomography in combination with suitable statistical analysis, enabling a consistent interpretation of the desorption scans (physisorption). The results indicate that the hydrothermal aftertreatment enhances the mesopore connectivity of the continuous 3D network by widening pores and especially necks, hence facilitating accessibility to the particles' internal surface area and the ability to better withstand high temperatures.

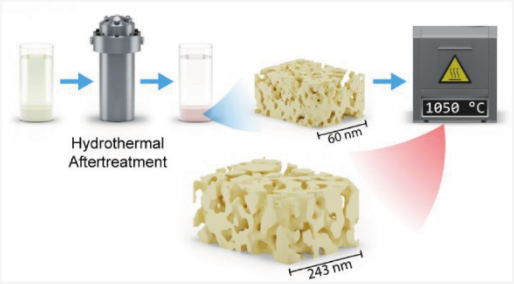

INTRODUCTION

Ceria and ceria-based mixed oxides are applied in a variety of catalytic processes,[1] e.g., the water−gas shift reaction, HCl oxidation,[2,3] and thermochemical water splitting.[4−6] The predominant application, however, still is the control of automotive emissions in three-way catalysis (TWC), where it is employed as an active support material for the catalytically active platinum group metals (PGMs; Pt, Pd, and Rh). These materials are also called oxygen storage materials (OSMs), and their role is to act as a buffer to accommodate changes in the exhaust gas composition by providing oxygen from the lattice for rich air to fuel ratios or incorporating oxygen for lean air to fuel ratios, thereby ensuring optimal conversion of toxic emissions.[7,8] Therefore, their capability of easily and reversibly switching the Ce oxidation state between +IV and +III is crucial, as it facilitates the formation of oxygen vacancies upon oxygen release. However, in spite of excellent redox properties, pure, mesoporous ceria has low thermal stability; i.e., when subjected to high temperatures, it suffers from the severe collapse of pores and the concomitant loss of specific surface area and pore volume, partially because of crystallite growth and sintering. These alterations are detrimental to optimal performance in heterogeneous catalysis, as they result in a decrease in PGM dispersion or could even cause the entrapment of PGMs in inaccessible voids. The formation of a solid solution with zirconia has been proven to be an effective method to mitigate the effects of such low thermal stability, especially in combination with trivalent doping, e.g., Y and/or La, which prevents phase segregation of the ceria-zirconia mixed oxide at high temperatures. Following this design strategy, here we study a specific type of ceria-zirconia mixed oxides, $Ce_xZr_{1-x-y-z}Y_yLa_zO_{2-\delta}$, which has been reported to feature high oxygen storage as well as promising thermal stability. However, besides a high and thermally stable specific surface area, the accessibility of this surface area and hence the catalytically active PGM particles are of utter importance to the effectivity of the catalyst. As demonstrated in the field of zeolite-based heterogeneous catalysis by the groups of Pérez-Ramírez[9,10] and Mitchell[11] et al., the performance of heterogeneous catalysts can be directly related to the connectivity of the pore space on the nanometer scale, which

Received: August 30, 2022
Revised: November 9, 2022
Published: December 23, 2022

https://doi.org/10.1021/acs.langmuir.2c02366
Langmuir 2023, 39, 177−191

Scheme 1. (a) Steps in the Synthesis Procedure Underlying This Study and (b) Data Acquisition and Analysis Pathway

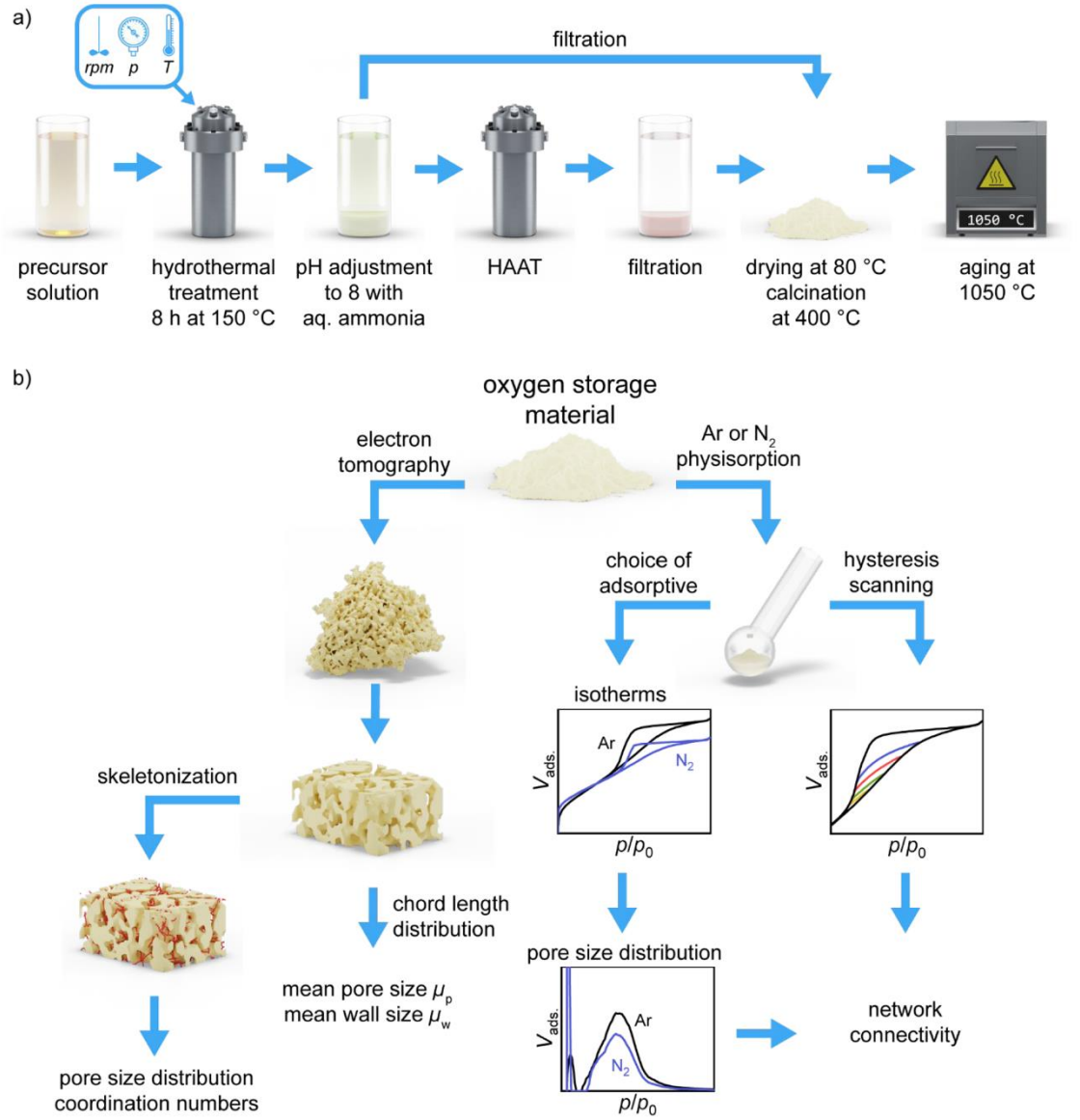

governs the transport processes to the active sites. The optimum performance of heterogeneous catalysts can be achieved in hierarchically structured pore systems possessing a multimodal pore size distribution, with each pore population being responsible for a different transport mechanism.[12] In such hierarchical pore structures, the macropores (d_{pore} > 50 nm) enable advective mass transport caused by a pressure difference between the inlet and the outlet of the catalyst and molecular diffusion. The predominant mechanism in mesopores (2 < d_{pore} < 50 nm), however, is Knudsen diffusion, with a diffusivity of up to 1 order of magnitude lower compared to molecular diffusion and which heavily depends on the mesopore diameter. In order to address these requirements during material synthesis, a deep understanding of the resulting material's mesopore space and connectivity and their dependency on the underlying synthesis procedure is crucial. Hence, in search of highly stable and high-performance support materials in TWC, a variety of approaches have been developed that provide fine control over structural parameters.[1] Many of them are based on coprecipitation or hydrothermal synthesis,[13,14] often combined with a sequence of aftertreatment steps performed on the precipitates, to tailor particle and pore sizes. In this study, we focus on the effects of a commonly performed hydrothermal ammonia aftertreatment[15−17] (HAAT) on the pore space's morphology and thermal stability, applying state-of-the-art analytical methodology. Such a hydrothermal aftertreatment was found to increase

https://doi.org/10.1021/acs.langmuir.2c02366
Langmuir 2023, 39, 177−191

the specific surface area and pore volume of the treated material in comparison to those of an untreated material while also increasing its thermal stability. In general, chemical aftertreatment procedures can alter the surface functionalization (e.g., removal of nitrate groups) or mechanically strengthen the mesoporous skeleton in a dissolution and reprecipitation process, possibly rendering the obtained materials more stable against sintering. In contrast to that, high-temperature thermal treatment is a rather harsh process for the removal of undesired functional groups. During combustion, these might create dangling bonds, facilitating the sintering processes, which commonly results in the severe loss of porosity.

The examined synthesis of $Ce_xZr_{1-x-y-z}Y_yLa_zO_{2-\delta}$ was adapted from Ohtake et al.[18] and modified with respect to the chemical composition of the material (cf. Scheme 1a) to resemble a commercially tried and tested composition that meets the design requirements of highly performing OSMs. However, the relationship between typical synthesis steps and the final mesopore space of the material, especially after aging at high temperatures, is still a matter of research. To unravel these relations, methods are required that not only allow the determination of integral parameters such as specific surface areas, e.g., BET method, and pore volumes but also provide insight into the local connectivity of pores. A very powerful method that is often employed to analyze the 3D nature of pore systems is electron tomography,[19−21] on the basis of which a 3D reconstruction of the analyzed material at the nanoscale can be generated, providing extensive data on pore dimensions, the spatial arrangement of pores, and pore connectivity as well as complementary information on the solid material phase. The downside of electron tomography, however, is the accessibility to such instruments as well as the laborious reconstruction and evaluation process that further requires substantial computational resources and trained personnel. Inherently, electron tomography can give insight into only a very small part of the material. A promising complement to electron tomography is the physisorption analysis of the mesoporous materials by so-called hysteresis scanning, a special physisorption technique. The method allows the discrimination of different types of mesopore networks based on the shape of the recorded desorption isotherms, which are measured in subsequent cycles, each starting at a different filling state of the pore system.[22,23] However, the interpretation of these scanning isotherms is still not straightforward, especially for disordered mesopore networks. Thus, establishing hysteresis scanning as a routine method depends on a profound understanding of the relation between the shape of desorption isotherms and the 3D mesopore space to which they correspond.[24] Also, such analysis requires significantly fewer resources than electron tomography and can also be performed on a much shorter time scale. In this work, we aim to contribute to the fundamental interpretation of desorption isotherms by combining argon hysteresis scanning with data obtained by electron tomography. Scheme 1b shows a schematic representation of the approach described in this study, highlighting the obtained information from each method and how it is used to draw conclusions about the material.

Many real-world examples for widely applied heterogeneous catalysts, such as complex metal oxide materials applied in TWC, feature such disordered pore networks. Therefore, we put it to the test by elucidating the effects of a hydrothermal ammonia aftertreatment on the nature of the pore space in a complex quaternary mixed oxide. Thus, a major goal of the presented study is to assess if hysteresis scanning can indeed be a tool for the routine analysis of such disordered pore networks.

MATERIALS AND METHODS

Preparation of $Ce_{0.18}Zr_{0.64}Y_{0.15}La_{0.03}O_{2-\delta}$ Powders. Based on the synthesis by Ohtake et al.,[18] the $Ce_{0.18}Zr_{0.64}Y_{0.15}La_{0.03}O_{2-\delta}$ powders were prepared by hydrothermal synthesis with and without an additional hydrothermal aftertreatment step using an aqueous ammonia solution (hereinafter abbreviated as HAAT). A 0.464 mol L^{-1} aqueous solution of $(NH_4)_2[Ce(NO_3)_6]$ (99.1%, Treibacher Industrie AG), $ZrO(NO_3)_2$ (20 wt % aq solution, >98%, Luxfer MEL Technologies), $Y(NO_3)_3{\cdot}6H_2O$ (>99%, Treibacher Industrie AG), and $La(NO_3)_3{\cdot}6H_2O$ (≥99.99%, Carl Roth GmbH + Co. KG) with a molar ratio of $Ce^{4+}/ZrO^{2+}/Y^{3+}/La^{3+}$ = 0.18:0.64:0.15:0.03 was placed in an autoclave, which was then filled with compressed air to a pressure of 2 bar. The solution was subsequently heated to 150 °C for 8 h under continuous stirring. After the hydrothermal treatment, the solution's pH was set to 8 by the addition of an aqueous ammonia solution (25 wt %). The obtained whitish-brown precipitate was filtered and subsequently dried at 80 °C for 18 h. The powder was finally calcined at 400 °C for 10 h to yield a pale-yellow powder (400noHAAT). In the variation with the additional HAAT step, after pH adjustment (pH 8) and filtration, the wet filter cake (ca. 240 g, pale brown) was redispersed in 1120 g of aqueous ammonia solution (5 wt %) and placed in the autoclave. The aftertreatment was performed under continuous stirring at an initial pressure of 2 bar (compressed air) and a temperature of 80 °C for 11 h. After this procedure, the pale-yellow precipitate was again separated by filtration and subsequently dried at 80 °C for 18 h. The powder was then calcined at 400 °C for 10 h to produce a pale-yellow powder (400HAAT). Both powders were also tested for thermal stability by aging at 1050 °C for 4 h in ambient air (1050noHAAT/1050HAAT).

Characterization. *Physisorption.* Argon physisorption was measured on an Autosorb iQ2 automated gas sorption analyzer (Quantachrome Instruments) at 87 K. Nitrogen physisorption was measured at 77 K. Prior to measurement, all samples were degassed under vacuum at 120 °C for 18 h. Data evaluation was performed with *ASiQwin* version 4.0 (Quantachrome Corporation). The Brunauer−Emmett−Teller (BET) method was used over a pressure range of p/p_0 = 0.05−0.30 to calculate the specific surface area. Pore size distributions (PSDs), assuming a cylindrical pore geometry, were calculated with a nonlocalized density functional theory (NLDFT) kernel of argon at 87 K on zeolites/silica. A comparison of the fit qualities is depicted in Figure S3.

XRD. Powder diffractograms were recorded on an Empyrean diffractometer (PANalytical) with Cu Kα radiation. The instrument was operated at a voltage of 40 kV and an output current of 40 mA. Crystallite sizes were calculated with the Scherrer equation after fitting the reflections with *HighScore Plus* version 3.0.5 (PANalytical).

SEM. Scanning electron microscopy was performed on a Smart SEM MERLIN scanning electron microscope (Carl Zeiss) after sputtering the samples with platinum for 60 s. The acceleration voltage was set to 3 kV, and the sample current, to 78 pA.

STEM Tomography. Scanning transmission electron microscopy (STEM)-based tomography was performed on a Themis 300 transmission electron microscope (Thermofisher Scientific) equipped with a probe aberration corrector, operated at 300 kV. The samples were prepared by grinding ca. 10 mg of the powders, suspending in ethanol, and dropping the suspension on a 100 × 400 mesh carbon-coated Cu grid (Quantifoil Micro Tools GmbH). Finally, Au nanoparticles ($d_{Au\text{-}np}$(400 °C) = 6 nm, $d_{Au\text{-}np}$(1050 °C) = 12 nm) were deposited onto the sample as fiducial markers, and the samples were cleaned two times for 30 s using a Fischione 1070 plasma cleaner in Ar/O_2 with a power of 50%. The tilt series were collected with a high-angle annular dark-field (HAADF) detector over the tilt ranges shown in Table S1 with a step size of 2°. Image alignment was performed in *IMOD* version 4.11.7 (University of Colorado) based on the Au fiducial markers. The residual alignment errors are also listed in Table S1. The 3D reconstructions of the aligned tilt series were performed in

https://doi.org/10.1021/acs.langmuir.2c02366
Langmuir 2023, 39, 177−191

Inspect3D version 4.4 (Thermofisher Scientific) using the simultaneous iterative reconstruction technique (SIRT) with 100 iterations. The resulting tomograms were then denoised using a median filter in *ImageJ*, following binarization by global thresholding in *Avizo* version 2021.1 (Thermofisher Scientific) to obtain an initial segmentation. Before further quantitative analysis, the segmentation was refined by removing unconnected and small islands with a diameter smaller than 3 voxels, which are caused by reconstruction artifacts.

Morphological Analysis. The resulting image stacks were analyzed by a set of methods regarding different morphological aspects. Skeletonization was performed on cropped regions of the particles in *Avizo* software using the Auto Skeleton module for the pore size characterization and according to the method described by Cheng et al.[25], implemented in ToolIP (Fraunhofer ITWM), to determine the local pore connectivity. The local thickness was calculated with the Local Thickness plugin in *Fiji*. To save resources during local thickness calculations on full particles, the particle was additionally separated from the background by determining the boundary around the particle for each slice with the find_outer_region method of the *python* toolkit PoreSpy.[26] The underlying *python* script can be found in the Supporting Information. For the 400 and 1050 °C powders, different rolling ball radii of 20 and 50 pixels were used, respectively. The corresponding values result from the difference in pixel and pore sizes in the reconstructions. The pore and wall spaces within the segmented volume were also analyzed using chord length distribution (CLD) analysis as described by Bruns et al.[27] In this method, points in the void or solid phase are chosen at random and a set of 26 angularly evenly spaced vectors are projected into the corresponding phase. The combined length of two opposing vectors represents the length of one chord. By this procedure, a total number of 10^6 chords was collected, omitting chords touching the boundary of the image stack. The obtained chord length distribution was binned, and a k-gamma function was fitted to the resulting histogram, providing the mean chord length μ.

■ RESULTS AND DISCUSSION

The composition of the investigated materials was verified by ICP-OES to be $Ce_{0.20}Zr_{0.63}Y_{0.14}La_{0.03}O_{2-\delta}$ for the sample without HAAT and $Ce_{0.19}Zr_{0.63}Y_{0.15}La_{0.03}O_{2-\delta}$ for the sample subjected to the aftertreatment step in an NH_3(aq) solution (5 wt %; HAAT). As reported previously,[28] the material features a special microstructure of agglomerated 5 μm spheres. This microstructure is stable during the performed ripening procedure and at high temperatures, as the SEM images indicate (Figure S1). XRD patterns (Figure 1) reveal the formation of a solid solution possessing a cubic phase during synthesis. Calculation of the crystallite size by the Scherrer method results in a very small dimension of 3 nm after calcination for both synthesis procedures. Upon aging at 1050 °C, the crystallite size of the calcined samples increases to 20 nm (1050noHAAT) and 19 nm (1050HAAT), suggesting that the crystallite size is unaffected by the HAAT step.

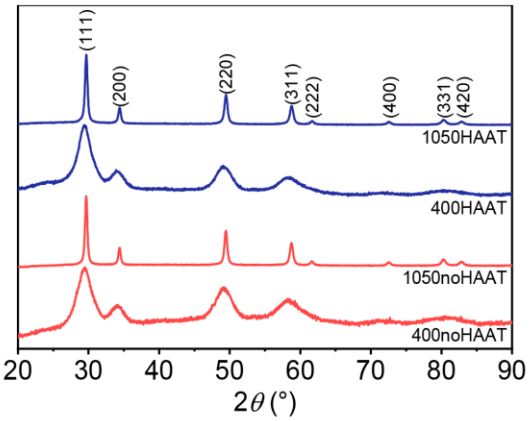

Figure 1. Comparison of XRD patterns before and after aging at 1050 °C.

To examine the morphology of the mesopore space and the alterations caused by HAAT by gas adsorption, a set of argon and nitrogen isotherms was recorded for each sample. Physisorption using argon at 87 K is the preferable method for textural characterization due to the absence of specific interactions with surface functional groups and accelerated diffusion in comparison to nitrogen at 77 K.[29] Hence, the following part will focus on the parameters derived from the argon physisorption measurements instead of a direct comparison of the sorption experiments. However, valuable information on the connectivity of mesopores can be obtained from the comparison with nitrogen physisorption (performed at 77 K), as discussed later in the article. Figure 2a shows the Ar isotherms measured at 87 K for the samples before and after aging at 1050 °C. According to the IUPAC classification,[29] sample 400noHAAT features a type IV isotherm with type H2 hysteresis loop, commonly found in materials, exhibiting strong network effects. Furthermore, the material possesses a high BET area of 150 $m^2\ g^{-1}$, a pore volume of 0.14 $cm^3\ g^{-1}$, and a narrow PSD ranging from 1 to 10 nm with a mean pore diameter of 4.3 nm (Figure 2c). After aging at 1050 °C, the hysteresis loop resembles an H1-type hysteresis. During this transformation, the BET area and pore volume are reduced drastically to 13 $m^2\ g^{-1}$ and 0.07 $cm^3\ g^{-1}$, respectively.

The material subjected to HAAT before drying and calcination also features a type IV isotherm with a type H2 hysteresis loop. In comparison to the sample without HAAT, additional aftertreatment in an aqueous NH_3 solution results in an increase in mesopore volume by a factor of 1.5 (0.21 $cm^3\ g^{-1}$) while maintaining a BET area of 145 $m^2\ g^{-1}$. Although the mean pore diameter of 5.3 nm is only 1 nm larger than in the material without HAAT, the PSD (Figure 2c) shows a pronounced tailing effect of the pore population toward larger mesopore diameters ranging from 3 up to 18 nm. Hints at a small secondary population of even larger pores can be seen in the range from 18 to 27 nm. As the direct comparison of PSDs implies, HAAT thus severely alters the mesopore space by enlarging the pores and increasing the mesopore volume.

After aging, the HAAT material (1050HAAT) also features an H1-type hysteresis loop and has a quite high overall mesopore volume of 0.13 $cm^3\ g^{-1}$, considering the quite high temperature applied (1050 °C). As the comparison of cumulative pore volumes (Figure 2d) shows, the larger pore volume observed after aging is mostly caused by an increased fraction of pores larger than 19 nm. This improvement of thermal stability is also visible in the BET area of 20 $m^2\ g^{-1}$ after aging, an increase by a factor of about 1.5. To ensure the reproducibility of these values, the physisorption analysis was repeated three times on the same material, providing values within the experimental uncertainty (5%). The porosity parameters of the materials in their different stages are summarized in Figure 2b.

To elucidate the pore connectivity and possible effects of the aftertreatment step, desorption scanning was performed using argon (T = 87 K). In this type of physisorption analysis, a set of desorption isotherms are recorded based on different filling states of the pore system, which is achieved by conducting

https://doi.org/10.1021/acs.langmuir.2c02366
Langmuir 2023, 39, 177−191

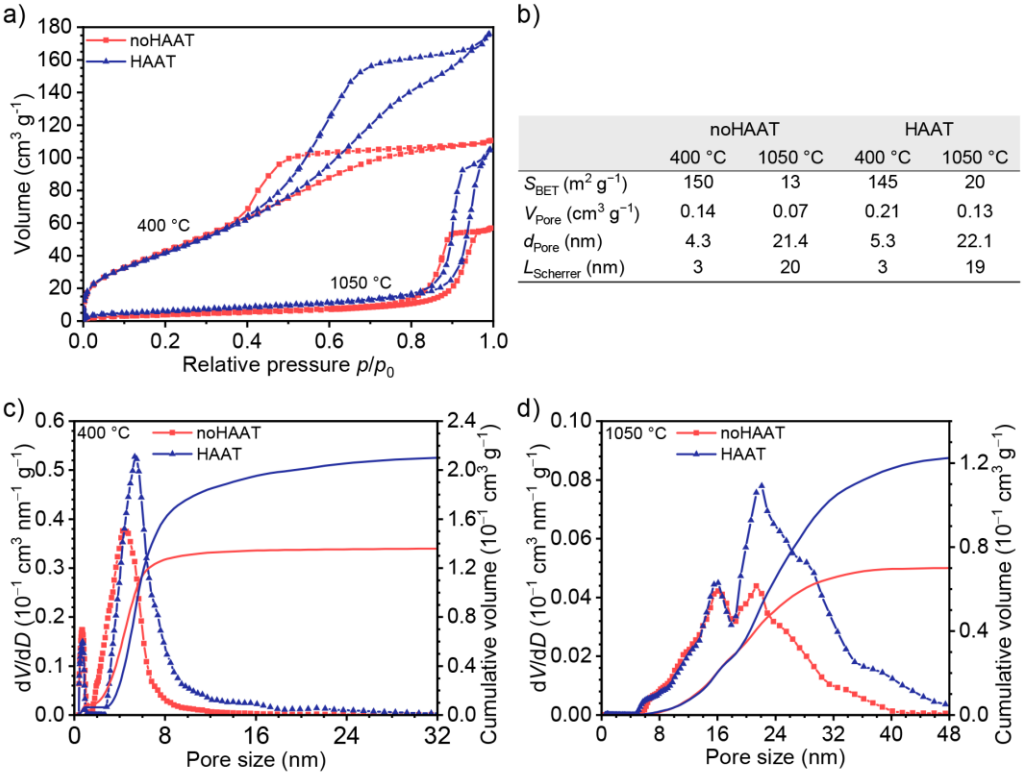

b)

	noHAAT		HAAT	
	400 °C	1050 °C	400 °C	1050 °C
S_{BET} (m^2 g^{-1})	150	13	145	20
V_{Pore} (cm^3 g^{-1})	0.14	0.07	0.21	0.13
d_{Pore} (nm)	4.3	21.4	5.3	22.1
$L_{Scherrer}$ (nm)	3	20	3	19

Figure 2. (a) Ar-physisorption isotherms (T = 87 K) of the samples after calcination (400 °C) and aging (1050 °C). (b) Tabular summary of mesopore space characteristics. (c and d) Comparison of NLDFT-based differential PSDs of the calcined (400 °C) and aged (1050 °C) powders and cumulative pore volumes (right y axis, line without symbols).

multiple sorption cycles, each starting at a lower relative pressure (p/p_0) than the previous cycle (Figure 3). By this procedure, the desorption behavior of the subsequently less-filled pore system is monitored. The shape of the resulting scanning isotherms is characteristic of the underlying desorption mechanisms and allows discriminating different types of pore connectivity.[24]Fig-Figure 3 shows the hysteresis loops of all four samples together with the obtained scanning segments and reveals significant differences between the samples and the underlying mesopore networks. Also, the shape of the scanning segments is probably caused by a superposition of desorption mechanisms unfolding simultaneously, hinting at a possibly inhomogeneous nature of the mesopore networks.

Sample 400noHAAT (Figure 3b) exhibits scanning segments that directly cross the hysteresis loop and meet the boundary isotherm in a sharp bend, after which they follow the boundary isotherm. This behavior is observed when evaporation during desorption is hindered by small pore necks, causing pore-blocking or cavitation. To distinguish between pore-blocking and cavitation, the desorption-based PSDs obtained from isotherms measured with different adsorptives (e.g., Ar and N_2) can be compared.[30] In the case of cavitation, gas bubbles form inside the mesopores if the difference in neck and cavity sizes of pores is very large. Then the PSDs obtained from the desorption branches of Ar and N_2 physisorption appear to be shifted with respect to each other (cf. Figure 4a) as the formation of these gas bubbles depends on the liquid–vapor transition of the adsorbate, which is a property of the employed adsorptive. If the difference in neck and cavity sizes is smaller, evaporation from the pore begins when evaporation from the neck starts. In this case, the PSDs, determined from the desorption branches from different adsorptives, correspond to the neck sizes and are identical in regard to the position of the corresponding pore size. Here, a small difference in the position of the maxima of the PSDs of 0.3 nm can be observed (Figure 4a), which, as described above, is formally an indication of cavitation. However, we consider the difference to be too small to distinguish the mechanisms for this sample. During desorption, the segments furthermore exhibit a shallow slope, indicating the simultaneous presence of network percolation effects.

In strong contrast to that, sample 400HAAT (Figure 3c) features desorption isotherms with steeper slopes that asymptotically merge into the boundary isotherm. Such behavior hints at either pore blocking or network percolation as types of mesopore connectivity. Interestingly, the p/p_0 value at which the desorption isotherms merge into the boundary isotherm is subsequently lowered with each sorption cycle starting from a lower p/p_0. One explanation for this behavior, which has also been observed in monolithic meso-macroporous silica, could be spatial pore size gradients or inhomogeneities,[24] possibly introduced during the hydrothermal treatment under basic conditions. Unfortunately, although plausible, the existence of such gradients cannot be confirmed by electron

https://doi.org/10.1021/acs.langmuir.2c02366
Langmuir 2023, 39, 177−191

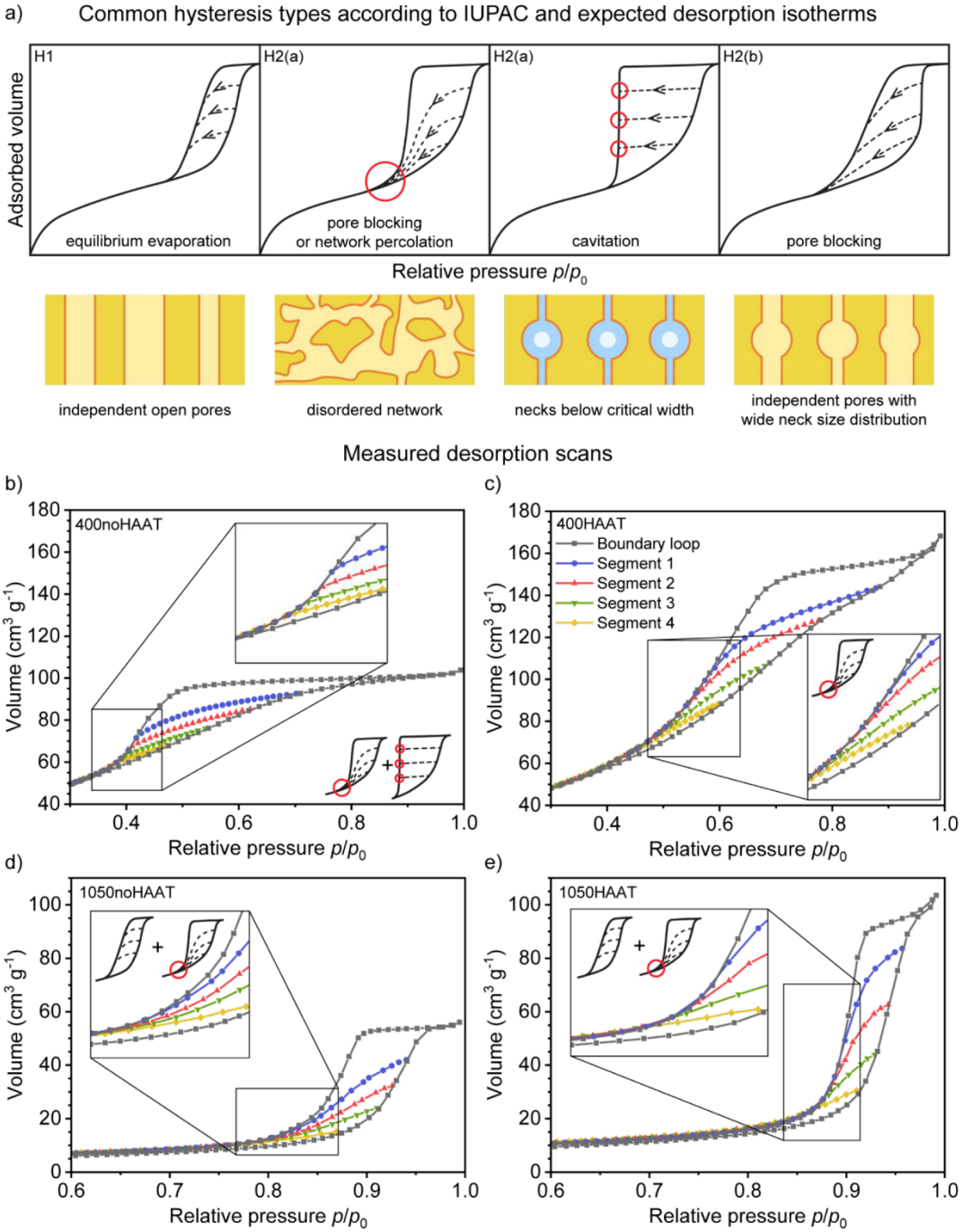

Figure 3. (a) Illustration of common hysteresis types and corresponding desorption scanning isotherms found in mesoporous materials. Reproduced from Kube & Turke et al.[24] Copyright 2020 American Chemical Society. (b–e) Comparison of hysteresis loops of all four samples, each scanned with four desorption isotherms (using Ar, T = 87 K). Here, the adsorption branches of the individual scanning isotherms are omitted for visual clearance; i.e., only the overall boundary adsorption branch is shown. The full scanning isotherms including the adsorption branches for each cycle are shown in Figure S4.

https://doi.org/10.1021/acs.langmuir.2c02366
Langmuir 2023, 39, 177–191

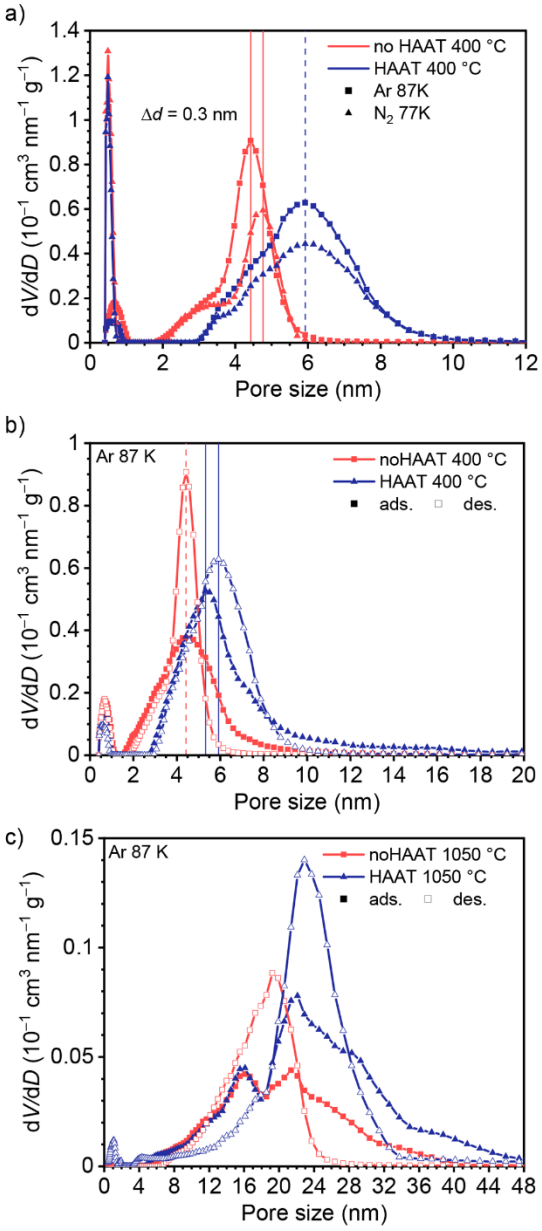

Figure 4. (a) Comparison of NLDFT-based PSDs calculated from the desorption branch of the Ar and N_2 isotherms of the samples after calcination (400 °C) and NLDFT-based PSDs from the adsorption and desorption branches of (b) the calcined samples' isotherms (400 °C) and (c) the aged samples' isotherms (1050 °C).

tomography (see below) as it provides only a small and local section of the material. Suitable experiments to prove such gradients have been presented by Kube and Turke et al.[24] Furthermore, this feature in the desorption scanning isotherms indicates the strong influence of the pore network on the evaporation from the pores in the material for 400HAAT. Since the interpretation of the desorption scans is challenging, a comparison of the PSDs determined from the full adsorption and desorption isotherms provides complementary insights (Figure 4b). This comparison reveals a shift of the mode value of the desorption-based PSD to larger values compared to the adsorption-based PSD, which appears to be counterintuitive at first and is quite different from that of sample 400noHAAT. This surprising shift can be attributed to the so-called "initiated condensation" mechanism already observed for mesopore networks.[24,31] In essence, 400HAAT thus features an indication for a 3D network-like, unhindered connection among the mesopores, while 400noHAAT features severely restricted mesopore connections. In conclusion, desorption scanning and the desorption-based PSDs suggest that by the aftertreatment procedure the accessibility of mesopores is significantly changed toward a more accessible mesopore network, especially preventing the occurrence of cavitation.

After aging at 1050 °C, the desorption isotherms of the noHAAT sample (Figure 3d) converge in the lower closure point of the hysteresis loop. This peculiarity indicates a strong influence of network percolation on the desorption in the absence of pore size gradients. Similarly, the desorption isotherms of sample 1050HAAT (Figure 3e) also indicate strong network percolation. Similar to sample 400HAAT (before aging), the scanning isotherms do not meet in the lower closure point of the boundary isotherm but at higher p/p_0. The p/p_0 value of this merging point is also subsequently lowered, suggesting that possibly pore size gradients remain after aging. Interestingly, the boundary isotherms of the aged samples feature a sharp bend in the desorption branch that is not present in the scanning curves. This feature implies that the larger mesopores appear to be severely hindered during pore emptying because of narrow necks connecting them to the outside. The comparison of adsorption- and desorption-derived PSDs (Figure 4c) supports this interpretation, as pores with large diameters (>24 nm for noHAAT, >30 nm for HAAT) make a smaller contribution to the desorption-based PSDs than to the adsorption-based PSDs.

To obtain detailed statistical information on pore connectivity and complementary information on the structural nature of the solid phase, electron tomographic analysis was performed. This method yields a 3D representation of the investigated materials at the nanoscale by reconstructing a binary image stack from a series of STEM images comprising different projection angles of the investigated particles.[32,33] Such 3D reconstruction holds information about pore and wall sizes as well as the hierarchical structure and connectivity of the pore network and has been used successfully to unravel the connectivity in macro- and mesoporous silica monoliths[20,21] and particles[34−36] as well as ceria materials.[19] The 3D sections shown in Figure 5 illustrate the alterations to the morphology upon aging at 1050 °C and the influence of the hydrothermal NH_3(aq) aftertreatment on the material's stability. Both samples calcined at 400 °C feature a similar finely structured and disordered mesopore network. Aging at 1050 °C causes a severe coarsening of the morphology and leads to a drastic densification of the material in the sample without aftertreatment, while the general morphology appears to be retained in the sample exposed to aftertreatment. Notably, the bare images reveal significant differences between 1050HAAT and 1050noHAAT, with the former possessing a larger porosity, in agreement with the physisorption analysis.

Figure 6 shows a comparison of 2D slices through the reconstructions of the four analyzed particles. Pore voxels are

https://doi.org/10.1021/acs.langmuir.2c02366
Langmuir 2023, 39, 177−191

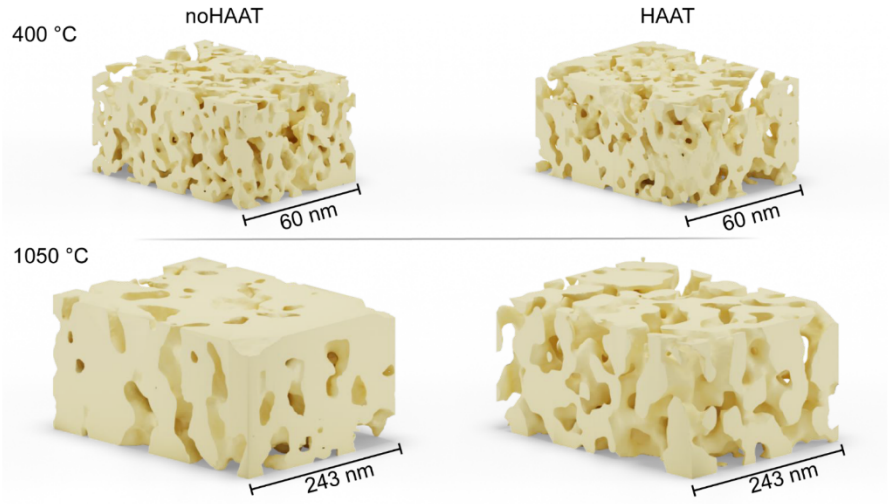

Figure 5. Sections of the 3D-reconstructed powders after calcination at 400 °C (top) and subsequent aging at 1050 °C (bottom).

color coded according to the local pore thickness, which is defined as the largest sphere that fits into the pore and is encompassing the given voxel. This method provides an insightful visualization of mesopore dimensions and their spatial distribution and connectivity (Figure 6a).

By calculating a histogram for the full image stack, a visual assessment of the slice images can also be translated into a pore size distribution. The corresponding histograms are shown in Figure 7 together with the pore size distributions obtained from Ar physisorption, which are in excellent agreement with the local thickness analysis. The biggest difference is caused by the capability of Ar physisorption to detect micropores, which are not resolved by STEM tomography but are visible as a pore population in the range of 0−1.5 nm (Ar physisorption). The same analysis was performed for the solid phase (Figures S5 and S6), where prior to aging (calcined at 400 °C) both the noHAAT and the HAAT material exhibit similar morphology, with small mean wall thicknesses of 4.2 and 4.9 nm. This thickness is only slightly larger than the calculated crystallite sizes of ca. 3 nm (XRD) for both samples and thus corresponds to walls made up of one to two primary particles. We observed a small increase of ∼1 nm in the necks connecting different sections of the walls in the HAAT material compared to the noHAAT material. In contrast, during aging the solid phase coarsens severely, as Figure 6b shows. This increase in wall thickness is larger in the noHAAT material (average wall thickness of ca. 36 nm) than in the HAAT sample (average wall thickness ca. 30 nm), which still features walls constituted by one to two particles as the crystallite size was determined to be around 20 nm.

Similar changes can also be observed in the mesopore space. Before aging, the materials feature a mean pore size similar to the mesopore dimension obtained from Ar physisorption (Figure 7). Similar to the increase in neck sizes in the walls, a widening of pore necks by ∼1 nm was observed. The HAAT material, furthermore, features an increased number of larger pores with a diameter of around 20 nm, which agrees with physisorption analysis (cf. Figure 1). During aging, the noHAAT material visibly loses a substantial fraction of the mesopore volume (seen in the change in ratio of solid-phase voxels to pore voxels) and apparently suffers from a dramatic reduction in pore connectivity. However, we note that the pores shown in Figure 6b might still be connected to the pore network in front of or behind the shown slice. In contrast to that, the slice of HAAT material reveals a highly interconnected pore network. Figure 6b also reveals the existence of pores with a diameter of up to 60 nm (dark-orange to red) in the 1050HAAT sample, which can hardly be resolved by physisorption and are thus not seen in the PSDs from physisorption.

CLD analysis provides an alternative method to statistically describe the feature sizes (pores/walls) in two-phase systems without an underlying assumption of a specific geometry. The chord length distribution is a distribution of surface-to-surface distances (chords) and can be obtained for each phase (e.g., solid and pore/void) individually. Here, the method developed by Bruns et al. was used, especially to analyze the mesopore phase with respect to the dominant contribution, i.e., pore dimensions.[27] Fitting the yielded histograms with a k-gamma function (Figure 8a) allows for a mathematical parametrization of the CLD,

$$f(l_c) = \frac{k^k l_c^{k-1}}{\Gamma(k)\mu_c^k} \exp\left(-k\frac{l_c}{\mu_c}\right) \quad (1)$$

where l_c represents the chord length, μ_c represents the mean chord length (first statistical moment), and k represents the ratio of the mean chord length and the standard deviation (second statistical moment).

$$k = \left(\frac{\mu_c}{\sigma}\right)^2 \quad (2)$$

The resulting k-gamma functions of the fitted pore phase CLDs are shown in Figure 8a along with the calculated mean chord lengths μ_c. The obtained curves for the 400 °C samples feature a maximum of between 5 and 6 nm, and μ_c = 9.9 nm for the noHAAT material and 11.0 nm for the HAAT material. Furthermore, the maximum dimension in the CLDs is up to 40 nm, which is quite large compared to the results of the local

https://doi.org/10.1021/acs.langmuir.2c02366
Langmuir 2023, 39, 177−191

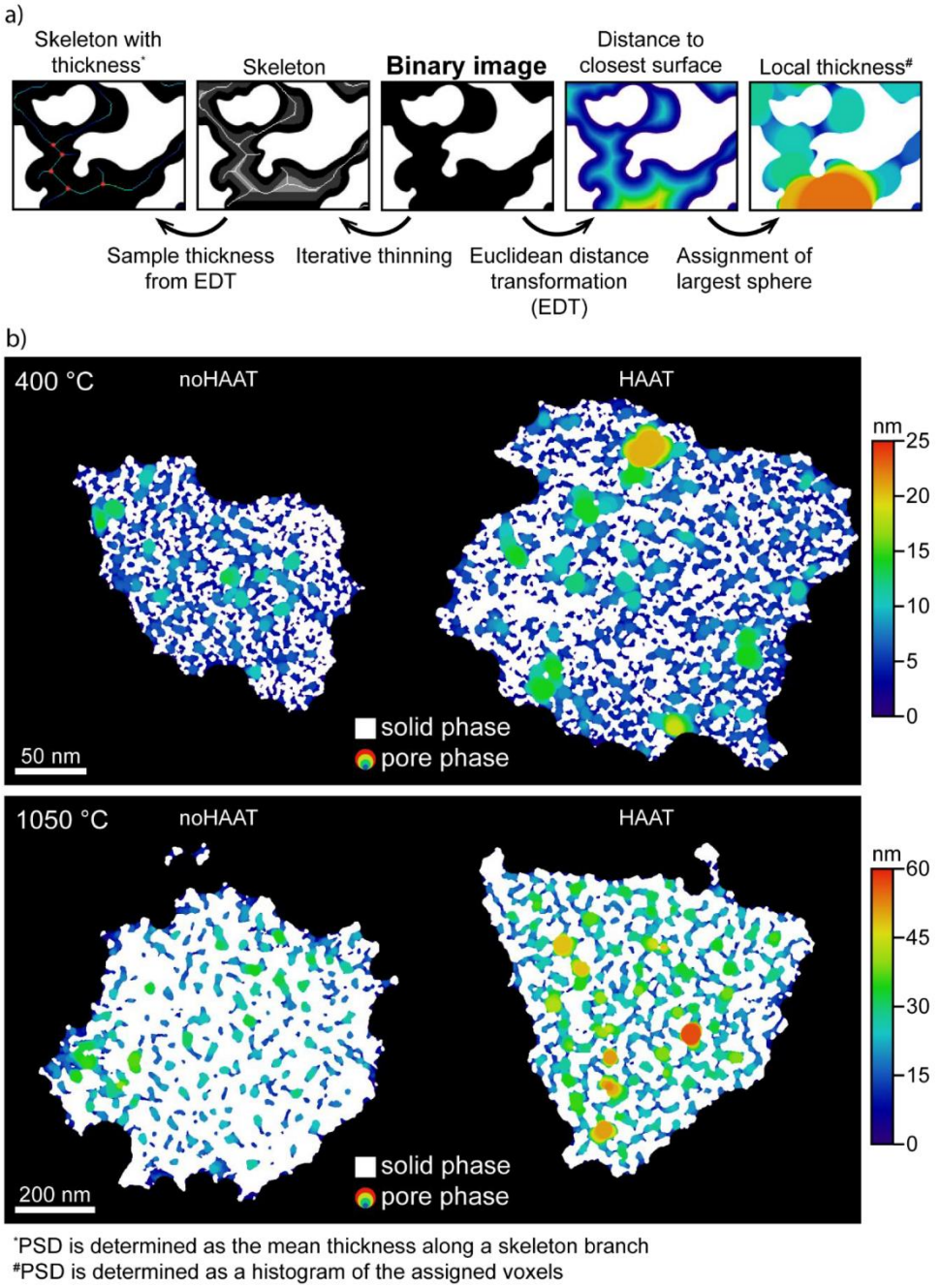

Figure 6. (a) Schematic procedure of the pore size analysis. (b) Slices through the 3D reconstructions of the analyzed particles. The solid phase is represented in white; pores are color coded according to their local thicknesses.

thickness and physisorption analysis. However, this finding can be explained by the fact that chords are also projected along and not only across the pores due to the equiangular spatial pattern of the projected chords, thus increasing the number of chords continuing into adjacent pores, causing an asymmetry in the resulting k-gamma fit. This effect is especially pronounced after aging of the samples at 1050 °C, where the CLD maxima shift to 16.6 nm for the noHAAT material and 29.8 nm for the HAAT material. Also, the treatment at 1050 °C results in a substantial broadening of the CLDs of the pore space of up to 70 nm in the

https://doi.org/10.1021/acs.langmuir.2c02366
Langmuir 2023, 39, 177−191

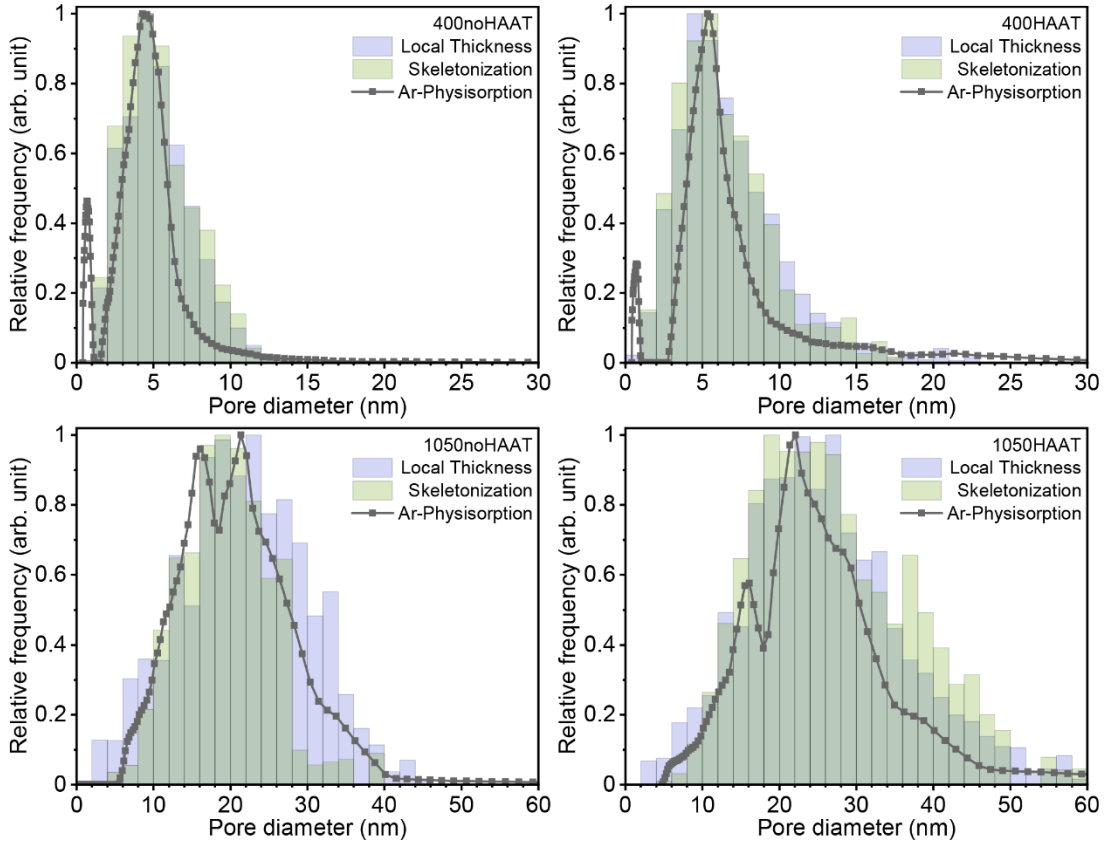

Figure 7. Normalized pore size distributions as obtained by Ar physisorption (87 K) and the STEM-based local thickness and skeletonization analyses.

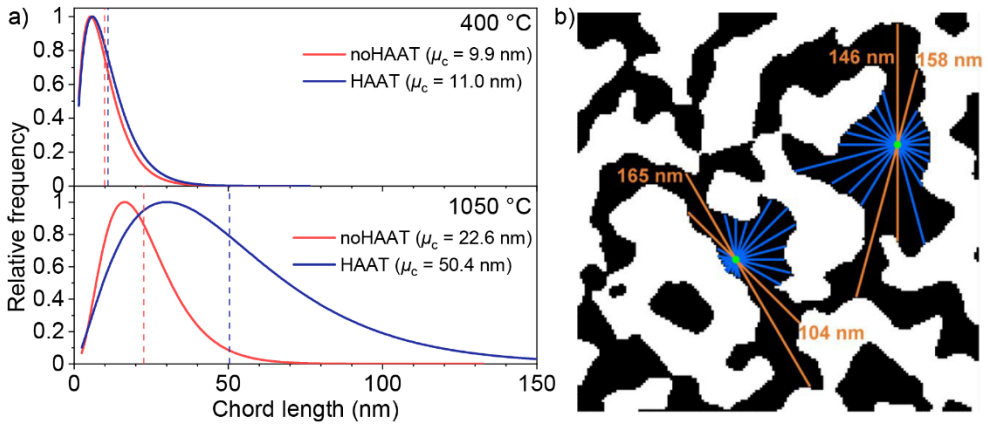

Figure 8. (a) k-gamma fits of the pore-phase CLDs. (b) Long chords spanning multiple pores in the continuous network, causing assymmetry in the CLD of the 1050noHAAT sample.

noHAAT and even beyond 150 nm in the HAAT material, corresponding to mean chord lengths of 22.6 and 50.4 nm, respectively. The large difference in the mean chord lengths is mainly caused by the increased frequency of very long chords spanning multiple pores due to the larger pore volume and superior pore connectivity in the sample subjected to the aftertreatment step in aqueous ammonia solution (cf. Figure 6b; bottom row). Figure 8b shows a set of exemplary chords exceeding a length of 100 nm in a single slice of the 1050HAAT sample. Hence, these observations suggest that the over-

https://doi.org/10.1021/acs.langmuir.2c02366
Langmuir 2023, 39, 177−191

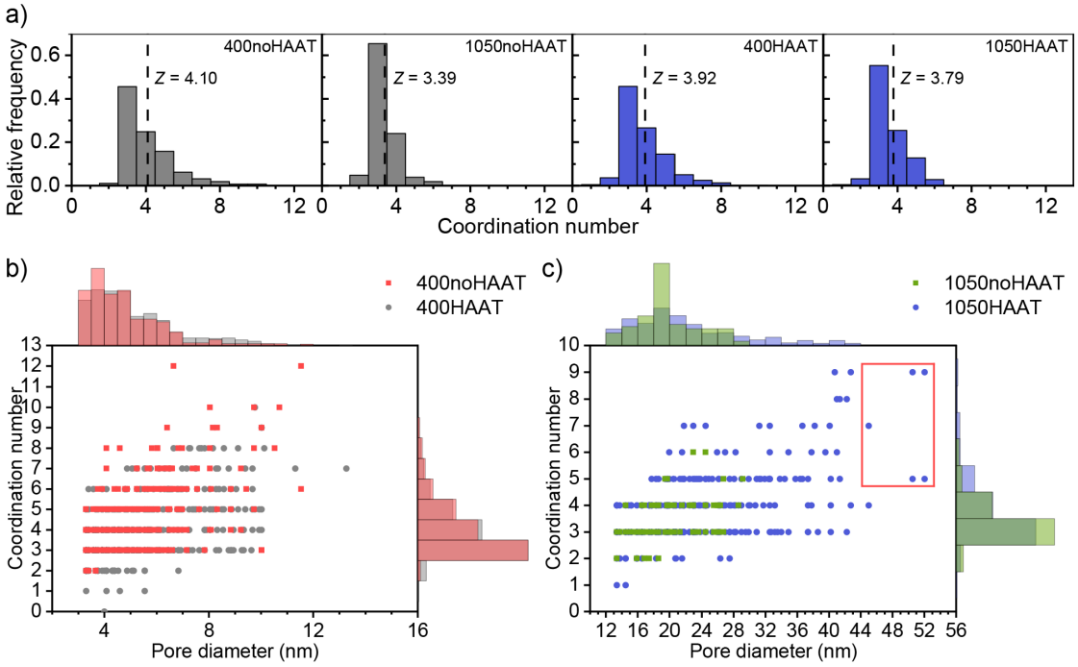

Figure 9. (a) Histograms showing the coordination number of pores, determined according to Cheng et al.[25] (b and c) Scatterplots of coordination numbers vs pore diameter for the different temperatures.

estimation of the mean chord lengths and pore diameters by the CLD analysis is caused by the high connectivity of the material subjected to the aftertreatment step. The mode values of l_c of the k-gamma curves, however, appear to closely resemble the mean pore sizes determined via the methods described above.

Similar conclusions can be drawn from the CLDs of the solid phase. For the 1050HAAT sample, the solid phase's CLD is similar to the CLD of the pore phase, resembling a complementary structure with equally sized walls ($\mu_{c,walls}$ = 57.1 nm, cf. Figure S7), hence analogously shifting the mean chord length to large values. The CLDs of the sample without HAAT, however, show a large discrepancy between the solid phase ($\mu_{c,walls}$ = 88.2 nm, cf. Figure S7) and the pore phase, which can be explained by the drastic coarsening of the sample's solid phase, forming a very dense material with little pore volume, as shown above (cf. Figure 6).

A powerful tool that can analyze both pore dimensions (diameter and length) and pore connectivity is the so-called skeletonization analysis. It provides a topology-preserving representation of the pore- or solid-phase's network by iteratively thinning the analyzed phase to its medial axis, creating a complex network of branches, e.g., pores, and nodes, with each node being a meeting point for multiple pores. The principle is sketched in Figure 6a. From this set of branches and nodes, structure-defining parameters such as the number of branches meeting in a node (local coordination number) as well as the length, diameter, and tortuosity of branches between nodes can be determined. Here, a 3D region of interest was extracted from each of the complete particles. The results of the skeletonization-based pore size analysis are shown in Figure 7 along with the previously discussed pore dimensions of the local thickness and physisorption analysis. Furthermore, the method allows a quantitative description of connectivity[25] in the present pore networks and the changes caused by the different synthesis routes and the effects of aging at 1050 °C. To achieve this, a set of regional maximal spheres representing pores are determined computationally, and, under the assumption that branching occurs where pores are largest, are used to obtain the local coordination of the pore. Histograms resulting from the analysis of coordination numbers are shown in Figure 9a. The corresponding mean coordination number Z (also shown in Figure 9a) was calculated according to eq 3, with n_t being the total number of nodes and n_b being the number of nodes, where b branches meet.

$$Z = \frac{1}{n_t}\sum_{b=3}^{x} bn_b \tag{3}$$

The histograms reveal that the most abundant coordination numbers are three and four for all samples. After calcination at 400 °C, the samples with and without HAAT feature a similar distribution of coordination numbers, resulting in Z = 3.92 and 4.10, respectively. In both cases, Z decreases upon aging at 1050 °C, as the fraction of pores with a coordination number of 4 is reduced. This change in the topology of the mesopore network signifies that the accessibility of the mesopore network is reduced, as the 3D structure is not preserved upon aging. However, this shift in Z to lower values is more pronounced in the sample prepared without HAAT (Z = 3.39), which, compared to the HAAT sample (Z = 3.79), undergoes a severe rearrangement in the solid phase, highlighting the improvement of thermal stability due to hydrothermal aftertreatment in aqueous ammonia solution. Furthermore, these data confirm the

https://doi.org/10.1021/acs.langmuir.2c02366
Langmuir 2023, 39, 177−191

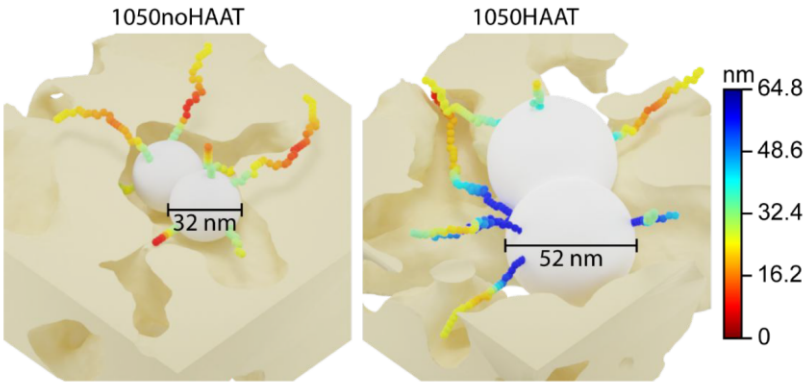

Figure 10. Three-dimensional sections of the materials (pale yellow) after aging at 1050 °C and two of the five largest spheres (white) used for the determination of the coordination number. The corresponding branches of the skeleton are color coded according to their local thickness. Narrow sections along these branches, the pore necks, are highlighted by a red color. As the spheres shown in both cases essentially belong to the same pore compartment, they are directly connected by a branch with the same pore diameter each. However, in this visualization these branches are occluded by the spheres due to their size.

continuous network character of the pore space as proposed by the results of the hysteresis scanning experiments.

Although the coordination numbers calculated from the skeleton analysis provide a powerful quantitative measure of the network connectivity, they do not hold information about the accessibility of the pores. Therefore, a more detailed analysis of the skeleton is required, considering the dimensions of the pores. Figure 9b,c shows scatterplots of the coordination number against the pore diameter (diameter of the corresponding regional maximal sphere) along with histograms displaying the population size of coordination numbers and pore sizes of the pores within the analyzed region of interest. While for the samples calcined at 400 °C no significant differences are observable, the samples differ strongly after aging (1050 °C). The scatterplot of the hydrothermally treated sample (Figure 9c) spreads more to the top right corner than does the untreated sample. Pores located in this plot region possess a larger diameter in combination with a high coordination number (>7). From a geometrical point of view, this behavior is consistent, as a large spherical pore provides more space at its boundary to accommodate pore necks than a smaller pore, assuming similar neck sizes. However, the diameter of the pore necks is a crucial factor in a pore's accessibility. As described above, the hysteresis scans of the aged samples (cf. Figure 3) and the comparison of PSDs derived from the adsorption and desorption isotherms (cf. Figure 4) suggest hindrance in the accessibility of the large pores within the PSD, being visible in the sharp bend of the boundary isotherms and the differences between the PSDs. To confirm this interpretation, we performed an analysis of the neck sizes of the five largest pores in each of the aged powders based on the branches obtained by skeletonization (Figure S8 and the accompanying description).

Figure 10 illustrates two of the largest pores from each of the aged samples and their corresponding branches of the skeleton that emerge from the spheres used for the determination of the coordination number. The branch diameters are color-coded according to the local thickness sampled along the branch, where the minimum value is considered to be the neck size. The large pores of the sample exposed to the aftertreatment in ammonia solution feature both small and very large necks of ca. 10 nm and up to ca. 55 nm, respectively. The largest neck diameters observed result from a direct connection between the spheres used for the determination of the coordination number, which in the cases shown in Figure 10 belong to the same pore compartment. Thus, in interpreting this analysis in terms of connectivity, the more relevant necks are those further from the center of the pores, i.e., necks that establish a connection to adjacent mesopores. The majority of such necks is in the size range of the mean pore size determined from Ar physisorption with diameters of 20−32 nm. In comparison to that, in the aged sample without HAAT even the largest pores are significantly smaller, with diameters of 25−30 nm. The smallest necks are in the range of 6−13 nm, and the largest necks have a diameter of 16−25 nm. The existence of small necks connecting these large pores to the pore network could explain the pore blocking observed in the boundary isotherm of the hysteresis scans and the corresponding PSDs (cf. Figures 3 and 4). However, at the same time these pores also feature larger necks similar to the mean pore sizes, which should provide good pore accessibility and contradict the observations from the physisorption experiments. To fully assess this phenomenon, we suggest a more global analysis of the pore network to be performed that also considers the necks of neighboring pores, as it is unclear if these large pores belong to a subnetwork within the pore system that is accessible only through small 5−15 nm necks. Unfortunately, such analysis is out of scope for this study, as such analysis is challenging. Nonetheless, it could help to further improve the interpretation of desorption isotherms, which we plan to address in the future.

Performing the same analysis for the pores in the size range of 16−23 nm, corresponding to the average pore size of the aged materials, paints a similar picture, where pores are predominantly connected by necks with a diameter of ∼20 nm, also featuring small 6−12 nm necks. These pores typically feature at least one neck with a size of 6−13 nm, which we deem a significant amount that supports the observed pore blocking.

■ CONCLUSIONS

In this study, we demonstrate the significant influence of a typical hydrothermal aftertreatment step on the connectivity of disordered mesopore networks of Y- and La-doped ceria-zirconia mixed oxides with high surface area. Aging at a high

https://doi.org/10.1021/acs.langmuir.2c02366
Langmuir 2023, 39, 177−191

temperature of 1050 °C was subsequently performed to simulate prolonged use as a catalyst support and to investigate the thermal stability. The disordered mesopore space of a crystalline, quaternary mixed oxide depending on typical chemical treatments and high-temperature treatment is characterized in depth using state-of-the-art methodology focusing on pore connectivity. The employed techniques comprise Ar physisorption, including advanced hysteresis scanning, combined with electron tomography to support the interpretation of the hysteresis scanning experiments. We believe that the present study provides an important advancement, as the presented procedure takes the characterization of disordered mesoporous materials a step beyond previous studies performed on silica materials,[22,24] which typically do not focus on chemical and thermal alterations and their effects on pore connectivity.

We show that the investigated hydrothermal aftertreatment significantly promotes the mesopore accessibility and thermal stability of the materials. However, upon aging at 1050 °C a growth in pore sizes accompanied by a loss in BET area and pore volume was observed in all materials, with the magnitude of these losses being smaller in the samples subjected to hydrothermal aftertreatment. Simultaneously to these changes in mesoporosity during aging, growth of the crystallites was observed, which appears to be independent of the hydrothermal aftertreatment. However, aging results in completely different morphologies of the materials, creating a densely packed material if no aftertreatment in ammonia solution is performed. Owing to the similar crystallization behavior, we suspect that the origin of the improved thermal stability is of a structural and surface-chemical nature, i.e., increased neck sizes between particles or the removal of surface-bound nitrate groups. Therefore, we plan to investigate the influence of this aftertreatment on surface-bound nitrate groups in the future, as we recently demonstrated[28] their substantial influence on the development of the mesopore morphology during calcination.

To validate the PSDs obtained from Ar physisorption, we employed multiple methods to determine PSDs from the 3D reconstructions generated by electron tomography, which all provided similar results. Among these, the local thickness approach has proven to be a valuable tool to analyze different aspects of the mesopore network, as it provides a reasonable and accurate pore size distribution and a comprehensible visualization of the spatial distribution of pore sizes, also highlighting the dimensions of pore connections. However, if further information on the pores, e.g., length, tortuosity, or the number of neighboring pores, is required, then a skeletonization-based analysis is mandatory. In the presented case, the skeletonization-based determination of pore sizes provided reliable results on pore sizes. For the CLD-based approach, we found that the mode of the CLD provided an estimation of the mean pore size closer to those obtained by methods other than the calculated mean chord length μ_c. This can be explained by the highly asymmetrical curves due to the pore connectivity, showing that special care has to be taken when interpreting such data.

We believe that the present study also nicely demonstrates the advantages and shortcomings of physisorption-based analysis and electron tomography and how the combination of both methods can be employed to fully characterize the mesopore space of disordered pore networks. While physisorption analysis can provide a qualitative description of differences in pore connectivity by the deduction of involved desorption mechanisms, it is not easy to quantify the connectivity. This is where electron tomography excels. However, as only a small amount of the material is reconstructed, pore size gradients or spatial inhomogeneities, for example, cannot be detected, which in turn can be indicated by hysteresis scans. Importantly, electron tomography was able to prove the existence of small necks surrounding larger mesopores, which was also suggested by physisorption analysis. Also, electron tomography showed that these larger mesopores are not surrounded exclusively by small necks but also by larger ones. However, owing to the small volume studied, electron tomography is not able to determine whether such a mesopore is connected to the external void volume only by small necks. Both methods together, as a relevant result, further support the recently introduced concepts explaining the pronounced hysteresis (connection of larger mesopores through small necks).[30] Additionally, our analyses support the interpretation of physisorption data of continuous mesoporous networks. The final notable difference between physisorption and electron tomography is the resolvable pore sizes. While both methods provide excellent results in the mesopore range, physisorption analysis can hardly resolve small macropores (50−100 nm). In turn, electron tomography is not capable of analyzing micropores (<2 nm), which, with the proper adsorptive, is easily realized with physisorption analysis and may provide valuable additional information.

Based on the insights gained in this study, we plan to investigate the influence of the differences in pore accessibility observed in the presented materials on the performance as an oxygen storage material. The so-called dynamic oxygen storage capacity (dOSC) could serve as a suitable parameter for investigating diffusion limitations caused by the observed small neck sizes, as it provides a practical approach to probing the oxygen uptake and release under transient conditions without the need to perform an actual conversion reaction in the presence of a platinum group metal dispersed on the surface of the oxygen storage material. Further attention should also be directed to the influence of parameters during hydrothermal ammonia aftertreatment on the pore connectivity, such as pH and temperature.

■ ASSOCIATED CONTENT

Supporting Information

The Supporting Information is available free of charge at https://pubs.acs.org/doi/10.1021/acs.langmuir.2c02366.

Python program used to isolate the pore space from the outer void space; angular ranges of the collected tils series; SEM and STEM images of the investigated materials; comparison of Ar and N_2 physisorption isotherms; NLDFT-fit comparisons; comparison of hysteresis loops with all adsorption branches included; slices through the 3D reconstructions showing the local thickness of the materials' solid phase; comparison of wall size distributions determined by local thickness and skeletonization; k-gamma fits of the solid-phase CLDs; summary of structural properties; schematic representation of the pore space and the skeletonization-based neck size analysis (PDF)

Video animation of the tilt series of the 1050HAAT sample (MP4)

Video animation of slices through the 1050HAAT sample (MP4)

Turntable video animation of the 3D reconstrution of the 1050HAAT sample (MP4)

https://doi.org/10.1021/acs.langmuir.2c02366
Langmuir 2023, 39, 177−191

1050HAAT (ZIP)

AUTHOR INFORMATION

Corresponding Author

Bernd M. Smarsly – *Institute of Physical Chemistry, Justus-Liebig University, 35392 Giessen, Germany; Center for Materials Research, 35392 Giessen, Germany;* orcid.org/0000-0001-8452-2663; Email: bernd.smarsly@phys.chemie.uni-giessen.de

Authors

Eric Prates da Costa – *Institute of Physical Chemistry, Justus-Liebig University, 35392 Giessen, Germany; Umicore AG & Co. KG, 63457 Hanau, Germany;* orcid.org/0000-0001-8163-7828

Xiaohui Huang – *Institute of Nanotechnology, Karlsruhe Institute of Technology, 76344 Eggenstein-Leopoldshafen, Germany; Department of Materials and Earth Sciences, Technical University Darmstadt, 64287 Darmstadt, Germany*

Christian Kübel – *Institute of Nanotechnology and Karlsruhe Nano Micro Facility (KNMF), Karlsruhe Institute of Technology, 76344 Eggenstein-Leopoldshafen, Germany; Department of Materials and Earth Sciences, Technical University Darmstadt, 64287 Darmstadt, Germany;* orcid.org/0000-0001-5701-4006

Xiaoyin Cheng – *Fraunhofer-Institut für Techno- und Wirtschaftsmathematik, 67663 Kaiserslautern, Germany*

Katja Schladitz – *Fraunhofer-Institut für Techno- und Wirtschaftsmathematik, 67663 Kaiserslautern, Germany*

Alexander Hofmann – *Umicore AG & Co. KG, 63457 Hanau, Germany;* orcid.org/0000-0001-9872-2156

Ulrich Göbel – *Umicore AG & Co. KG, 63457 Hanau, Germany*

Complete contact information is available at: https://pubs.acs.org/10.1021/acs.langmuir.2c02366

Funding

Financial support was provided by Umicore AG & Co. KG.

Notes

The authors declare no competing financial interest.

ACKNOWLEDGMENTS

Financial support was provided by Umicore AG & Co. KG. Further acknowledgement goes to the Center for Materials Research (LaMa) at Justus-Liebig University Giessen for the support of this project. X.H. acknowledges the China Scholarship Council (CSC) for the support of her Ph.D. at Karlsruhe Institute of Technology and the Technical University of Darmstadt.

REFERENCES

(1) Devaiah, D.; Reddy, L. H.; Park, S.-E.; Reddy, B. M. Ceria–zirconia mixed oxides: Synthetic methods and applications. *Catal. Rev. Sci. Eng.* **2018**, *60*, 177–277.

(2) Sun, Y.; Li, C.; Djerdj, I.; Khalid, O.; Cop, P.; Sann, J.; Weber, T.; Werner, S.; Turke, K.; Guo, Y.; Smarsly, B. M.; Over, H. Oxygen storage capacity versus catalytic activity of ceria–zirconia solid solutions in CO and HCl oxidation. *Catal. Sci. Technol.* **2019**, *9*, 2163–2172.

(3) Li, C.; Sun, Y.; Hess, F.; Djerdj, I.; Sann, J.; Voepel, P.; Cop, P.; Guo, Y.; Smarsly, B. M.; Over, H. Catalytic HCl oxidation reaction: Stabilizing effect of Zr-doping on CeO_2 nano-rods. *Applied Catalysis B: Environmental* **2018**, *239*, 628–635.

(4) Melchionna, M.; Fornasiero, P. The role of ceria-based nanostructured materials in energy applications. *Mater. Today* **2014**, *17*, 349–357.

(5) Montini, T.; Melchionna, M.; Monai, M.; Fornasiero, P. Fundamentals and Catalytic Applications of CeO_2-Based Materials. *Chem. Rev.* **2016**, *116*, 5987–6041.

(6) Pappacena, A.; Rancan, M.; Armelao, L.; Llorca, J.; Ge, W.; Ye, B.; Lucotti, A.; Trovarelli, A.; Boaro, M. New Insights into the Dynamics That Control the Activity of Ceria–Zirconia Solid Solutions in Thermochemical Water Splitting Cycles. *J. Phys. Chem. C* **2017**, *121*, 17746–17755.

(7) Di Monte, R.; Kašpar, J. On the Role of Oxygen Storage in Three-Way Catalysis. *Top. Catal.* **2004**, *28*, 47–57.

(8) Farrauto, R. J.; Deeba, M.; Alerasool, S. Gasoline automobile catalysis and its historical journey to cleaner air. *Nat. Catal* **2019**, *2*, 603–613.

(9) Groen, J. C.; Zhu, W.; Brouwer, S.; Huynink, S. J.; Kapteijn, F.; Moulijn, J. A.; Pérez-Ramírez, J. Direct demonstration of enhanced diffusion in mesoporous ZSM-5 zeolite obtained via controlled desilication. *J. Am. Chem. Soc.* **2007**, *129*, 355–360.

(10) Pérez-Ramírez, J.; Christensen, C. H.; Egeblad, K.; Christensen, C. H.; Groen, J. C. Hierarchical zeolites: enhanced utilisation of microporous crystals in catalysis by advances in materials design. *Chem. Soc. Rev.* **2008**, *37*, 2530–2542.

(11) Kenvin, J.; Mitchell, S.; Sterling, M.; Warringham, R.; Keller, T. C.; Crivelli, P.; Jagiello, J.; Pérez-Ramírez, J. Quantifying the Complex Pore Architecture of Hierarchical Faujasite Zeolites and the Impact on Diffusion. *Adv. Funct. Mater.* **2016**, *26*, 5621–5630.

(12) Hartmann, M.; Machoke, A. G.; Schwieger, W. Catalytic test reactions for the evaluation of hierarchical zeolites. *Chem. Soc. Rev.* **2016**, *45*, 3313–3330.

(13) Hirano, M.; Hirai, K. Effect of Hydrolysis Conditions on the Direct Formation of Nanoparticles of Ceria–Zirconia Solid Solutions from Acidic Aqueous Solutions. *J. Nanopart. Res.* **2003**, *5*, 147–156.

(14) Si, R.; Zhang, Y.-W.; Li, S.-J.; Lin, B.-X.; Yan, C.-H. Urea-Based Hydrothermally Derived Homogeneous Nanostructured $Ce_{1-x}Zr_xO_2$ (x = 0–0.8) Solid Solutions: A Strong Correlation between Oxygen Storage Capacity and Lattice Strain. *J. Phys. Chem. B* **2004**, *108*, 12481–12488.

(15) Di Monte, R.; Kašpar, J.; Bradshaw, H.; Norman, C. A rationale for the development of thermally stable nanostructured CeO_2-ZrO_2-containing mixed oxides. *Journal of Rare Earths* **2008**, *26*, 136–140.

(16) Chuah, G. K.; Jaenicke, S.; Pong, B. K. The Preparation of High-Surface-Area Zirconia. *J. Catal.* **1998**, *175*, 80–92.

(17) Raju, V.; Jaenicke, S.; Chuah, G.-K. Effect of hydrothermal treatment and silica on thermal stability and oxygen storage capacity of ceria–zirconia. *Applied Catalysis B: Environmental* **2009**, *91*, 92–100.

(18) Ohtake, N.; Katoh, M.; Sugiyama, S. High thermal-stability ceria synthesized via thermal-hydrolysis route and methane-combustion performance. *J. Ceram. Soc. Japan* **2017**, *125*, 57–61.

(19) Özkan, E.; Hofmann, A.; Votsmeier, M.; Wang, W.; Huang, X.; Kübel, C.; Badaczewski, F.; Turke, K.; Werner, S.; Smarsly, B. M. Comprehensive Characterization of a Mesoporous Cerium Oxide Nanomaterial with High Surface Area and High Thermal Stability. *Langmuir* **2021**, *37*, 2563–2574.

(20) Stoeckel, D.; Kübel, C.; Hormann, K.; Höltzel, A.; Smarsly, B. M.; Tallarek, U. Morphological analysis of disordered macroporous-mesoporous solids based on physical reconstruction by nanoscale tomography. *Langmuir* **2014**, *30*, 9022–9027.

(21) Stoeckel, D.; Kübel, C.; Loeh, M. O.; Smarsly, B. M.; Tallarek, U. Morphological Analysis of Physically Reconstructed Silica Monoliths with Submicrometer Macropores: Effect of Decreasing Domain Size on Structural Homogeneity. *Langmuir* **2015**, *31*, 7391–7400.

(22) Cimino, R.; Cychosz, K. A.; Thommes, M.; Neimark, A. V. Experimental and theoretical studies of scanning adsorption–desorption isotherms. *Colloids Surf., A* **2013**, *437*, 76–89.

(23) Schlumberger, C.; Thommes, M. Characterization of Hierarchically Ordered Porous Materials by Physisorption and Mercury

Porosimetry—A Tutorial Review. *Adv. Mater. Interfaces* **2021**, *8*, 2002181.
(24) Kube, S. A.; Turke, K.; Ellinghaus, R.; Wallacher, D.; Thommes, M.; Smarsly, B. M. Pore Size Gradient Effect in Monolithic Silica Mesopore Networks Revealed by In-Situ SAXS Physisorption. *Langmuir* **2020**, *36*, 11996−12009.
(25) Cheng, X.; Föhst, S.; Redenbach, C.; Schladitz, K.Detecting Branching Nodes of Multiply Connected 3D Structures. In *Proceedings of the Mathematical Morphology and its Applications to Signal and Image Processing: 14th international symposium, ISMM 2019*; Saarbrücken, Germany, July 8−10, 2019; Burgeth, B., Kleefeld, A., Naegel, B., Passat, N., Perret, B., Eds.; Springer International Publishing: Cham, 2019; Vol. *11564*, pp 441−455.
(26) Gostick, J.; Khan, Z.; Tranter, T.; Kok, M.; Agnaou, M.; Sadeghi, M.; Jervis, R. PoreSpy: A Python Toolkit for Quantitative Analysis of Porous Media Images. *JOSS* **2019**, *4*, 1296.
(27) Bruns, S.; Müllner, T.; Kollmann, M.; Schachtner, J.; Höltzel, A.; Tallarek, U. Confocal laser scanning microscopy method for quantitative characterization of silica monolith morphology. *Analytical chemistry* **2010**, *82*, 6569−6575.
(28) Prates da Costa, E.; Hofmann, A.; Göbel, U.; Cop, P.; Smarsly, B. M. Development of Pore Morphology During Nitrate Group Removal by Calcination of Mesoporous $Ce_xZr_{1-x-y-z}Y_yLa_zO_{2-\delta}$ Powders. *Langmuir* **2022**, *38*, 8342−8352.
(29) Thommes, M.; Kaneko, K.; Neimark, A. V.; Olivier, J. P.; Rodriguez-Reinoso, F.; Rouquerol, J.; Sing, K. S. Physisorption of gases, with special reference to the evaluation of surface area and pore size distribution (IUPAC Technical Report). *Pure Appl. Chem.* **2015**, *87*, 1051−1069.
(30) Thommes, M.; Smarsly, B.; Groenewolt, M.; Ravikovitch, P. I.; Neimark, A. V. Adsorption hysteresis of nitrogen and argon in pore networks and characterization of novel micro- and mesoporous silicas. *Langmuir* **2006**, *22*, 756−764.
(31) Kleitz, F.; Bérubé, F.; Guillet-Nicolas, R.; Yang, C.-M.; Thommes, M. Probing Adsorption, Pore Condensation, and Hysteresis Behavior of Pure Fluids in Three-Dimensional Cubic Mesoporous KIT-6 Silica. *J. Phys. Chem. C* **2010**, *114*, 9344−9355.
(32) Weyland, M.; Midgley, P. A.; Thomas, J. M. Electron Tomography of Nanoparticle Catalysts on Porous Supports: A New Technique Based on Rutherford Scattering. *J. Phys. Chem. B* **2001**, *105*, 7882−7886.
(33) Kübel, C.; Voigt, A.; Schoenmakers, R.; Otten, M.; Su, D.; Lee, T.-C.; Carlsson, A.; Bradley, J. Recent advances in electron tomography: TEM and HAADF-STEM tomography for materials science and semiconductor applications. *Microscopy and microanalysis the official journal of Microscopy Society of America, Microbeam Analysis Society, Microscopical Society of Canada* **2005**, *11*, 378−400.
(34) Hochstrasser, J.; Svidrytski, A.; Höltzel, A.; Priamushko, T.; Kleitz, F.; Wang, W.; Kübel, C.; Tallarek, U. Morphology-transport relationships for SBA-15 and KIT-6 ordered mesoporous silicas. *Physical chemistry chemical physics PCCP* **2020**, *22*, 11314−11326.
(35) Reich, S.-J.; Svidrytski, A.; Höltzel, A.; Wang, W.; Kübel, C.; Hlushkou, D.; Tallarek, U. Transport under confinement: Hindrance factors for diffusion in core-shell and fully porous particles with different mesopore space morphologies. *Microporous Mesoporous Mater.* **2019**, *282*, 188−196.
(36) Tallarek, U.; Hochstrasser, J.; Ziegler, F.; Huang, X.; Kübel, C.; Buchmeiser, M. R. Olefin Ring-closing Metathesis under Spatial Confinement: Morphology−Transport Relationships. *ChemCatChem.* **2021**, *13*, 281−292.

https://doi.org/10.1021/acs.langmuir.2c02366
Langmuir 2023, 39, 177−191

3.3 Tuning Mesopore Accessibility of High Surface Area Doped Ceria-zirconia Mixed Oxides by Hydrothermal Posttreatment

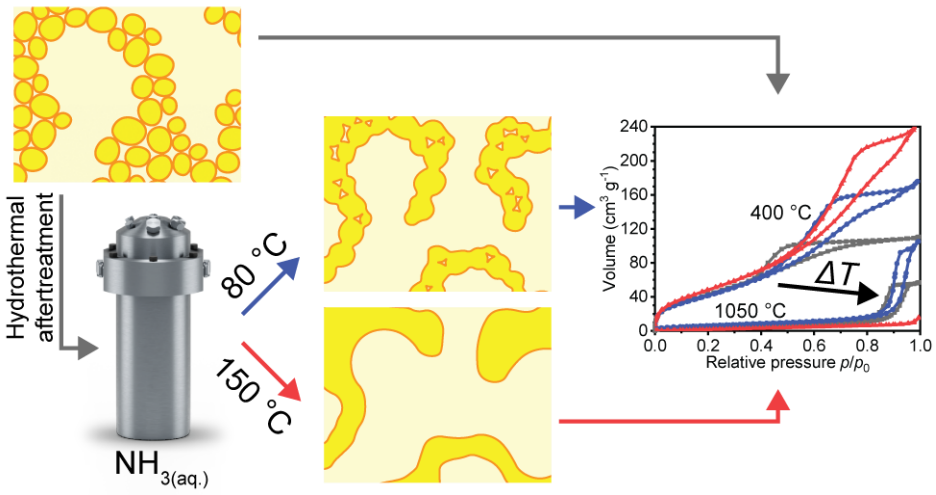

Prates da Costa, E., Huang, X., Kübel, C., Cheng, X., Schladitz, K., Hofmann, A., Göbel, U., Smarsly, B. M. Tuning Mesopore Accessibility of High Surface Area Doped Ceria-zirconia Mixed Oxides by Hydrothermal Posttreatment, *submitted to Langmuir*.

Tuning Mesopore Accessibility of High Surface Area Doped Ceria-zirconia Mixed Oxides by Hydrothermal Posttreatment

Eric Prates da Costa[a,b], *Xiaohui Huang*[c,e], *Christian Kübel*[c,d,e], *Xiaoyin Cheng*[f], *Katja Schladitz*[f], *Alexander Hofmann*[b], *Ulrich Göbel*[b], *Bernd M. Smarsly*[a,g]*

a. Institute of Physical Chemistry, Justus-Liebig University, Heinrich-Buff-Ring 17, 35392 Giessen, Germany.

b. Umicore AG & Co. KG, Rodenbacher Chaussee 4, 63457 Hanau, Germany.

c. Institute of Nanotechnology, Karlsruhe Institute of Technology, Hermann-von-Helmholtz Platz 1, 76344 Eggenstein-Leopoldshafen, Germany.

d. Karlsruhe Nano Micro Facility (KNMF), Karlsruhe Institute of Technology, Hermann-von-Helmholtz Platz 1, 76344 Eggenstein-Leopoldshafen, Germany.

e. Department of Materials and Earth Sciences, Technical University Darmstadt, Alarich-Weiss-Str. 2, 64287 Darmstadt, Germany.

f. Fraunhofer-Institut für Techno- und Wirtschaftsmathematik, Fraunhofer-Platz 1, 67663 Kaiserslautern, Germany.

g. Center for Materials Research, Heinrich-Buff-Ring 16, 35392 Giessen, Germany.

KEYWORDS Physisorption, hysteresis-scanning, scanning transmission electron microscopy, electron tomography, small angle X-ray scattering, ceria-zirconia, mesoporous, hydrothermal treatment

ABSTRACT

The connectivity and thermal stability of pores in heterogenous, mesoporous metal oxide catalysts are key properties controlling their (long-term) efficacy. In this study we investigate the influence of conditions like pH and temperature during a common hydrothermal aftertreatment step in the synthesis of mesoporous $Ce_xZr_{1-x-y-z}Y_yLa_zO_{2-\delta}$ oxides obtained from molecular precursors via hydrothermal synthesis. This study has a strong focus on the methodological approach, elucidating whether and how even the smallest changes in morphology and connectivity may be unraveled and related to the underlying chemical processes, to uncover key parameters for the ongoing improvement of material properties. Deep insights into the mesopore space were obtained by state-of-the-art physisorption (including hysteresis scanning), electron tomography as well as small angle X-ray scattering (SAXS) analysis. We also provide a simple tool to simulate SAXS curves from electron tomography data that allow a direct comparison to experimentally obtained SAXS curves. Furthermore, the impact on surface-bound nitrate groups and the development during calcination was studied in detail by thermogravimetric analysis coupled with mass spectrometry. The key observations indicate a significant increase in thermal stability at temperatures as high as 1050 °C and improved mesopore accessibility with an increasing pH of the aftertreatment solution. The combined observations from the employed methods suggest a pH dependent removal of surface-bound nitrate groups as well as a dissolution and re-precipitation-based fusing of the primary particles that constitute the mesopore skeleton. This transformation yields a mechanically and thermally stronger mesopore space with the capability to endure high temperatures.

Introduction

Due to their ability to store and release oxygen, mesoporous ceria-based mixed oxides are widely applied in catalysis as oxygen storage materials (OSMs).[1,2] The biggest field of application is automotive catalysis for the removal of toxic emissions from automotive exhausts (three-way catalysis; TWC), where they are employed as active support materials for precious metals in the form of complex mixed metal oxides containing other metals such as Zr, Y, or La to enhance catalytic properties. However, they have shown promise in other applications such as HCl oxidation[3,4] and thermochemical water splitting[5,6] for hydrogen generation as well. Their oxygen storage capabilities result from the special redox chemistry, that facilitates an easy and reversible switch of the oxidation state of the cerium from Ce^{4+} to Ce^{3+}. High oxygen storage capacity (OSC), specific surface area and thermal stability are commonly required properties in catalytic applications, which can be readily tuned by a large variety of available synthesis methods and their conditions.[3,7] Besides the chemical composition and thermal stability, the morphology of the mesopore network is a crucial factor that governs the performance of heterogeneous catalysts, as it directly influences the diffusion of reactants and ultimately the accessibility of active sites within the pores. Particularly in TWC, mesopore connectivity can also affect the long-term performance of the OSMs, because valuable precious metals used as active compounds may become trapped in pores and rendered inaccessible. Previous studies on ceria-based OSMs have mainly concentrated on the impact of different synthesis approaches on the thermal stability of these materials, focusing on pore volume and specific surface areas, obtained by simple physisorption analysis, as main descriptors related to thermal stability of mesoporosity.[8,9] So far, for these materials the investigation of mesopore connectivity has not played a major role, mainly due to the availability and usability of suitable standard characterization methods. However, understanding the 3D arrangement and connectivity of mesopores as well as the dimensions of pore walls of ceria-based OSMs and how they can be tuned by the synthesis approach is essential for the rational design and ongoing optimization of these materials. High resolution electron tomographic analysis is one approach that can provide direct 3D structural information on the pore morphology.[10–13] However, due to the high experimental effort for reliable electron tomographic analysis, this is not suitable as a screening tool for a large set of samples, e.g., to evaluate a wide range of synthesis conditions. A promising tool that capable of being applied on a routine basis is so-called hysteresis scanning. Currently this technique is mainly applied in specialized sorption research, to elucidate the connectivity of mesopores, due to the still difficult interpretation of scanning isotherms.[14–16] However, in contrast to electron tomography, it allows for a comparably quick measurement and data evaluation, making it a promising tool that is capable of being applied on a routine basis. While

a hysteresis scanning experiment can be completed within mere days, a comprehensive electron tomography analysis may take several weeks to finalize. Hence, if the additional information on the material's solid phase that is provided by electron tomography is not required, hysteresis scanning presents a viable alternative. We are convinced that a more advanced physisorption analysis, also employing hysteresis scanning, combined with a systematic approach to trace the influence of synthesis parameters and steps on the mesopore space allows to overcome this issue.

As an important common feature, these commercialized protocols for the syntheses of such CeO_2-based materials use nitrates as educts for all involved compounds (Zr, Y, …), as these nitrates possess high solubility. Unlike chloride precursors, which require extensive washing procedures to later prevent interference with the dispersed precious metals, they are readily removable from the final material via calcination. Also, being a very weak base and chemically inert under reaction conditions, NO_3^- does not interfere with the sol-gel reactions. Our previous studies, employing a thorough physisorption analysis, have demonstrated the critical impact of the removal of surface-bound nitrate groups by calcination on the mesoporous network of pure ceria[17] and rare earth doped ceria-zirconia mixed oxides[18], obtained *via* a modified hydrothermal synthesis adapted from Ohtake et al.[8] as depicted in Scheme 1.

Scheme 1. Investigated Synthesis Procedure. Reproduced from Prates da Costa et al.[19] Copyright 2023 American Chemical Society.

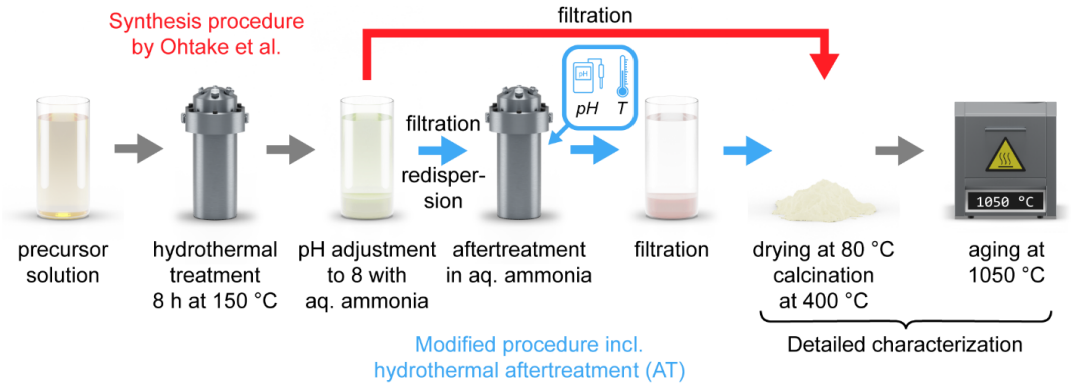

In these syntheses, the surface-bound nitrate groups act as a protective surface layer that slows down sintering, enabling the formation of a thermally stable mesoporous skeleton. Following this, in a recent study[19] we investigated the impact of hydrothermal aftertreatment in aqueous ammonia solution of wet $Ce_{0.18}Zr_{0.64}Y_{0.15}La_{0.03}O_{2-\delta}$ filter cakes, prepared by the same synthesis route.

In comparison to the untreated material the aftertreatment improved mesopore connectivity and increased thermal stability upon high temperature aging, agreeing with the scarce literature on comparably treated ceria-zirconia.[20–22] The focus of our recent study, however, was on the development of characterization procedures, as these materials feature highly disordered mesopore networks, which are difficult to analyze by standard physisorption analysis, i.e., analysis of a single isotherm. Yet, the impact on the surface-bound nitrate groups remained unclear. In search of a rationale for the observed improvement of thermal stability and connectivity, in the present study we shift the focus to the influence of the conditions during the hydrothermal aftertreatment step in aqueous ammonia solution. Especially we focus on the impact on the surface-bound nitrate groups and the final mesoporosity. We presume that an aftertreatment in aqueous ammonia solution might drastically reduce the surface coverage with nitrate groups and, hence, their stabilizing properties towards sintering. Such aftertreatment has previously been shown to significantly strengthen the materials against thermal degradation,[19] possibly presenting a mild alternative to calcination for the removal of residual nitrates. Besides possible surface-chemical alterations, such post treatment under basic conditions is known from classical Sol-Gel-Science to significantly alter the pore structure.[23] It is known to cause transformations to the gel networks, such as condensation, dissolution and re-precipitation, or crystallization, which drastically affect subsequent drying and sintering processes. To untangle the chemical and structural effects, a highly detailed characterization of the mesopore space in dependence of synthesis parameters is required. In this work we make use of the recently established characterization concepts on materials obtained by a systematic variation of the hydrothermal aftertreatment pH and temperature and test the thermal stability of the mesopore space by aging at 1050 °C, simulating peak exhaust temperatures. State-of-the-art Ar-physisorption, electron tomography and small angle X-ray scattering (SAXS) analysis were employed, to fully describe the structural alterations and quantify mesopore connectivity in dependence of the underlying synthesis procedure. To validate, whether the 3D-reconstructions obtained from electron tomography are representative of the bulk material, we simulate SAXS curves from the reconstructions and compare those to measured SAXS data. Such validation is crucial, in order to allow for a meaningful comparison of physisorption data to the reconstructions, as electron tomography provides only a very localized section of a sample. Furthermore, we performed thermogravimetric analysis coupled with mass spectrometry (TG-MS), to elucidate the impact of hydrothermal aftertreatment in aqueous ammonia solution on the surface-bound nitrate groups, tracing the removal of residual moieties and their impact on sintering upon calcination and high temperature aging. The goal of this study is to develop a more detailed picture of the chemical aspects of the synthesis and how they affect the

morphology of the mesopore space, to aid in the further optimization of doped mesoporous ceria-zirconia.

Materials and Methods

Preparation of $Ce_{0.18}Zr_{0.64}Y_{0.15}La_{0.03}O_{2-\delta}$ Powders

The $Ce_{0.18}Zr_{0.64}Y_{0.15}La_{0.03}O_{2-\delta}$ powders were prepared by a hydrothermal synthesis route adapted from Ohtake et al.[8] with an additional hydrothermal aftertreatment step performed at varying pH (hereinafter denoted as "(*Calc. temp*)**AT**(*AT temp.*)/(*pH*)", i.e., 400AT80/6.9). In the first step of the synthesis an aqueous solution (1.4 L) with a total metal-ion concentration of 0.464 mol L^{-1} was prepared from $(NH_4)_2[Ce(NO_3)_6]$ (99.1%, Treibacher Industrie AG), $ZrO(NO_3)_2$ (20 wt% aq. solution, >98%, Luxfer MEL Technologies), $Y(NO_3)_3 \cdot 6H_2O$ (>99%, Treibacher Industrie AG), and $La(NO_3)_3 \cdot 6H_2O$ (≥99.99%, Carl Roth GmbH + Co. KG) with a molar ratio of Ce^{4+}:ZrO^{2+}:Y^{3+}:La^{3+} = 0.18:0.64:0.15:0.03. The precursor solution was placed in a stirred 2 L autoclave (Parr) and the initial pressure was set to 2 bar with compressed air. The solution was heated to 150 °C for 8 h under continuous stirring. After cooling to room temperature, the pH of the solution was set to 8 by adding an aqueous ammonia solution (25 wt%, ca. 130 mL). The pale-brown precipitate was filtered, and the wet filter cake (ca. 240 g) was redispersed in 1120 g of an aqueous ammonia solution (5 wt%, 10 wt%; pH 10.9 and 11.3), an aqueous solution of nitric acid (5 wt%; pH −0.2) or 1120 g of demineralized water (pH 6.9). A pH of 9.0 was achieved by redispersing the filter cake in 1120 g of demineralized water and dropwise addition of an aqueous ammonia solution (25 wt%) until the desired pH was reached. The obtained mixture was placed in the autoclave again for the aftertreatment (at 2 bar of compressed air) and heated to 80 °C for 11 h under continuous stirring. Afterwards, the pale-yellow precipitates were filtered without washing and subsequently dried at 80 °C for 18 h. Finally, the powders were calcined at 400 °C for 10 h.

A reference powder, which was not subjected to the aftertreatment procedure and instead directly calcined after the first filtration step, was prepared. Additionally, the aftertreatment in aqueous ammonia solution (5 wt%, pH 10.9) was performed at 150 °C to elucidate the influence of the aftertreatment temperature. Further, a sample of each prepared powder was aged in ambient air at 1050 °C for 4 h, to investigate the thermal stability of the powders. The heating rate to reach the desired temperatures for calcination and aging was 5 K min^{-1}.

Characterization

Physisorption was measured using Argon (87 K) or Nitrogen (77 K) on an *Autosorb iQ2 automated gas sorption analyzer* (*Quantachrome Instruments*). All samples were degassed under vacuum at 120 °C for 18 h before measuring. *ASiQwin Version 4.0* (*Quantachrome Corporation*) was used for data analysis. Specific surface areas were determined by the Brunauer-Emmett-Teller (BET) method over a relative pressure range of p/p_0 = 0.05–0.30. A non-

localized Density Functional Therory (NLDFT) Kernel of Ar at 87 K (or N_2 at 77 K) on zeolites/silica was applied to calculate pore size distributions (PSDs), assuming cylindrical pores.

XRD Powder diffraction patterns were measured using an *Empyrean diffractometer* (*PANalytical*) with Cu-Kα radiation at 40 kV and an output current of 40 mA. The Scherrer equation was applied to calculate crystallite sizes from the reflections, fitted in *HighScore Plus Version 3.0.5* (*PANalytical*).

SEM Scanning electron microscopy was performed on a *Smart SEM MERLIN scanning electron microscope* (*Carl Zeiss*) after sputtering the samples with platinum for 60 s. The acceleration voltage was set to 3 kV and the sample current to 78 pA.

TGA-MS Thermogravimetric analysis was performed on a *STA409 PC Luxx thermogravimetric analyzer* (*Netzsch*) with a heating rate of 5 K min^{-1} over a temperature range from 25 to 1050 °C, using synthetic air (80% N_2, 20% O_2) as carrier gas. On-line mass spectrometry was performed on a *QMS Aëolos Quadro quadrupole mass spectrometer* (*Netzsch*) over a m/z range of 12–100.

SAXS Small Angle X-ray Scattering experiments were performed on a *SAXSpoint 2.0* (Anton Paar, Austria) laboratory SAXS instrument using point-focused/slit-collimated Cu-Kα radiation with a wavelength of 0.154 nm from a micro-source (operated at 50 W) and an EIGER2 R 500K hybrid pixel area X-ray detector (Dectris, Baden-Daettwil, Switzerland). For the measurements the powder samples were transferred into a motorized VarioStage sample holder (Anton Paar, Graz, Austria), consisting of a 1 mm thick metal plate with 20 squared holes. The samples plate was sealed with a vacuum-tight sealing tape from both sides. SAXS patterns of the samples and the backround (sealing tape) were recorded in vacuum (ca. 1 mbar) at 25 °C at a sample-to-detector distance of 575.65 mm. The exposure time of each measurement was two minutes. The recorded 2D-SAXS patterns were radially integrated in order to obtain 1D-SAXS curves of the scattering intensity as a function of the scattering vector *q*. Further, the raw data was corrected for transmission and background scattering. Chord-length-distributions (CLDs) were determined by a parametrization based approach, described in previous publications.[24,25]

STEM tomography Scanning transmission electron microscopy (STEM) based tomography was conducted on a Themis 300 transmission electron microscope (Thermo-Fischer Scientific, Portland, Oregon, USA) equipped with a probe aberration corrector and operated at 300 kV. Samples were prepared by grinding ca. 10 mg of the powders and suspending them in ethanol. The suspensions were dropped on 100 x 400 mesh carbon-coated Cu grids (*Quantafoil Micro Tools GmbH*) on which Au nanoparticles ($d_{Au\text{-}np}$(400 °C) = 6 nm, $d_{Au\text{-}np}$(1050 °C) = 12 nm) had been deposited as fiducial markers. Prior to the image acquisition, the samples were cleaned two times for 30 s using an *Fischione 1070 Plasmacleaner* in Ar/O_2 with a power of 50%. Collection of tilt series

was performed with a high-angular annular dark-field (HAADF) detector with a step size of 2° over the tilt ranges shown in Table S1. Alignment of the tilt series was performed in *IMOD Version 4.11.7* (*University of Colorado, Denver, Colorado, USA*) using the deposited Au fiducial markers. Resulting residual alignment errors and resolutions are also listed in Table S1. Reconstruction of the aligned tilt series was performed in the ASTRA toolbox[26–28] (imec-Vision Lab, University of Antwerp; CWI, Amsterdam) in MATLAB using the Discrete Algebraic Reconstruction Technique (DART) on a Windows Server (2019) equipped with a NVIDIAQuadro RTX 8000 graphics card. An initial Simultaneous Iterative Reconstruction Technique (SIRT) reconstruction with 150 iterations was used as input for DART. The main loop for DART was repeated 10 times and then SIRT with another 150 iterations was included for each loop to ensure convergence. The grey levels used for segmentation were estimated from the average intensity of each component based on the initial SIRT reconstruction. During the DART reconstruction, the random probability was fixed to 0.3 and a 3 × 3 Gaussian filter was used to smooth the re-projected sinogram in each loop.

Morphological analysis The analysis of the resulting image stacks was performed analogously to our previous publication.[19] The Local Thickness plugin in Fiji was used to calculate the mesopore and wall size distributions of the full particles as a histogram of the assigned thickness values.[29] Topological analysis was performed by the procedure presented by Cheng et al.[30] to determine the local pore connectivity, using MAVI and TooIIP (Fraunhofer ITWM). The mean coordination number Z was calculated according to eq. (1, with n_t the total number of nodes and n_b the number of nodes, where b branches meet.

$$Z = \frac{1}{n_t}\sum_{b=3}^{x} b \cdot n_b \qquad (1)$$

To further compare the reconstructions to the obtained SAXS curves we implemented the algorithm described by Schmidt-Rohr[31] in Python to calculate SAXS curves from the electron tomography data. For a detailed description of the method please refer to the main text. The program is available on gitlab.[32]

Results and Discussion

General Characterization

Here we apply a modification of the synthetic procedure described by Ohtake et al.[8] to produce doped ceria-zirconia mixed oxides with an additional hydrothermal aftertreatment step conducted at varying pH. Analogously to our recent investigations[17–19], the obtained powders feature a special structure of agglomerated spheres with a diameter of ca. 5 µm, as shown in the scanning electron microscopy (SEM) images in Figure S1. This spherical superstructure is preserved under basic hydrothermal aftertreatment conditions at both temperatures investigated (80 °C and 150 °C) but is destroyed upon hydrothermal aftertreatment under acidic and neutral conditions. Furthermore, this spherical superstructure is thermally stable when aged at 1050 °C for most samples. Exceptions to this are

the powders, whose spherical structure is already destroyed during aftertreatment under acidic or neutral conditions (AT80/−0.2 and AT80/6.9) and the sample, where the hydrothermal aftertreatment was performed in aqueous ammonia solution at 150 °C (AT150/10.9). The spherical particles themselves are composed of small, crystalline primary particles, as the broad reflections in the XRD patterns (Figure S2) reveal. The powders feature a fluorite-type cubic phase with broad reflections due to the small crystallites. The crystallite sizes – determined by the Scherrer method – of ca. 3 nm after calcination at 400 °C and ca. 20 nm after aging at 1050 °C appear to be unaffected by the hydrothermal aftertreatment. However, already after calcination the powder treated in acidic solution shows a small shift in 2θ to higher angles. This shift is enlarged upon aging at 1050 °C, accompanied by a splitting of the (200)- and (311)-reflection, indicating the presence of a tetragonal phase. Such observation could be caused by the preferred dissolution of one of the contained oxides, resulting in a change of composition and hence the formation of a zirconia-like tetragonal lattice. To elucidate the influence of the aftertreatment procedure, the composition of the synthesized powders was determined by ICP-OES. As Table S2 shows, the composition of all powders is nearly identical ($Ce_{0.21}Zr_{0.63}Y_{0.14}La_{0.03}O_{2-\delta}$) and in agreement with the targeted composition of ($Ce_{0.18}Zr_{0.64}Y_{0.15}La_{0.03}O_{2-\delta}$) showing only minor deviations. The only exception is the powder, where aftertreatment was performed under acidic conditions. Only traces of the dopants Yttrium and Lanthanum could be detected, supporting the observed phase transformation, as these two elements stabilize the cubic structure. These findings indicate that, unlike basic aftertreatment, acidic hydrothermal aftertreatment is not suitable for tuning mesoporosity of such materials.

Characterization of Mesoporosity

To study the influence of the hydrothermal aftertreatment conditions and subsequent aging on the mesopore space, Ar-physisorption measurements were conducted. Argon was chosen as adsorptive, to prevent errors due to possible changes in surface functionalization, caused by pH variation. In contrast to Nitrogen, Argon does not possess a quadrupole moment, which could result in a preferential orientation on the adsorbent surface, hence, possibly causing non-structure-related differences in specific surface areas and micropore characterization.[33] The resulting Ar-physisorption isotherms are depicted in Figure 1a and d, along with the corresponding PSDs derived *via* NLDFT-analysis (Figure 1b, c and e, f).

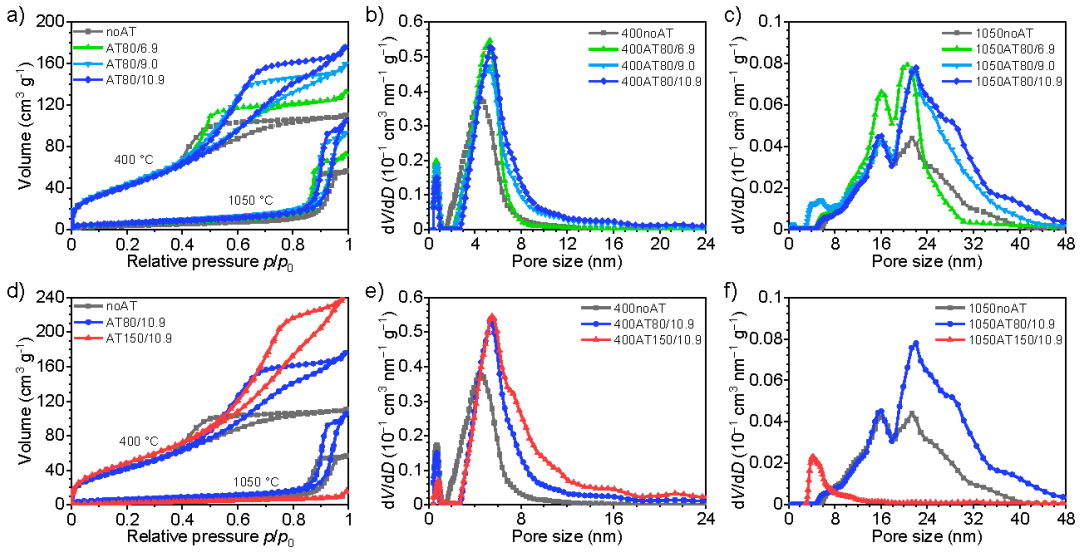

Figure 1. (a) Ar-physisorption isotherms (87 K) of the materials subjected to the aftertreatment at 80 °C and the corresponding pore size distributions after (b) calcination at 400 °C and (c) aging at 1050 °C. (d) Comparison of Ar-isotherms (87 K) and (e-f) pore size distributions of the materials subjected to aftertreatment in aqueous ammonia solution at pH 10.9 at different temperatures. The corresponding data for the samples AT80/−0.2 and AT80/11.3 is shown in Figure S3.

All isotherms classify as Type IV isotherms of the IUPAC classification[34], featuring pronounced hysteresis behavior, indicating their mesoporous nature. However, the type of hysteresis loop differs according to the thermal treatment of the samples. After calcination at 400 °C the isotherms feature a type H2 hysteresis loop, hinting at the occurrence of network effects such as cavitation – the formation of a gas bubble in the pore cavity, due to very small necks in comparison to the pore diameter – or pore-blocking/network percolation. After aging at 1050 °C the isotherms feature a type H1 hysteresis loop, which is typically encountered in materials with uniformly sized and shaped mesopores, featuring no network effects. This change in hysteresis type is observed for all samples but one, namely the sample treated in aqueous ammonia solution at 150 °C, which becomes completely nonporous upon aging (Figure 1d). Besides the thermal treatment of the powders, Figure 1 also visualizes the differences caused by posttreatment conditions. An increase in pH of the aftertreatment solution (Figure 1a-c; conducted at 80 °C) causes a significant increase in pore volume from 0.14 $cm^3 g^{-1}$ to up to 0.21 $cm^3 g^{-1}$ (Table 1), while the BET-area remains constant within the range of uncertainty of the measurement at ca. 150 $m^2 g^{-1}$. The observed increase in mesopore volume is caused by the increase in size of the mesopores, evidenced by the shift of the PSDs to larger diameters. While the shift of the PSDs' mode value from 4.3 nm to

5.3 nm, compared to the untreated material, is similar for all investigated pH values, individual sections of the PSDs change differently. Most notable are the changes in the ranges 2–4 nm and 6–18 nm. The former range represents the fraction of small mesopores, which diminishes with increasing pH values. The latter range represents newly formed, large mesopores, responsible for the significant increase in pore volume. Interestingly, posttreatment performed in demineralized water at pH 6.9 does not affect pore sizes beyond 7 nm, resulting in a sharpening of the PSD. In contrast, treatment at high pH results in a broadening of the pore size distribution, with the magnitude of the effect being pH-dependent. Upon aging at 1050 °C (Figure 1c), the mesopores undergo considerable growth, increasing the mean pore size to 20–30 nm. This growth is accompanied by a loss in BET-area as well as pore volume, as shown in Table 1. These losses, however, are smaller for the materials treated at higher pH, which retain about 60% of their pore volume. When performed at 150 °C, the post treatment at pH 10.9 yields a thermally instable material. Despite a drastic increase in pore volume to 0.29 $cm^3\ g^{-1}$ and an increased BET-area of 173 $m^2\ g^{-1}$ after calcination at 400 °C, the material becomes nearly non-porous upon aging at 1050 °C with a residual pore volume of 0.01 $cm^3\ g^{-1}$ and a BET-area of 10 $m^2\ g^{-1}$.

Table 1. Tabular Summary of Mesopore Characteristics.

XXXAT80/YY	400 °C			1050 °C			
pH	V_{Pore} ($cm^3\ g^{-1}$)	S_{BET} ($m^2\ g^{-1}$)	D_{NLDFT} (nm)	V_{Pore} ($cm^3\ g^{-1}$)	S_{BET} ($m^2\ g^{-1}$)	D_{NLDFT} (nm)	$\frac{V_{Pore,1050\,°C}}{V_{Pore,400\,°C}}$
-	0.14	150	5.0	0.07	13	21.4	0.52
-0.2	0.13	123	5.0	0.01	5	12.6	0.08
6.9	0.16	149	5.6	0.09	17	19.0	0.55
9.0	0.19	155	7.1	0.12	23	23.8	0.61
10.9	0.21	145	7.8	0.12	20	24.2	0.58
11.3	0.21	145	8.1	0.13	19	25.2	0.59
XXXAT150/YY	400 °C			1050 °C			
	0.294	173	9.8	0.01	10	12.4	0.04

A comparison of the adsorption-based PSDs of the materials treated at pH 10.9 but at different aftertreatment temperatures (80 °C *vs.* 150 °C, Figure 1e) illustrates the impact of treatment temperature on the pore sizes. While the range of 2–4 nm is similar in both materials, the region beyond 6 nm shows a significant increase in the fraction of large pores. Another difference was

found in the fraction of micropores (<2 nm), which at 80 °C only decreased slightly with increasing pH but diminished drastically at 150 °C (cf. Figure 1b and e) A comparison of adsorption- and desorption-based PSDs was performed to further analyze the mesoporous networks. If the calculated PSDs are superimposed, evaporation from the mesopore network can commence unhindered. The presence of network effects that impede evaporation, however, result in a shift of the desorption isotherm to smaller relative pressures and hence a shift (or skewing) of the desorption-based PSDs to smaller pore sizes in comparison to the adsorption-based PSD.[35] The corresponding comparison is shown in Figure 2. The desorption-based PSDs of the samples 400noAT and 400AT80/6.9 are much sharper in shape and maxima are shifted slightly to smaller pore sizes than in the corresponding adsorption-based PSDs. This observation suggests severe hindrance in the evaporation from pores, and hence impeded pore accessibility. In contrast, the desorption-based PSDs of the samples post treated in aqueous ammonia solution indicate a widening of mesopore necks and improvement of pore accessibility with increasing pH. Upon aftertreatment they become similar in shape to the adsorption-based PSDs, even shifting their maxima to larger values beyond the maxima of the adsorption-based PSDs. Such observation could be interpreted as adsorption following the so-called "initiated condensation" mechanism, which manifests in a shift of the maximum in the desorption-based PSDs to larger pore sizes. The origin of this shift is a mismatch of the assumed connectivity of pores in the applied adsorption-kernels, which describe adsorption in open and independent cylindrical pores, but do not account for three-dimensional connectivity present in the investigated materials. In fact, the mismatch between the adsorption- and desorption-based PSDs is a shift of the adsorption-based PSD to smaller pore sizes, due to the delay in condensation being smaller than modelled by the applied adsorption NLDFT-kernel that hence underestimates pore sizes, as demonstrated and explained for the first time by Kleitz et al. in KIT-6 materials.[36] Hence, its presence is a hint at a well-connected mesopore network. In this instance however, the observed shift is caused by hinderance during desorption, which is still present in all samples, even in those with additional hydrothermal aftertreatment. This can be seen in the difference in contribution to the adsorption- and desorption-based PSDs at large pore sizes, which is a typical symptom of hindered desorption (i.e., pore blocking or cavitation). Due to smaller restricting necks, pore evaporation is delayed until the relative pressure p/p_0 is reached, where evaporation from the necks commences. This, however, results in an overrepresentation in the volume fraction of pores corresponding to the average neck size, as the adsorbate inside the larger, hindered pores is attributed to the average neck size. The issue is illustrated in Figure 2c and Figure S4. Despite this, the observed increase in neck sizes still represents an improvement in pore accessibility, as the following discussion of the hysteresis scanning experiments demonstrates.

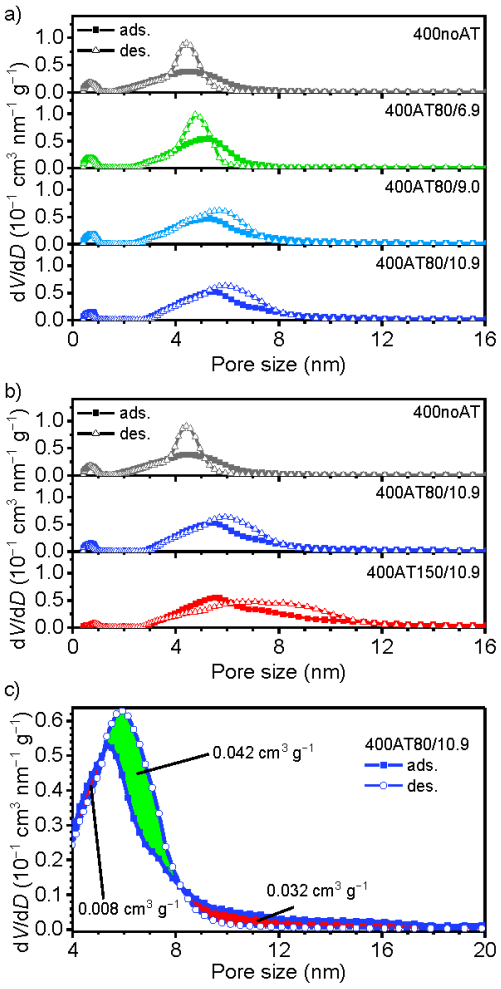

Figure 2. Comparison of adsorption and desorption-based differential PSDs of the samples calcined at 400 °C with the aftertreatment performed at (a) 80 °C with a variation of pH and (b) pH 10.9 at different temperatures. (c) Magnified section of the comparison of adsorption and desorption-based PSDs, illustrating the shift of the maximum in the desorption-based PSD due to pore-blocking of large pores.

Desorption hysteresis scanning is a powerful physisorption technique to analyze the connectivity of mesoporous networks.[14–16] It allows to derive the mechanisms involved in pore evaporation and, hence, to draw conclusions about the connectivity and accessibility of mesopores. To measure a set of desorption scanning isotherms, multiple adsorption and desorption cycles are performed. In each cycle, the pore networks are filled partially to a different degree, e.g., by subsequently lowering the starting p/p_0 each time, starting desorption from the partially filled pore network. The shape of the resulting isotherms is characteristic of the underlying desorption mechanism, which depends on pore connectivity. Ar-desorption scanning isotherms (T = 87 K) of the materials subjected to hydrothermal aftertreatment at different pH and temperatures are compared in Figure 3a. Their observed behavior supports the conclusions drawn from the comparison of adsorption and desorption-based PSDs shown in Figure 2.

The untreated material (400noAT) features scanning isotherms, which directly cross the hysteresis loop and meet the boundary isotherm in a sharp bend. For hysteresis loops of type H2, this is commonly observed if cavitation is the desorption mechanism. In contrast to that, the scanning isotherms of the hydrothermally treated materials merge smoothly into the boundary isotherm, due to the widened necks. This behavior is commonly observed for pore blocking or network percolation, where the difference between the pore cavity and necks is smaller than in the case

of cavitation, resulting in less hinderance during evaporation from the pores. We had demonstrated before that such hydrothermal aftertreatment in aqueous ammonia solution alleviates cavitation occurring in such pore networks.[19] In this instance, however, a direct comparison of the desorption scanning isotherms, to determine the magnitude of the pH and temperature influence, is difficult, due to the changes in shape of the hysteresis loop and relative pressure range, where hysteresis occurs.

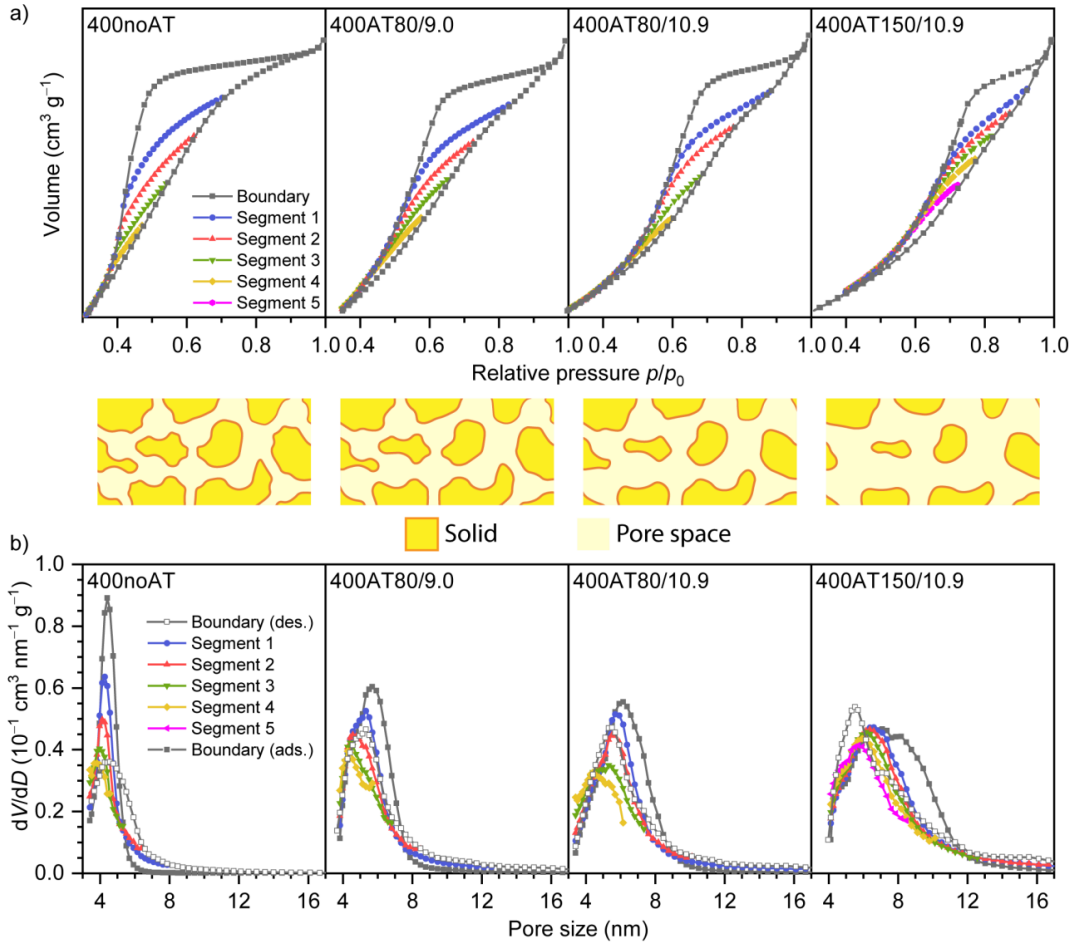

Figure 3. (a) Ar-physisorption desorption scans (T = 87 K) and schematic sketches of the alterations in the mesopore space of selected samples, illustrating the pH and temperature dependence of mesopore connectivity. The hysteresis loops are stretched vertically to facilitate visual comparison of the shape of the desorption branches. (b) Comparison of the desorption-based PSDs (filled) against the adsorption-based PSD (hollow) obtained from the hysteresis scanning and boundary isotherms *via* NLDFT-analysis.

To facilitate a comparison between the samples, the desorption-based PSDs of the scanning isotherms were calculated and compared to the adsorption-based PSD obtained from the boundary isotherm, shown in Figure 3b. This comparison demonstrates that even after hydrothermal aftertreatment larger pores show hindrance during desorption. However, this effect diminishes with increasing aftertreatment pH or temperature, supporting the conclusions drawn above. This can be seen in the PSDs from the first desorption scanning segments, which at larger pore sizes show significantly smaller fractions of large pores than the adsorption-based PSD of the boundary isotherm. These segments correspond to a partially filled pore system, where pores that are larger than the average pore size are filled before desorption. These pores are embedded within the main pore network and accessible only through smaller necks of average pore size and therefore suffer from pore blocking. This is also supported by the 3D-reconstructions obtained from electron tomography (Figure 4), which are discussed in detail below. Subsequent desorption isotherms correspond to the evaporation from the main pore network, comprised of pores of average pore size, resulting in evaporation *via* a network percolation mechanism. The corresponding calculated PSDs are initially similar to the adsorption-based PSD and then feature a smaller differential pore volume over the entire range.

In combination, these alterations suggest an Ostwald-Ripening-like dissolution and reprecipitation-based mechanism, which is supported by the observed influence of treatment conditions, leading to a more pronounced effect at higher pH and temperature. In particular, the pH mainly affects the solubility of the primary particles, and an increased temperature causes a severe acceleration of the dissolution and reprecipitation process. These findings are in good agreement with literature, discussing similarly treated materials.[20–22] The investigations further demonstrate that basic aftertreatment conditions are crucial for tuning pore sizes and thermal stability, as aftertreatment under neutral conditions results only in little improvement of thermal stability and a small increase in pore sizes, while also destroying the spherical secondary structure of the material (cf. Figure S1). Acidic aftertreatment not only does not allow tailoring pore sizes, but it also results in a thermally less stable material, destruction of the secondary structure, and a change in chemical composition. Further influences of the aftertreatment pH concerning surface chemical alterations and their influence on the thermal stability will be discussed in the section addressing the role of surface-bound nitrate groups.

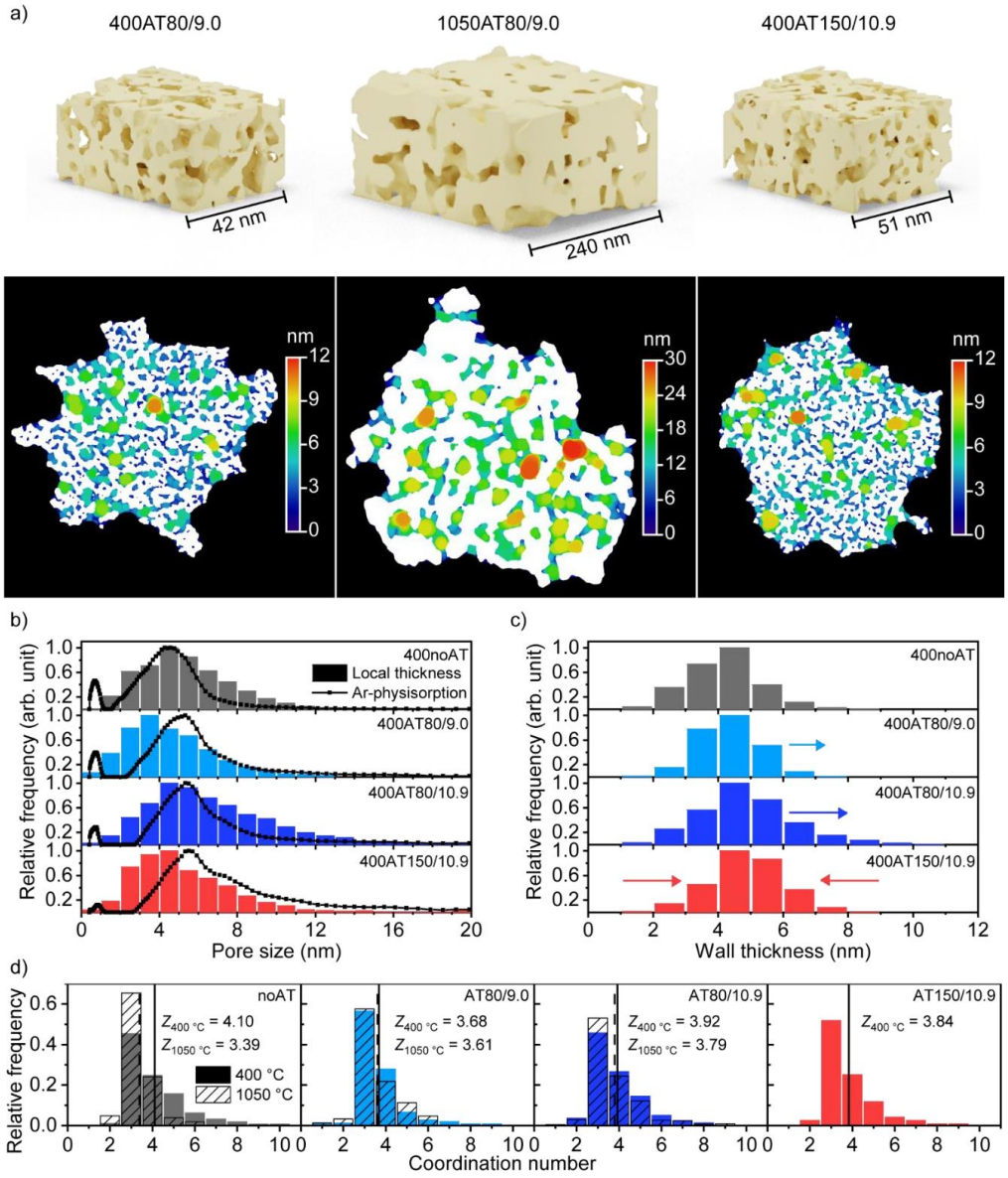

Figure 4. (a) Sections from the 3D-reconstructions obtained from electron tomography of the materials subjected to different hydrothermal aftertreatment conditions. The reconstruction of the sample aged at 1050 °C is depicted larger, to emphasize the difference in length scales to the samples calcined at 400 °C. (b) Comparison of adsorption-based PSDs from Ar-physisorption (NLDFT, T = 87 K) and PSDs obtained via local thickness analysis[29] performed on the 3D-reconstructions. (c) Wall thicknesses obtained *via* local thickness analysis of the solid phase. (d) Skeletonization-based pore coordination numbers according to the method described by Cheng et al.[30]

In order to complement the detailed physisorption analysis, electron tomography was conducted on selected samples. This method generates a three-dimensional (3D) representation of the material at the nanoscale by reconstructing an image stack from a series of scanning transmission electron microscopy (STEM) images taken at different projection angles.[37,38] The obtained 3D reconstruction provides information on the size of the pores and walls, as well as comprehensive statistical data on the connectivity of pores.[17,19,39] In particular, the samples 400AT80/9.0, 1050AT80/9.0, and 400AT150/10.9 were investigated, which bridge the gap in our recently published data[19] and allow for a discussion of the influence of aftertreatment temperature and pH. As the sample 1050AT150/10.9 is nearly non-porous, no electron tomography was performed for this sample. Figure 4a shows sections of the obtained 3D reconstructions and 2D slices of the full particles which are the basis for the quantitative analysis of the mesopore space by electron tomography. The shown sections prove the presence of a continuous, three-dimensional mesopore network, supporting the qualitative conclusions drawn from physisorption analysis. Aging at 1050 °C causes a severe coarsening of the mesopore skeleton and growth of mesopores, agreeing with the physisorption analysis as well. The 2D slices of the full particles reveal the presence of pores larger than the average pore size, embedded within the mesoporous structure. These support the above discussion of the hysteresis scans, as they represent the large pores that are hindered in desorption with their evaporation heavily depending on the surrounding mesopore network. Figure 4b shows the comparison of PSDs obtained from Ar-physisorption and local thickness analysis[29] of the samples after calcination. Both methods are generally in agreement, however, the local thickness histograms of the samples 400AT80/9.0 and 400AT150/10.9 are slightly shifted to smaller pore sizes by ca. 1 nm, which is why the pore sizes apparently do not confirm the trend observed in the physisorption and SAXS data. Logical explanations could be that the applied NLDFT-kernel is not suited to accurately describe the pore space or that the particles chosen during acquisition of the tilt series are not representative for the bulk materials. Concerning the first proposed explanation, the assumption of a cylindrical pore geometry could simply be false and hence dramatically affecting the PSDs. For example, the aftertreatment could gradually alter the morphology in dependence of the pH, from a worm-like cylindrical pore shape towards a more spherical shape. However, the observed trend of pore growth can also be extracted directly from the raw isotherms depicted in Figure 1, which clearly show a successive shift of the hysteresis loops to higher relative pressures. This trend is also reflected in the PSDs calculated by NLDFT. Additionally, the following discussion of the small angle X-ray scattering (SAXS) data supports the trend witnessed by the physisorption analysis. In a following section, we also address the question whether particles chosen during acquisition of the

STEM tilt series are representative for the bulk material by calculating SAXS curves from the 3D-reconstructions. These simulated curves suggest that the reconstructions indeed are generally representative for the bulk material, however, a subtle shift of the simulated SAXS curves of the samples 400noAT and 400AT80/10.9 to smaller scattering values was found (cf. Figure 6). This shift is consistent with the relative shift of the tompgraphy-based pore sizes in comparison to the samples 400AT80/9.0 and 400AT150/10.9. Concluding from that, the observed shift between the PSDs from electron tomography and physisorption is likely caused by the underlying assumptions on the pore geometry in the applied physisorption kernel.

Analogously to the analysis of the pore space, the local thickness approach can be used to calculate a wall size distribution (Figure 4c), inaccessible by physisorption analysis. The calculated wall size distributions indicate an increase of the mean wall size by up to 0.7 nm from 4.2 nm to 4.9 nm with an increasing pH and a sharpening of the wall size distribution with increasing temperature. In combination with the increase in mesopore sizes, this provides a rationale for the observed thermal stability of the differently treated materials: Hydrothermal aftertreatment at 150 °C results in a significant change in the ratio of the sizes of mesopores and walls. Comparably thin walls and large mesopores, yield a mechanically less stable material.

Besides pore size analysis, the 3D-reconstructions are a powerful tool to analyze pore connectivity by a skeletonization approach. In essence, the phase to be analyzed is thinned to its center line, yielding a topological representation of the mesopore (or solid) space. By counting the number of branches that meet in nodes and meticulously joining nodes belonging to the same pore, the coordination numbers of each pore can be determined, and the mean coordination number Z can be calculated according to eq. (1. The resulting histograms of the skeletonization analysis and Z-values are shown in Figure 4d. The comparison of Z before and after aging at 1050 °C shows a significant decrease of Z in the untreated sample (noAT), while in the samples AT80/9.0 and AT80/10.9 Z remains nearly constant. This further confirms that an increased pH during hydrothermal aftertreatment renders the materials thermally more stable than the untreated counterpart and therefore helps to maintain high connectivity even at high temperatures. Furthermore, this data proves that the pore network is continuously highly interconnected, confirming the conclusions drawn from hysteresis scanning.

SAXS was employed as an alternative and independent method of characterization, to validate the findings from both Ar-physisorption and electron tomography and to further investigate the observed differences. Figure 5 shows double-logarithmic plots of the SAXS curves of the materials calcined at 400 °C (a) and the materials after aging at 1050 °C (b).

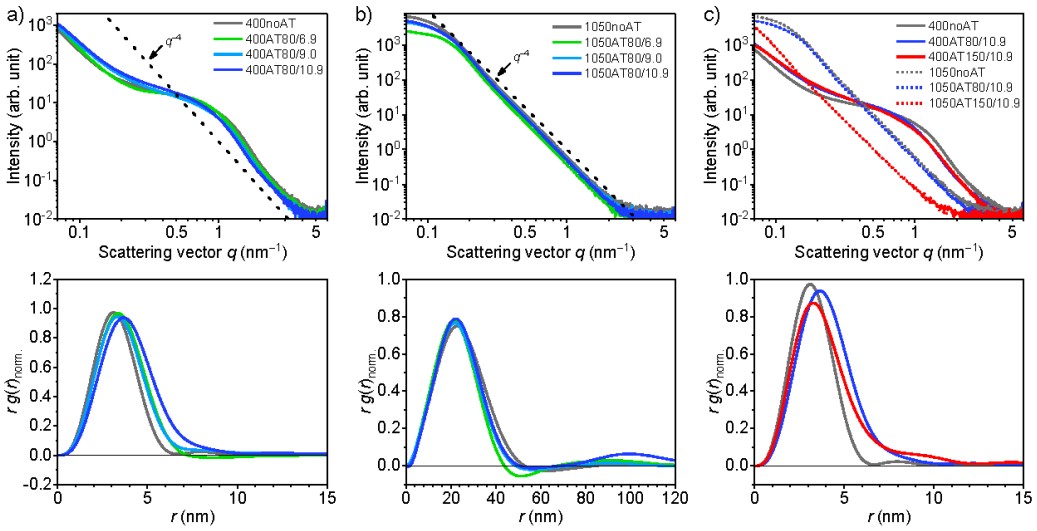

Figure 5. SAXS curves and calculated chord-length-distributions (CLDs) of the samples subjected to aftertreatment at different pH at 80 °C after calcination at 400 °C (a) and aging at 1050 °C (b). The CLDs of the aged samples feature a second maximum at 90–100 nm. This maximum, however, is a fitting artifact, which is caused by the extrapolation at small scattering vectors, due to a finite measurement range. Nevertheless, the CLD below 40 nm is not affected by this artifact. Using appropriate fitting parameters to suppress this artifact, the corresponding l_p values may be calculated over the range of 0–80 nm. (c) SAXS curves and CLDs for the samples subjected to aftertreatment at pH 10.9 at 150 °C. Since the aged sample treated at 150 °C becomes nearly non-porous, no suitable CLD could be calculated. Hence, the CLD plot only contains the data of the samples calcined at 400 °C. The corresponding data for the samples AT80/−0.2 and AT80/11.3 are shown in Figure S4.

None of the curves features Bragg reflections, which is a strong indicator for the disordered nature of the mesopore space. As Figure 5a depicts, already the calcined powders show a pH dependent shift of the inflection points of the SAXS curves from q = 1.4 nm^{-1} to q = 1.1 nm^{-1}, which corresponds to a size of the scattering features of 4.5 nm and 5.7 nm in real space. In the present case this can be interpreted as an increase in the mean mesopore size by ca. 1.2 nm, which agrees well with the findings from physisorption analysis (cf. Figure 1). Adhering to Porod's law, which describes the decay of the scattering intensity at large q, where the local surface roughness dominates, the scattering intensity becomes proportional to q^{-4} at large scattering vectors of $q >$ 1.8 nm^{-1}. The same is true for the SAXS curves of the powders aged at 1050 °C (Figure 5b), which follow Porod's law over a very broad range ($q >$ 0.3 nm^{-1}). Compared to the calcined materials the inflection points are shifted to small scattering vectors (0.1 nm^{-1} < q < 0.2 nm^{-1}). In real space

this translates to a significant growth of mesopores with a size of scattering features between 30 to 60 nm (cf. eq (2)).

$$d = \frac{2\pi}{q} \qquad (2)$$

A powerful tool for the SAXS-based quantitative analysis of disordered mesoporous materials is the chord-length-distribution (CLD) analysis, as it is applicable to any two-phase system (here: solid and void) and – in contrast to the NLDFT-based mesopore size analysis requires no assumptions on the underlying mesopore geometry. The CLD is described by $g(r)$ the relative frequency of surface-to-surface distances as a function of the chord length. Once obtained, it allows for the calculation of descriptive parameters of the mesopore space such as average pore and wall thicknesses (denoted l_v and l_w) and the surface area per scattering volume. The calculated CLDs are shown in Figure 5. The positions of the first maxima generally reflect the observations from the physisorption analysis very well and roughly correspond to the dimensions of mesopores or walls. The following minima and maxima likely arise from chords that penetrate more than one surface, i.e., spanning across a pore plus the subsequent wall. Furthermore, the CLD calculated from SAXS data does not distinguish chords belonging to the void or the solid phase. This becomes especially evident in the sample 400/1050AT80/−0.2, which is shifted to much higher r than expected from the physisorption analysis, where the smallest increase in mesopore size of all samples was determined. This observation can be explained by the dense nature of the material, possessing thick walls and therefore long chords, causing the severe tailing of the CLD, observed for the sample 1050AT80/−0.2.

To disentangle the mesopore and wall dimensions, the average chord length l_p (Porod-length) may be calculated as the first statistical moment of $g(r)$ according to eq (3:

$$l_p = \int_0^\infty r \cdot g(r)\, dr \qquad (3)$$

The relationship of l_p to l_v and l_w is shown in eq (4 and requires the knowledge of the mesopore volume fraction φ_v, which can be calculated according to eq (5) from the mesopore volume obtained from physisorption analysis and the skeleton-density obtained from He-pycnometry. An average value of $\rho_{Skel.} = 4.8$ g cm^{-3} determined from three samples was used for all calculations.

$$l_p = l_W \varphi_V = l_V(1 - \varphi_V) \qquad (4)$$

$$\varphi_V = \frac{V_V}{V_W + V_V} \text{ with } V_W = \frac{1}{\rho} \qquad (5)$$

As micro- and macroporosity are not included within the measured q-range, only the mesopore volume is relevant to this analysis. The calculated mesopore and wall dimensions are presented in Table 2 along with the mesopore size obtained from Ar-physisorption analysis. The results of both methods agree well in case of the materials calcined at 400 °C. However, the samples treated at an elevated pH show a deviation towards larger mesopore dimensions. This observation can be

explained by the cylindrical nature of the mesopores, demonstrated by the tomographic reconstructions investigated in a recent publication[19] and the observed improvement of pore accessibility evidenced by Ar-physisorption (cf. Figure 2), which contributes to a lengthening of chords. Also, whilst the NLDFT-based approach determines the diameter of a theoretical cylindrical pore with infinite length, which fills at a given relative pressure, the calculated l_v represents the average chord length of chords within the void phase. As for cylindrical pores, these can also be oriented along instead of across the pores, causing asymmetry in the CLD. Hence, the average chord length of the void phase l_v does not necessarily correspond to the pore diameter.

For the samples aged at 1050 °C, although being in the same order of magnitude, the comparison reveals larger differences between the NLDFT-based approach and the CLD approach. The general trend that mesopore sizes increase with increasing pH during posttreatment, however, is still reflected within the data obtained for l_v.

Besides the average mesopore size l_v, the average wall size l_w is a crucial property of the mesoporosity, as it critically influences a materials mechanical strength and the length of intra-particular diffusion pathways. This could for example heavily influence oxygen diffusion within the solid phase of the oxygen storage catalyst, a decisive factor for the speed at which oxygen can be released from or incorporated into the crystal lattice. For the samples calcined at 400 °C, the wall sizes of all samples are quite similar ranging from 5.6 nm to 7.1 nm, supporting the observations from XRD, which show that the crystallite size is unaffected by the posttreatment. The only exception to this is the sample post treated in an aqueous solution of nitric acid (400AT80/−0.2), which possesses a wall thickness of 8.5 nm. During aging at 1050 °C, the wall sizes of the materials, like the mesopore sizes, generally increase. However, considerable differences were detected between the samples. Overall, the increase in average wall size is smaller for the materials treated under basic conditions (pH > 9) than for the material treated at pH 6.9 or the untreated material, which in turn signifies an improved thermal stability of these materials. In contrast to that, the sample 400AT80/−0.2 shows a drastic increase in l_w to 390.8 nm, being in agreement with the severe loss of porosity observed by physisorption analysis and SEM. Aside the comparison of average mesopore and wall dimensions, the volume fraction φ_v also proves the improved thermal stability of the materials treated under basic conditions (cf. Table 2).

Table 2. Comparison of Textural Properties Obtained from Ar-physisorption and CLD Analysis.

XXXAT80/YY	400 °C					1050 °C				
pH	l_p (nm)	φ_V	l_V (nm)	l_W (nm)	D_{NLDFT} (nm)	l_p (nm)	φ_V	l_V (nm)	l_w (nm)	D_{NLDFT} (nm)
-	2.83	0.40	4.7	7.1	5.0	19.04	0.26	25.6	74.4	21.4
−0.2	3.27	0.39	5.3	8.5	5.0	18.04	0.05	18.9	390.8	12.6
6.9	3.01	0.43	5.3	6.9	5.6	17.40	0.30	24.7	58.7	19.0
9.0	3.13	0.48	6.0	6.5	7.1	18.01	0.36	28.2	49.8	23.8
10.9	3.45	0.51	7.0	6.8	7.8	19.04	0.37	30.4	51.0	24.2
11.3	3.36	0.51	6.8	6.6	8.1	19.95	0.38	32.1	52.7	25.2
XXXAT150/YY	400 °C					1050 °C				
10.9	3.29	0.59	8.0	5.6	9.8	n.a.	n.a.	n.a.	n.a.	12.4

As the 3D-reconstructions obtained from electron tomography provide only a very localized insight into the mesopore space, the question may arise, whether the chosen particle represents the bulk of the material. While, as demonstrated above, the agreement of pore sizes determined by Ar-physisorption and electron tomography analysis is decent, the NLDFT-analysis is based on critical assumptions about the geometry of the pores. Experimentally obtained SAXS curves, in turn, are free from such assumptions and can provide valuable additional proof, whether the particles chosen for reconstruction are representative for the bulk of the material. Hence, a method for direct comparison is desirable.

To calculate scattering curves from the 3D-reconstructions the relationship of $I(\mathbf{q})$ to the scattering density $\rho(\mathbf{x})$, shown in eq (6), is essential. It states that $I(\mathbf{q})$ is the absolute square of the Fourier Transform of the scattering density. The experimentally accessible scattering intensity $I(q)$ is the result of orientational averaging of $I(\mathbf{q})$ (with $q = |\mathbf{q}|$).

$$I(\mathbf{q}) = |\mathcal{F}[\rho(\mathbf{x})]|^2 \qquad (6)$$

By treating the voxel values in the 3D-data of the tomographic reconstructions as the scattering density $\rho(\mathbf{x})$, the scattering intensity $I(q)$ can be calculated according to the method described by Schmidt-Rohr.[31] In particular, Fast Fourier Transform (FFT) of the 3D image stack yields the 3D discrete Fourier Transform, which – following Schmidt-Rohr – is converted into a continuous

density distribution by multiplication with a sinc function (sinus cardinalis) as shown in eq (7.

$$I(\mathbf{q}) = |\mathcal{F}[\rho(\mathbf{x})]|^2 \cdot \left\{ \prod_n^m \frac{\sin x_n}{x_n} \right\}^2 \qquad (7)$$

The 3D scattering intensity $I(\mathbf{q})$ is converted into a 1D scattering curve $I(q)$, by orientational averaging. This was achieved by scanning the 3D-grid of $I(\mathbf{q})$ and binning the intensity of each voxel into $I'(q)$. To obtain the final scattering curve, $I'(q)$ is divided by q^2, as the number of voxels in each spherical shell increases proportional to q^2. The q-range accessible by this procedure is directly related to the voxel size a and the width of the investigated volume of interest (VOI) in voxels, as eq (8) and (9) demonstrate.

$$q_{min} = \frac{2\pi}{Na} \text{ and } q_{max} = \frac{2\pi}{\frac{N}{2}a} = \frac{4\pi}{Na} \qquad (8)$$

$$\text{With} \quad N = width\ of\ \rho(x)\ in\ px \quad \text{and } a = pixel\ size\ in\ nm\ px^{-1} \qquad (9)$$

The calculated SAXS curves are shown in Figure 6 along with the measured SAXS curves. The shapes of the calculated SAXS curves agree well with the shapes of the measured curves, indicating that the investigated VOIs are generally representative for the bulk material. However, as noted above, subtle shifts of the calculated SAXS curves to smaller q-values are visible for the samples 400noAT and 400AT80/10.9 (Figure 6a). This results in an overestimation of the pore sizes determined from these reconstructions. Additionally, all reconstructions show a moderate deviation of the simulation from the measured SAXS curves at low angles. This is a result of the small number of sample points available in the discrete FFT at low angles, i.e., for the smallest possible q-value only six voxels exist.

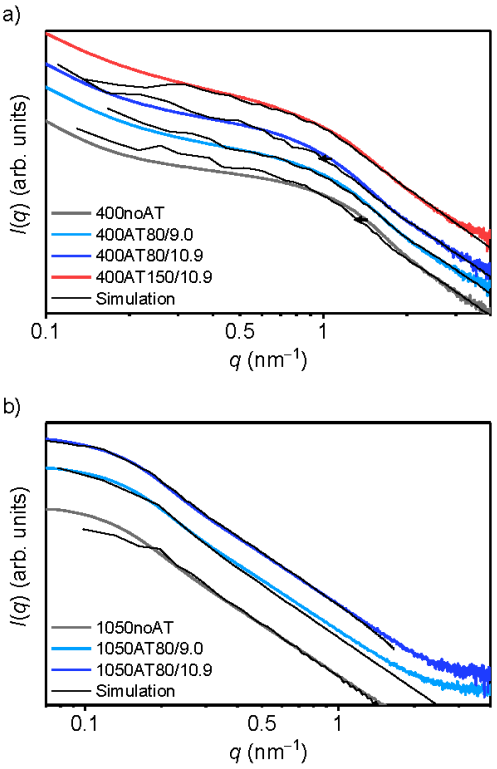

Figure 6. Measured SAXS curves and corresponding simulated SAXS curves calculated from the tomographic reconstructions after (a) calcination at 400 °C and (b) aging at 1050 °C. In (a) the simulated SAXS curves of the samples 400noAT and 400AT80/10.9 show a subtle shift in comparison to their corresponding measured SAXS curve.

To test the sensitivity of the simulated SAXS curves for small deviations in the reconstructions,

two procedures were applied to the reconstruction of the sample 400AT80/9.0. In the first test, the pixel size was varied around the original pixel size with a step size of 0.05 nm px^{-1}. This corresponds to a scaling of the reconstruction, which results in a horizontal scaling of the calculated SAXS curve that is perceived as a horizonal shift of the curve. To simulate the case where a particle with slightly larger or slightly smaller pores was selected that are not representative of the bulk material, a dilation and an erosion filter were applied to the reconstruction before calculating the SAXS curves. This adds or removes one or two pixels at the surface of the solid phase, effectively changing the pore size. The results of both tests are shown in Figure S5. Both variations result in noticeable deviation from the measured SAXS curve, and the curve calculated with the unmodified reconstruction and pixel size, indicating that the method is capable of detecting even small deviations between experimental and calculated SAXS curves. Hence, this procedure provides a quick and simple approach to compare SAXS curves and tomographic reconstructions, allowing to exclude the input data for further pore size characterization as the source of possible mismatch between methods, which could for example be caused by inadequate fitting of the SAXS curves.

Investigation of Calcination Processes

In a previous publication, we discussed the importance of surface bound nitrate groups in the calcination process.[18] By combining Ar-physisorption analysis and thermogravimetric analysis coupled with mass spectrometry (TG-MS), we demonstrated a similar stabilizing effect of the nitrate groups against sintering at temperatures below 600 °C as it was observed by Özkan et al. for pure ceria materials.[17] However, as illustrated by the analysis of the mesopore space above, the improvements in thermal stability gained by additional aftertreatment under basic conditions surpass the stabilization by the nitrate groups, although a removal of nitrate groups is to be expected under such conditions. This presumption is confirmed by the mass losses observed in the TG-MS analysis of the dried powders, depicted in Figure 7a. Generally, the mass loss may be divided into three sections. The first section ranges from the starting temperature (room temperature) to ca. 200 °C, which can be attributed to the removal of physisorbed water. In the second section, ranging from 200 °C to 600 °C, the decomposition of surface bound nitrate groups occurs. This is confirmed by the MS-intensities of different nitrogen oxide species, e.g., m/z = 30 (NO^+), which is depicted in Figure 7b. Besides these and water, no other relevant signals caused by decomposition products of other surface bound species could be detected. In this section, the differences in nitrate content are revealed. While the untreated material shows a mass loss of ca. 9%, the total mass losses of the powders subjected to aftertreatment decrease with an increasing pH and temperature during aftertreatment. After aftertreatment the materials treated at 80 °C and pH 9.0 and 10.9 both show a mass loss of 6%. Aftertreatment at 150 °C and pH 10.9 results in a mass loss of 5%.

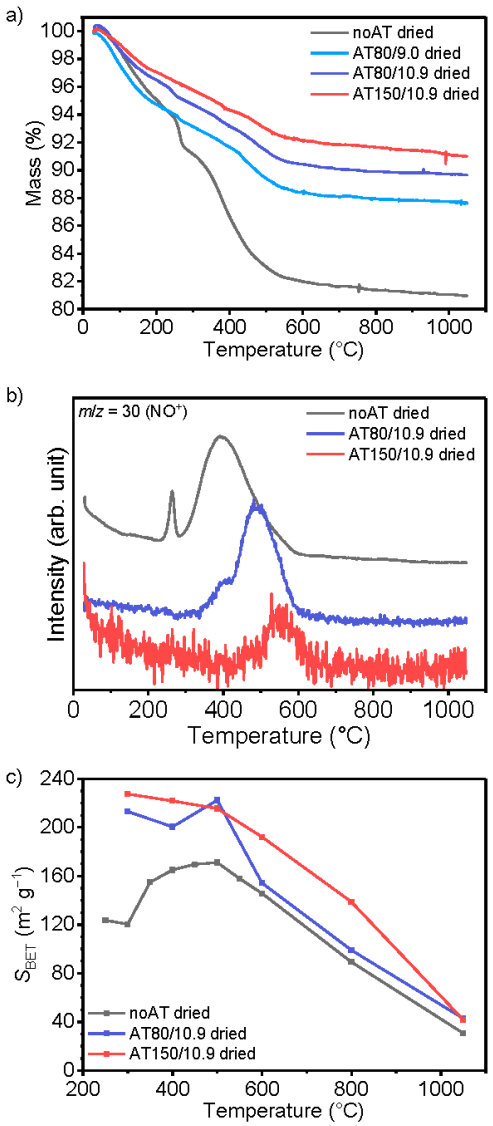

Figure 7. (a) Mass loss observed during TG-MS measurements performed on the dried powders before calcination, showing different nitrate contents after hydrothermal aftertreatment at different temperatures and (b) the corresponding MS-intensities of the NO^+ cation at m/z = 30. (c) Development of crystallite sizes during calcination of the dried powders.

To find a rationale for the low thermal stability of the material treated at 150 °C, the development of the pore space upon calcination of the dried powders was investigated in detail. Therefore, a set of Ar-physisorption isotherms (Figure S6) and SAXS curves (Figure 8 and Figure S8a) was recorded for samples heated to specific temperatures in the range of nitrate group removal. A full discussion on the influence of the nitrate groups on the untreated material was provided in a previous publication.[18] In essence, the removal of the nitrate groups initially generates new micropores until 500 °C is reached, seen in the increase in pore volume and BET-area. At this stage, the protecting layer, stabilizing the primary particles against sintering, is mostly removed and a decline in pore volume and BET-area is observed. This is accompanied by a significant growth of mesopores, as the calculated PSDs illustrate (Figure S8c). In comparison to that, the hydrothermally treated materials exhibit a different calcination behavior. Due to the reduced number of nitrate groups present after aftertreatment, in both cases, no new micropores are formed in the range of 300–600 °C, as the PSDs in Figure 8a and b reveal. Instead, a continuous loss of BET-area occurs (cf. Figure 7c) due to the immediate collapse of micropores and lack of additional stabilization in this phase. However, the dried materials with aftertreatment initially feature a much higher BET-area of 210–230 m^2 g^{-1} instead of ca. 120 m^2 g^{-1}. The SAXS curves, calculated CLDs, and PSDs depicted in Figure 8 demonstrate that in case of the material hydrothermally treated

at 80 °C, the growth of mesopores and loss of mesopore volume commences at 500 °C. In contrast to that, the material hydrothermally treated at 150 °C appears to be thermally more stable until 600 °C, as no growth of pores is observed. However, above 800 °C, the loss in mesopore volume takes place at a much faster rate and mesopores grow less until a temperature of 1050 °C is reached than in the material treated hydrothermally at 80 °C. We suspect that due to the more advanced condensation and crystallization of primary particles the mesopore skeleton is unable to rearrange fast enough to develop larger, thermally more stable mesopores. Hence, after prolonged aging at 1050 °C, almost no pores persist.

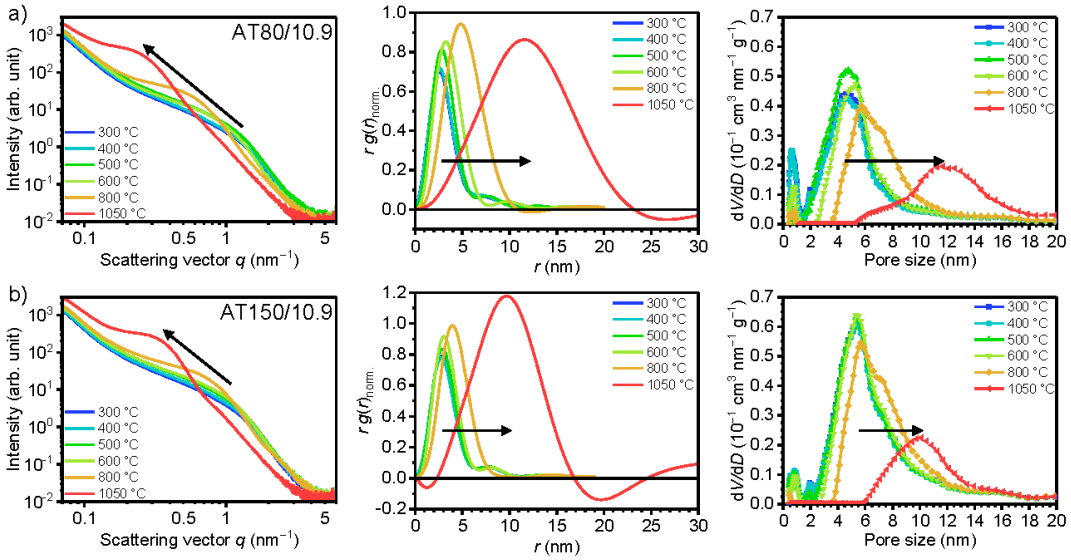

Figure 8. SAXS curves (left), calculated CLDs (center), and corresponding pore size distributions obtained from Ar-physisorption at $T = 87$ K (right) for different temperatures during calcination of the dried materials AT80/10.9 (a) and AT150/10.9 (b). The data for the sample without additional hydrothermal aftertreatment is shown in Figure S7. Due to a similar fitting artefact as seen in Figure 5, corresponding l_p, l_w, and l_v values (Tables S3–5 and Figure S9) were calculated over the range 0–20 nm for temperatures below 800 °C.

The combined observations from the various employed methods are illustrated schematically in Figure 9a for the different stages of synthesis and aging. The unmodified synthesis procedure (noAT) yields a mesopore skeleton that after completion of the nitrate removal is comprised of only lightly bound particles, featuring low mechanical resistance against the collapse of pores. In contrast to that, the hydrothermal aftertreatment removes a significant amount of surface-bound nitrate groups (cf. Figure 9b), presenting a gentler method of nitrate removal than

calcination. As outlined above, the aftertreatment furthermore causes significant structural changes to the mesopore network that can be described by classical Sol-Gel-processes, outlined schematically in Figure 9b.

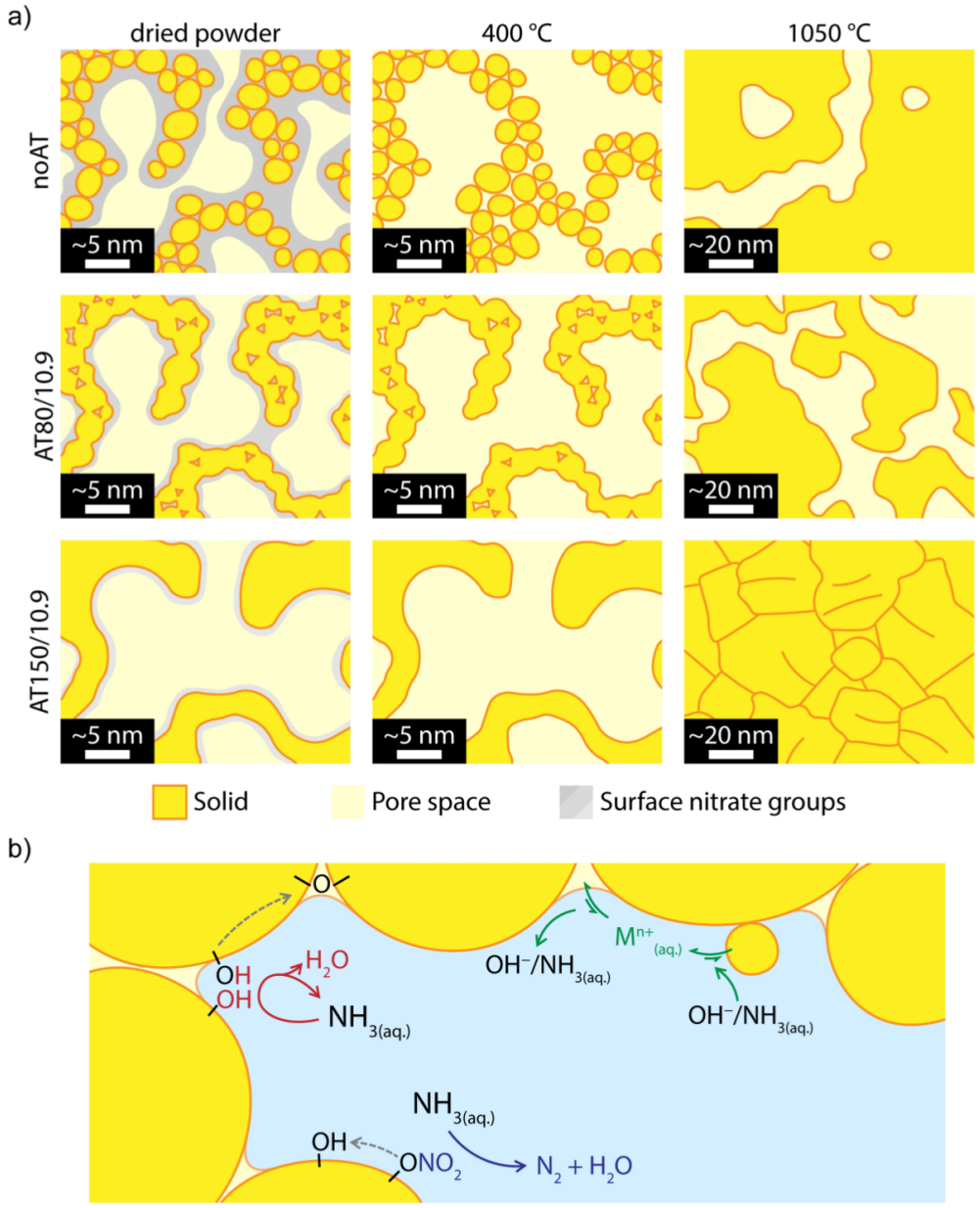

Figure 9. Schematic representation of (a) the materials' nanostructures at the different stages of synthesis and aging in dependence of aftertreatment conditions and (b) the chemical reactions occurring at the primary particle's surface during hydrothermal aftertreatment in aqueous ammonia solution.

These include a base-catalyzed condensation of inter and intra-particular hydroxyl groups (crystallization) as well as a coarsening of the skeletal structure by base-catalyzed dissolution and reprecipitation. Performed at 80 °C, the aftertreatment in aqueous ammonia solution causes the condensation of the primary particles at their surface and thickening of mesopore walls, forming a mechanically more stable skeleton structure that results in improved thermal stability (Figure 9a). This is accompanied by a growth of mesopores (increasing the mesopore volume) and improvement in pore connectivity due to the widening of pore necks. Upon aging at 1050 °C, the hydrothermally treated materials maintain a higher mesopore volume, due to the considerable growth of mesopores, and an improved connectivity. However, when performed at 150 °C instead of 80 °C, the hydrothermal aftertreatment leads to a thermally instable material. Although the material is thermally more stable at low temperatures, maintaining a high mesopore volume after calcination at 400 °C, even showing stability up to 800 °C (cf. Figure 8b), the material becomes nearly non-porous during prolonged aging. This is likely caused by a slower rate of mesopore growth during high temperature treatment due to the formation of a rigid mesopore skeleton with comparably thin walls for the newly formed large mesopores. This highly crystallized and rigid structure, however, is unable to rearrange and accommodate for the growth of pores, resulting in the collapse and concomitant sintering of the material.

Conclusions

In this study we present a detailed analysis of the effects of temperature and pH during hydrothermal aftertreatment of wet filter cakes of doped ceria-zirconia mixed oxides obtained via hydrothermal synthesis, focusing on chemical and structural changes. We demonstrate a pH dependent widening of mesopore necks by detailed Ar-physisorption analysis in combination with desorption hysteresis scanning, concluding that such aftertreatment significantly improves mesopore accessibility that can be tuned by choosing appropriate aftertreatment conditions. Electron tomography analysis, combined with suitable statistical analysis, was conducted in order to validate and complement the physisorption analysis, confirming the continuous 3D nature of the mesoporous networks. These are able to withstand high temperature aging, retaining improved connectivity if the materials were subjected to hydrothermal aftertreatment at higher pH. In search of a rationale for the materials' improved thermal stability, the solid phase of the material was studied in detail, based on the electron tomography reconstructions and SAXS. The data reveal an increase of wall thicknesses with an increase in aftertreatment pH. In analogy to classical Sol-Gel-processes, the alterations in the mesopore space suggest a dissolution and re-precipitation-based mechanism that advances the condensation of the primary particles, forming a stronger skeleton structure, while simultaneously widening the mesopore necks. Besides directly altering the mesopore structure, the hydrothermal

aftertreatment also represents a gentle alternative to calcination for the removal of surface-bound nitrate groups. While these were shown to prevent sintering of primary particles at low temperatures, the gain in thermal stability due to hydrothermal aftertreatment surpasses this effect significantly. We believe these concepts also apply to the synthesis of other nitrate-precursor-based metal oxides in order to improve their thermal stability and pore accessibility.

In the progress of the validation and comparison between physisorption and SAXS data and the reconstructions obtained *via* electron tomography we encountered discrepancies amongst the methods. A simple and obvious explanation of such discrepancy is the fact that with physisorption and SAXS analysis the bulk properties of the material are analyzed, while electron tomography provides the reconstruction of one particle, that may not be representative of the bulk material. In order to validate the representativeness of the tomographic reconstructions for the bulk material, we implemented a simple tool to simulate SAXS curves from the reconstructions, allowing for a direct comparison to the SAXS data.

The present study demonstrates the power of a detailed physisorption analysis to unravel even fine changes in the mesopore space, allowing to trace the impact of synthesis parameters. In particular, the importance of mesopore connectivity, a decisive factor in heterogeneous catalysis, needs to be stressed and should be paid more attention in the routine characterization of mesoporous materials for catalytic applications. Ideally this is achieved by performing hysteresis scanning experiments, in order to obtain pore size dependent information on the accessibility of mesopores, as demonstrated in this study. Although a quantification of connectivity from hysteresis scanning data is still a matter of ongoing research, it is already possible to derive valuable information on the mesopore network and desorption mechanisms found within. It is capable of probing the connectivity of different mesopore populations, allowing to paint a detailed picture of the investigated materials' mesopore structure. This indeed renders hysteresis scanning a promising tool for the routine analysis of mesopore networks.

ASSOCIATED CONTENT

Supporting Information

The data underlying this study are openly available in a Zenodo repository. DOI: 10.5281/zenodo.8054446. The following files are available free of charge.

Electron Tomography Tilt Ranges, Alignment Error, and Reconstruction Resolution; Elemental Compositions of the Synthesized Powders as Determined by ICP-OES; SEM images showing the spherical secondary structure of the synthesized powders; X-ray diffraction patterns of the synthesized powders; Ar-physisorption isotherms and corresponding adsorption-based pore size distributions of the sample treated under acidic conditions and the sample treated at pH 11.3; Differences between adsorption- and

desorption-based pore size distributions obtained via NLDFT-analysis of the Ar-physisorption isotherms; SAXS curves and calculated CLDs of the samples subjected to aftertreatment at different; Simulated scattering curves calculated from the electron tomography reconstruction of the sample 400AT80/9.0 with varying pixel sizes; Ar-physisorption isotherms of the samples heated to different temperatures during calcination of the dried materials; SAXS curves, calculated CLDs, and corresponding pore size distributions of the dried material without additional hydrothermal aftertreatment; Mean pore and wall sizes according to the CLD analysis of the SAXS data; Tabular Mean Pore and Wall Sizes Calculated from the CLD of the Dried Powders noAT, AT80/10.9, and AT150/10.9 (PDF)

AUTHOR INFORMATION

Corresponding Author

*(B.S.) E-mail: bernd.smarsly@phys.chemie.uni-giessen.de

Present Addresses

†If an author's address is different than the one given in the affiliation line, this information may be included here.

Author Contributions

The manuscript was written through contributions of all authors. All authors have given approval to the final version of the manuscript.

Funding Sources

Financial support was provided by Umicore AG & Co. KG.

Notes

Any additional relevant notes should be placed here.

ACKNOWLEDGMENT

The authors thank Heinz Amenitsch, Manfred Kriechbaum, Lysander Wagner, and Raoul Brand for the SAXS measurements. Funding through the DFG CRC 1441 TrackAct is gratefully acknowledged. Further acknowledgement goes to the Center of Materials Research (LaMa) at Justus-Liebig University Giessen for the support of this project. X. Huang acknowledges the China Scholarship Council (CSC) for the support of her PhD at Karlsruhe Institute of Technology & Technical University of Darmstadt.

REFERENCES

(1) Melchionna, M., Fornasiero, P. The role of ceria-based nanostructured materials in energy applications. *Mater. Today* **2014**, *17*, 349–357, DOI: 10.1016/j.mattod.2014.05.005.

(2) Montini, T., Melchionna, M., Monai, M., Fornasiero, P. Fundamentals and Catalytic Applications of CeO_2-Based Materials. *Chem. Rev.* **2016**, *116*, 5987–6041, DOI: 10.1021/acs.chemrev.5b00603.

(3) Sun, Y., Li, C., Djerdj, I., Khalid, O., Cop, P., Sann, J., Weber, T., Werner, S., Turke, K., Guo, Y., Smarsly, B. M., Over, H. Oxygen storage capacity versus catalytic activity of ceria–zirconia solid solutions in CO and HCl

oxidation. *Catal. Sci. Technol.* **2019**, *9*, 2163–2172, DOI: 10.1039/C9CY00222G.

(4) Cop, P., Maile, R., Sun, Y., Khalid, O., Djerdj, I., Esch, P., Heiles, S., Over, H., Smarsly, B. M. Impact of Aliovalent/Isovalent Ions (Gd, Zr, Pr, and Tb) on the Catalytic Stability of Mesoporous Ceria in the HCl Oxidation Reaction. *ACS Appl. Nano Mater.* **2020**, *3*, 7406–7419, DOI: 10.1021/acsanm.0c00994.

(5) Abanades, S., Haeussler, A., Julbe, A. Synthesis and thermochemical redox cycling of porous ceria microspheres for renewable fuels production from solar-aided water-splitting and CO_2 utilization. *Appl. Phys. Lett.* **2021**, *119*, 23902, DOI: 10.1063/5.0055282.

(6) Le Gal, A., Abanades, S. Dopant Incorporation in Ceria for Enhanced Water-Splitting Activity during Solar Thermochemical Hydrogen Generation. *J. Phys. Chem. C* **2012**, *116*, 13516–13523, DOI: 10.1021/jp302146c.

(7) Özkan, E., Cop, P., Benfer, F., Hofmann, A., Votsmeier, M., Guerra, J. M., Giar, M., Heiliger, C., Over, H., Smarsly, B. M. Rational Synthesis Concept for Cerium Oxide Nanoparticles: On the Impact of Particle Size on the Oxygen Storage Capacity. *J. Phys. Chem. C* **2020**, *124*, 8736–8748, DOI: 10.1021/acs.jpcc.0c00010.

(8) Ohtake, N., Katoh, M., Sugiyama, S. High thermal-stability ceria synthesized via thermal-hydrolysis route and methane-combustion performance. *J. Ceram. Soc. Japan* **2017**, *125*, 57–61, DOI: 10.2109/jcersj2.16255.

(9) Si, R., Zhang, Y.-W., Wang, L.-M., Li, S.-J., Lin, B.-X., Chu, W.-S., Wu, Z.-Y., Yan, C.-H. Enhanced Thermal Stability and Oxygen Storage Capacity for $Ce_xZr_{1-x}O_2$ (x = 0.4–0.6) Solid Solutions by Hydrothermally Homogenous Doping of Trivalent Rare Earths. *J. Phys. Chem. C* **2007**, *111*, 787–794, DOI: 10.1021/jp0630875.

(10) Friedrich, H., Jongh, P. E. de, Verkleij, A. J., Jong, K. P. de. Electron tomography for heterogeneous catalysts and related nanostructured materials. *Chem. Rev.* **2009**, *109*, 1613–1629, DOI: 10.1021/cr800434t.

(11) Ercius, P., Alaidi, O., Rames, M. J., Ren, G. Electron Tomography: A Three-Dimensional Analytic Tool for Hard and Soft Materials Research. *Adv. Mater.* **2015**, *27*, 5638–5663, DOI: 10.1002/adma.201501015.

(12) Reich, S.-J., Svidrytski, A., Höltzel, A., Wang, W., Kübel, C., Hlushkou, D., Tallarek, U. Transport under confinement: Hindrance factors for diffusion in core-shell and fully porous particles with different mesopore space morphologies. *Microporous Mesoporous Mater.* **2019**, *282*, 188–196, DOI: 10.1016/j.micromeso.2019.02.036.

(13) Tallarek, U., Hochstrasser, J., Ziegler, F., Huang, X., Kübel, C., Buchmeiser, M. R. Olefin Ring-closing Metathesis under Spatial Confinement: Morphology–Transport Relationships. *ChemCatChem* **2021**, *13*, 281–292, DOI: 10.1002/cctc.202001495.

(14) Cimino, R., Cychosz, K. A., Thommes, M., Neimark, A. V. Experimental and theoretical studies of scanning adsorption–desorption isotherms. *Colloids Surf., A* **2013**, *437*, 76–89, DOI: 10.1016/j.colsurfa.2013.03.025.

(15) Kenvin, J., Mitchell, S., Sterling, M., Warringham, R., Keller, T. C., Crivelli, P., Jagiello, J., Pérez-Ramírez, J. Quantifying the Complex Pore Architecture of Hierarchical Faujasite Zeolites and the Impact on Diffusion. *Adv. Funct. Mater.* **2016**, *26*, 5621–5630, DOI: 10.1002/adfm.201601748.

(16) Kube, S. A., Turke, K., Ellinghaus, R., Wallacher, D., Thommes, M., Smarsly, B. M. Pore Size Gradient Effect in Monolithic Silica Mesopore Networks Revealed by In-Situ SAXS Physisorption. *Langmuir* **2020**, *36*, 11996–12009, DOI: 10.1021/acs.langmuir.0c02183.

(17) Özkan, E., Hofmann, A., Votsmeier, M., Wang, W., Huang, X., Kübel, C., Badaczewski, F., Turke, K., Werner, S., Smarsly, B. M. Comprehensive Characterization of a Mesoporous Cerium Oxide Nanomaterial with High Surface Area and High Thermal Stability. *Langmuir* **2021**, *37*, 2563–2574, DOI: 10.1021/acs.langmuir.0c02747.

(18) Prates da Costa, E., Hofmann, A., Göbel, U., Cop, P., Smarsly, B. M. Development of Pore Morphology During Nitrate Group Removal by Calcination of Mesoporous $Ce_xZr_{1-x-y-z}Y_yLa_zO_{2-\delta}$ Powders. *Langmuir* **2022**, *38*, 8342–8352, DOI: 10.1021/acs.langmuir.2c00875.

(19) Prates da Costa, E., Huang, X., Kübel, C., Cheng, X., Schladitz, K., Hofmann, A., Göbel, U., Smarsly, B. M. Effects of Hydrothermal Treatment on Mesopore Structure and Connectivity in Doped Ceria-Zirconia Mixed Oxides. *Langmuir* **2022**, *39*, 177–191, DOI: 10.1021/acs.langmuir.2c02366.

(20) Chuah, G. K., Jaenicke, S., Pong, B. K. The Preparation of High-Surface-Area Zirconia. *J. Catal.* **1998**, *175*, 80–92, DOI: 10.1006/jcat.1998.1980.

(21) Di Monte, R., Kašpar, J., Bradshaw, H., Norman, C. A rationale for the development of thermally stable nanostructured CeO_2-ZrO_2-containing mixed oxides. *J. Rare Earths* **2008**, *26*, 136–140, DOI: 10.1016/S1002-0721(08)60053-8.

(22) Raju, V., Jaenicke, S., Chuah, G.-K. Effect of hydrothermal treatment and silica on thermal stability and oxygen storage capacity of ceria–zirconia. *Appl. Catal., B* **2009**, *91*, 92–100, DOI: 10.1016/j.apcatb.2009.05.010.

(23) Brinker C. J., Scherer G. W. *Sol-gel science: The physics and chemistry of sol-gel processing*; Acad. Press: Boston, 2010.

(24) Smarsly, B., Antonietti, M., Wolff, T. Evaluation of the small-angle x-ray scattering of carbons using parametrization methods. *J. Chem. Phys.* **2002**, *116*, 2618–2627, DOI: 10.1063/1.1433463.

(25) Stoeckel, D., Wallacher, D., Zickler, G. A., Perlich, J., Tallarek, U., Smarsly, B. M. Coherent analysis of disordered mesoporous adsorbents using small angle X-ray scattering and physisorption experiments. *Phys. Chem. Chem. Phys.* **2014**, *16*, 6583–6592, DOI: 10.1039/c3cp55072a.

(26) Palenstijn, W. J., Batenburg, K. J., Sijbers, J. Performance improvements for iterative electron tomography reconstruction using graphics processing units (GPUs). *J. Struct. Biol.* **2011**, *176*, 250–253, DOI: 10.1016/j.jsb.2011.07.017.

(27) van Aarle, W., Palenstijn, W. J., Beenhouwer, J. de, Altantzis, T., Bals, S., Batenburg, K. J., Sijbers, J. The ASTRA Toolbox: A platform for advanced algorithm development in electron tomography. *Ultramicroscopy* **2015**, *157*, 35–47, DOI: 10.1016/j.ultramic.2015.05.002.

(28) van Aarle, W., Palenstijn, W. J., Cant, J., Janssens, E., Bleichrodt, F., Dabravolski, A., Beenhouwer, J. de, Joost Batenburg, K., Sijbers, J. Fast and flexible X-ray tomography using the ASTRA toolbox. *Opt. Express* **2016**, *24*, 25129–25147, DOI: 10.1364/OE.24.025129.

(29) Hildebrand, T., Rüegsegger, P. A new method for the model-independent assessment of thickness in three-dimensional images. *J. Microsc.* **1997**, *185*, 67–75, DOI: 10.1046/j.1365-2818.1997.1340694.x.

(30) Cheng, X., Föhst, S., Redenbach, C., Schladitz, K. Detecting Branching Nodes of Multiply Connected 3D Structures. In *Mathematical Morphology and its Applications to Signal and Image Processing: 14th international symposium, ISMM 2019 Saarbrücken, Germany, July 8-10, 2019 proceedings*; Burgeth, B., Kleefeld, A., Naegel, B., Passat, N., Perret, B., Eds.;

Springer International Publishing: Cham, 2019; Vols. 11564, pp. 441–455.
(31) Schmidt-Rohr, K. Simulation of small-angle scattering curves by numerical Fourier transformation. *J. Appl. Crystallogr.* **2007**, *40*, 16–25, DOI: 10.1107/S002188980604550X.
(32) Eric Prates da Costa. *tomo2scattering: python script to calculate a scattering curve from a tomographic reconstruction*. https://gitlab.com/EPDC/tomo2scattering, DOI: 10.5281/zenodo.8054538.
(33) Thommes, M., Cychosz, K. A. Physical adsorption characterization of nanoporous materials: progress and challenges. *Adsorption* **2014**, *20*, 233–250, DOI: 10.1007/s10450-014-9606-z.
(34) Thommes, M., Kaneko, K., Neimark, A. V., Olivier, J. P., Rodriguez-Reinoso, F., Rouquerol, J., Sing, K. S. Physisorption of gases, with special reference to the evaluation of surface area and pore size distribution (IUPAC Technical Report). *Pure Appl. Chem.* **2015**, *87*, 1051–1069, DOI: 10.1515/pac-2014-1117.
(35) Thommes, M., Smarsly, B., Groenewolt, M., Ravikovitch, P. I., Neimark, A. V. Adsorption hysteresis of nitrogen and argon in pore networks and characterization of novel micro- and mesoporous silicas. *Langmuir* **2006**, *22*, 756–764, DOI: 10.1021/la051686h.
(36) Kleitz, F., Bérubé, F., Guillet-Nicolas, R., Yang, C.-M., Thommes, M. Probing Adsorption, Pore Condensation, and Hysteresis Behavior of Pure Fluids in Three-Dimensional Cubic Mesoporous KIT-6 Silica. *J. Phys. Chem. C* **2010**, *114*, 9344–9355, DOI: 10.1021/jp909836v.
(37) Weyland, M., Midgley, P. A., Thomas, J. M. Electron Tomography of Nanoparticle Catalysts on Porous Supports: A New Technique Based on Rutherford Scattering. *J. Phys. Chem. B* **2001**, *105*, 7882–7886, DOI: 10.1021/jp011566s.
(38) Kübel, C., Voigt, A., Schoenmakers, R., Otten, M., Su, D., Lee, T.-C., Carlsson, A., Bradley, J. Recent advances in electron tomography: TEM and HAADF-STEM tomography for materials science and semiconductor applications. *Microsc. Microanal.* **2005**, *11*, 378–400, DOI: 10.1017/S1431927605050361.
(39) Stoeckel, D., Kübel, C., Hormann, K., Höltzel, A., Smarsly, B. M., Tallarek, U. Morphological analysis of disordered macroporous-mesoporous solids based on physical reconstruction by nanoscale tomography. *Langmuir* **2014**, *30*, 9022–9027, DOI: 10.1021/la502381m.

For table of contents only

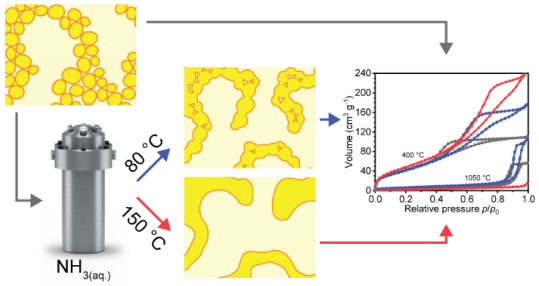

4 Fazit und Ausblick

Die vorliegende Arbeit beschäftigt sich mit der Synthese und Charakterisierung ungeordnet mesoporöser, CeO_2-basierter OSMs zur Anwendung in der TWC. Schwerpunkt war hierbei die systematische Analyse der Wechselwirkungen zwischen Syntheseparametern und resultierender Mesoporenmorphologie.

Im Rahmen dessen wurde ein literaturbekanntes Hydrothermalsyntheseverfahren für CeO_2 mit hoher spezifischer Oberfläche und thermischer Stabilität erfolgreich auf ein quaternäres Mischoxid der Zusammensetzung $Ce_{0.18}Zr_{0.64}Y_{0.15}La_{0.03}O_{2-\delta}$ übertragen. Daran konnte durch tiefgehende Physisorptionsanalyse – inklusive Hysterese-Scanning Experimenten – in Kombination mit Thermogravimetrischer Analyse gezeigt werden, dass an der Oberfläche befindliche Nitratgruppen insbesondere zu Beginn des in der Synthese durchgeführten Kalzinierungsschrittes Sinterprozesse inhibieren und somit zur Ausbildung eines thermisch stabilen Mesoporennetzwerkes beitragen.

In einer Erweiterung der durchgeführten Synthese wurden die Effekte eines zusätzlichen hydrothermalen Nachbehandlungsschrittes in wässriger Ammoniaklösung untersucht. Es wurde gezeigt, dass dieser sich durch eine Aufweitung der Poren und Porenöffnungen und eine Zunahme der Wandstärken positiv auf die Zugänglichkeit der Mesoporen sowie die thermische Stabilität des Mesoporennetzwerkes auswirkt. Ein höherer pH-Wert der Nachbehandlungslösung verstärkte dabei das Ausmaß dieser Veränderungen. Die verbesserte Zugänglichkeit wurde anhand von Hysterese-Scanning Experimenten und mithilfe elektronentomographischer Rekonstruktionen nachgewiesen. Die in den Rekonstruktionen und der Physisorptionsanalyse beobachteten pH-abhängigen Änderungen im Mesoporenraum ließen sich auf einen zugrundeliegenden Auflöse- und Wiederabscheidungsprozess sowie eine basenkatalysierte Vernetzung der Primärpartikel zurückführen, welche die Ursache für die hohe thermische Stabilität darstellen. Diese neuartigen Einblicke in die Entwicklung des Porenraumes und der Wandstrukturen unter hoher thermischer Belastung zeigen essenzielle Parameter und Schritte in der Herstellung mesoporöser Mischoxide auf und verdeutlichen, wie mit ihrer Hilfe die thermische Stabilität erhöht werden kann.

In der Gesamtheit wurde im Rahmen dieser Arbeit eine für mesoporöse Materialien universell anwendbare systematische Vorgehensweise vorgestellt, die als Leitfaden für eine Analyse von Zusammenhängen zwischen Syntheseparametern und resultierender Mesoporenmorphologie dient. Diese legt ein großes Augenmerk auf die Verknüpfung zwischen Poren und deren damit verbundene Zugänglichkeit, da diese ein kritischer Faktor auf dem Anwendungsgebiet der heterogenen Katalyse ist. Die Schlüsselrolle spielten dabei die durchgeführten Hysterese-Scanning Experimente. Im Zuge einer Studie zur Methodenvalidierung wurde die Interpretation von Hysterese-Scanning Kurven mit elektronentomographischen Rekonstruktionen verglichen. Eine porengrößenabhängige Analyse der Konnektivität der Rekonstruktionen zeigte dabei eine große Übereinstimmung mit den durch die Hysterese-Scans nahegelegten Verknüpfungsverhältnissen. So konnte zu einem tieferen Verständnis der Zusammenhänge zwischen Mesoporennetzwerk und Form der Scanning-Kurven beigetragen und deren Interpretation vereinfacht werden. Auch wenn eine Quantifizierung der Konnektivität noch nicht möglich ist, wurde das Potenzial von Hysterese-Scanning Experimenten zur Anwendung als Routinemethode für die Konnektivitätsanalyse in Mesoporennetzwerken anhand dieser Studie veranschaulicht. Es ist bereits möglich darüber weitreichende Aussagen über die Verknüpfung einzelner Porenpopulationen zu treffen und deren Zugänglichkeit zu beurteilen. Aufgrund dieser Erkenntnisse wurde das Hysterese-Scanning in den Prozess der Eingangscharakterisierung von Rohmaterialien bei Umicore Automotive Catalysts in Hanau integriert.

Basierend auf den gewonnenen Erkenntnissen sind auch neue Forschungsfragen entstanden. Diese betreffen insbesondere die zur Beurteilung der thermischen Stabilität bei hohen Temperaturen durchgeführten synthetischen Alterungen. Eine Abbildung realer Bedingungen im Labormaßstab, wie sie beispielsweise im Abgasstrom eines Ottomotors herrschen, ist äußerst anspruchsvoll. Dennoch könnten die schnell wechselnden Temperaturen und Abgaszusammensetzungen die Materialien stärker beanspruchen und so zu einem schnelleren Kollaps der Poren führen. Ein weiterer Punkt ist, dass die tatsächliche Chemie der Katalysereaktion nicht in den gezeigten Alterungen abgebildet ist. Der Einfluss einer zyklischen Entleerung und Wiederauffüllung des Sauerstoffspeichers sowie potenzieller Exothermien bei der

Umsetzung von Schadstoffen auf den Mesoporenraum und dessen Konnektivität wurden noch nicht untersucht.

Zusammenfassend konnte durch die vorgelegte Arbeit ein tieferes Verständnis über die syntheseparameterabhängige Beschaffenheit und thermische Stabilität des Mesoporenraumes komplexer CeO_2-basierter OSMs erlangt werden. Die gewonnenen Erkenntnisse tragen zur fortschreitenden, gezielten Entwicklung langzeitstabiler Sauerstoffspeicher bei.

5 Literaturverzeichnis

(1) Farrauto, R. J., Deeba, M., Alerasool, S. Gasoline automobile catalysis and its historical journey to cleaner air. *Nat. Catal.* **2019**, *2*, 603–613, DOI: 10.1038/s41929-019-0312-9.

(2) Devaiah, D., Reddy, L. H., Park, S.-E., Reddy, B. M. Ceria–zirconia mixed oxides: Synthetic methods and applications. *Catal. Rev. Sci. Eng.* **2018**, *60*, 177–277, DOI: 10.1080/01614940.2017.1415058.

(3) Umweltbundesamt. *Die europäische Abgas-Gesetzgebung*. https://www.umweltbundesamt.de/themen/verkehr-laerm/emissionsstandards/pkw-leichte-nutzfahrzeuge#die-europaische-abgas-gesetzgebung. Zugriff am 2. Januar 2023.

(4) Umweltbundesamt. *Grenzwerte für Schadstoffemissionen von PKW*, 2016. https://www.umweltbundesamt.de/sites/default/files/medien/376/bilder/dateien/tabelle_grenzwerte_fuer_schadstoffemissionen_von_pkw.pdf. Zugriff am 2. Januar 2023.

(5) Kašpar, J., Fornasiero, P. Nanostructured materials for advanced automotive de-pollution catalysts. *J. Solid State Chem.* **2003**, *171*, 19–29, DOI: 10.1016/S0022-4596(02)00141-X.

(6) Di Monte, R., Kašpar, J. On the Role of Oxygen Storage in Three-Way Catalysis. *Top. Catal.* **2004**, *28*, 47–57, DOI: 10.1023/B:TOCA.0000024333.08447.f7.

(7) eurostat. *New passenger cars by type of motor energy*. road_eqr_carpda, 2022. https://ec.europa.eu/eurostat/databrowser/view/road_eqr_carpda/default/table?lang=en. Zugriff am 3. Januar 2023.

(8) Abanades, S., Haeussler, A., Julbe, A. Synthesis and thermochemical redox cycling of porous ceria microspheres for renewable fuels production from solar-aided water-splitting and CO_2 utilization. *Appl. Phys. Lett.* **2021**, *119*, 23902, DOI: 10.1063/5.0055282.

(9) Boretti, A. Technology Readiness Level of Solar Thermochemical Splitting Cycles. *ACS Energy Lett.* **2021**, 1170–1174, DOI: 10.1021/acsenergylett.1c00181.

(10) Costa Oliveira, F. A., Barreiros, M. A., Haeussler, A., Caetano, A. P. F., Mouquinho, A. I., Oliveira e Silva, P. M., Novais, R. M., Pullar, R. C., Abanades, S. High performance cork-templated ceria for solar thermochemical hydrogen production via two-step water-splitting cycles. *Sustainable Energy Fuels* **2020**, *4*, 3077–3089, DOI: 10.1039/D0SE00318B.

(11) Le Gal, A., Abanades, S. Dopant Incorporation in Ceria for Enhanced Water-Splitting Activity during Solar Thermochemical Hydrogen Generation. *J. Phys. Chem. C* **2012**, *116*, 13516–13523, DOI: 10.1021/jp302146c.

(12) *Grundlagen Verbrennungsmotoren: Funktionsweise, Simulation, Messtechnik,* 5th ed.; Vieweg+Teubner Verlag: Wiesbaden, 2012.

(13) Deutschmann, O., Grunwaldt, J.-D. Abgasnachbehandlung in mobilen Systemen: Stand der Technik, Herausforderungen und Perspektiven. *Chem. Ing. Tech.* **2013**, *85*, 595–617, DOI: 10.1002/cite.201200188.

(14) Kašpar, J., Fornasiero, P., Hickey, N. Automotive catalytic converters: current status and some perspectives. *Catal. Today* **2003**, *77*, 419–449, DOI: 10.1016/S0920-5861(02)00384-X.

(15) Montini, T., Melchionna, M., Monai, M., Fornasiero, P. Fundamentals and Catalytic Applications of CeO_2-Based Materials. *Chem. Rev.* **2016**, *116*, 5987–6041, DOI: 10.1021/acs.chemrev.5b00603.

(16) Zinkevich, M., Djurovic, D., Aldinger, F. Thermodynamic modelling of the cerium–oxygen system. *Solid State Ionics* **2006**, *177*, 989–1001, DOI: 10.1016/j.ssi.2006.02.044.

(17) Trovarelli, A., Llorca, J. Ceria Catalysts at Nanoscale: How Do Crystal Shapes Shape Catalysis? *ACS Catal.* **2017**, *7*, 4716–4735, DOI: 10.1021/acscatal.7b01246.

(18) Madier, Y., Descorme, C., Le Govic, A. M., Duprez, D. Oxygen Mobility in CeO_2 and $CexZr_{(1-x)}O_2$ Compounds: Study by CO Transient Oxidation and $^{18}O/^{16}O$ Isotopic Exchange. *J. Phys. Chem. B* **1999**, *103*, 10999–11006, DOI: 10.1021/jp991270a.

(19) Mamontov, E., Egami, T., Brezny, R., Koranne, M., Tyagi, S. Lattice Defects and Oxygen Storage Capacity of Nanocrystalline Ceria and Ceria-Zirconia. *J. Phys. Chem. B* **2000**, *104*, 11110–11116, DOI: 10.1021/jp0023011.

(20) Kašpar, J., Di Monte, R., Fornasiero, P., Graziani, M., Bradshaw, H., Norman, C. Dependency of the Oxygen Storage Capacity in Zirconia–Ceria Solid Solutions upon Textural Properties. *Top. Catal.* **2001**, *16/17*, 83–87, DOI: 10.1023/A:1016682831177.

(21) Wu, Z., Li, M., Overbury, S. H. On the structure dependence of CO oxidation over CeO_2 nanocrystals with well-defined surface planes. *J. Catal.* **2012**, *285*, 61–73, DOI: 10.1016/j.jcat.2011.09.011.

(22) Aneggi, E., Boaro, M., Leitenburg, C. de, Dolcetti, G., Trovarelli, A. Insights into the redox properties of ceria-based oxides and their implications in catalysis. *J. Alloys Compd.* **2006**, *408-412*, 1096–1102, DOI: 10.1016/j.jallcom.2004.12.113.

(23) Hickey, N., Fornasiero, P., Di Monte, R., Kaspar, J., Graziani, M., Dolcetti, G. A comparative study of oxygen storage capacity over $Ce_{0.6}Zr_{0.4}O_2$ mixed oxides investigated by temperature-programmed reduction and dynamic OSC measurements. *Catal. Lett.* **2001**, *72*, 45–50, DOI: 10.1023/A:1009096106758.

(24) Li, C., Sun, Y., Djerdj, I., Voepel, P., Sack, C.-C., Weller, T., Ellinghaus, R., Sann, J., Guo, Y., Smarsly, B. M., Over, H. Shape-Controlled CeO_2 Nanoparticles: Stability and Activity in the Catalyzed HCl Oxidation Reaction. *ACS Catal.* **2017**, *7*, 6453–6463, DOI: 10.1021/acscatal.7b01618.

(25) Sun, Y., Li, C., Djerdj, I., Khalid, O., Cop, P., Sann, J., Weber, T., Werner, S., Turke, K., Guo, Y., Smarsly, B. M., Over, H. Oxygen storage capacity versus catalytic activity of ceria–zirconia solid solutions in CO and HCl oxidation. *Catal. Sci. Technol.* **2019**, *9*, 2163–2172, DOI: 10.1039/C9CY00222G.

(26) Yao, H. Ceria in automotive exhaust catalysts I. Oxygen storage. *J. Catal.* **1984**, *86*, 254–265, DOI: 10.1016/0021-9517(84)90371-3.

(27) Johnson, M. Cerium dioxide crystallite sizes by temperature-programmed reduction. *J. Catal.* **1987**, *103*, 502–505, DOI: 10.1016/0021-9517(87)90142-4.

(28) Fornasiero, P., Dimonte, R., Rao, G. R., Kaspar, J., Meriani, S., Trovarelli, A., Graziani, M. Rh-Loaded CeO_2-ZrO_2 Solid-Solutions as Highly Efficient Oxygen Exchangers: Dependence of the Reduction Behavior and the Oxygen Storage Capacity on the Structural-Properties. *J. Catal.* **1995**, *151*, 168–177, DOI: 10.1006/jcat.1995.1019.

(29) Rao, G. R., Kašpar, J., Meriani, S., Di Monte, R., Graziani, M. NO decomposition over partially reduced metallized CeO_2-ZrO_2 solid solutions. *Catal. Lett.* **1994**, *24*, 107–112, DOI: 10.1007/BF00807380.

(30) Vlaic, G., Fornasiero, P., Geremia, S., Kašpar, J., Graziani, M. Relationship between the Zirconia-Promoted Reduction in the Rh-Loaded $Ce_{0.5}Zr_{0.5}O_2$ Mixed Oxide and the Zr–O Local Structure. *J. Catal.* **1997**, *168*, 386–392, DOI: 10.1006/jcat.1997.1644.

(31) Di Monte, R., Kašpar, J. Nanostructured CeO_2–ZrO_2 mixed oxides. *J. Mater. Chem.* **2005**, *15*, 633–648, DOI: 10.1039/b414244f.

(32) Vidmar, P., Fornasiero, P., Kašpar, J., Gubitosa, G., Graziani, M. Effects of Trivalent Dopants on the Redox Properties of $Ce_{0.6}Zr_{0.4}O_2$ Mixed Oxide. *J. Catal.* **1997**, *171*, 160–168, DOI: 10.1006/jcat.1997.1784.

(33) Yashima, M., Arashi, H., Kakihana, M., Yoshimura, M. Raman Scattering Study of Cubic-Tetragonal Phase Transition in $Zr_{1-x}Ce_xO_2$ Solid Solution. *J. Am. Ceram. Soc.* **1994**, *77*, 1067–1071, DOI: 10.1111/j.1151-2916.1994.tb07270.x.

(34) Otero, G. S., Lustemberg, P. G., Prado, F., Ganduglia-Pirovano, M. V. Relative Stability of Near-Surface Oxygen Vacancies at the CeO_2(111) Surface upon Zirconium Doping. *J. Phys. Chem. C* **2020**, *124*, 625–638, DOI: 10.1021/acs.jpcc.9b09433.

(35) Si, R., Zhang, Y.-W., Wang, L.-M., Li, S.-J., Lin, B.-X., Chu, W.-S., Wu, Z.-Y., Yan, C.-H. Enhanced Thermal Stability and Oxygen Storage Capacity for $Ce_xZr_{1-x}O_2$ (x = 0.4−0.6) Solid Solutions by Hydrothermally Homogenous Doping of Trivalent Rare Earths. *J. Phys. Chem. C* **2007**, *111*, 787–794, DOI: 10.1021/jp0630875.

(36) Aneggi, E., Leitenburg, C. de, Dolcetti, G., Trovarelli, A. Promotional effect of rare earths and transition metals in the combustion of diesel soot over CeO_2 and CeO_2–ZrO_2. *Catal. Today* **2006**, *114*, 40–47, DOI: 10.1016/j.cattod.2006.02.008.

(37) Krogstad, J. A., Lepple, M., Gao, Y., Lipkin, D. M., Levi, C. G. Effect of Yttria Content on the Zirconia Unit Cell Parameters. *J. Am. Ceram. Soc.* **2011**, *94*, 4548–4555, DOI: 10.1111/j.1551-2916.2011.04862.x.

(38) Guillén-Hurtado, N., Atribak, I., Bueno-López, A., García-García, A. Influence of the cerium precursor on the physico-chemical features and NO to NO_2 oxidation activity of ceria and ceria–zirconia catalysts. *J. Mol. Catal. A: Chem.* **2010**, *323*, 52–58, DOI: 10.1016/j.molcata.2010.03.010.

(39) Pappacena, A., Schermanz, K., Sagar, A., Aneggi, E., Trovarelli, A. Development of a modified co-precipitation route for thermally resistant, high surface area ceria-zirconia based solid solutions. In *Studies in Surface Science and Catalysis Scientific Bases for the Preparation of Heterogeneous Catalysts*; Gaigneaux, E. M., Devillers, M., Hermans, S., Jacobs, P. A., Martens, J. A., Ruiz, P., Eds.; Elsevier, 2010; Vols. 175, pp. 835–838.

(40) Esteves, P., Wu, Y., Dujardin, C., Dongare, M. K., Granger, P. Ceria–zirconia mixed oxides as thermal resistant catalysts for the decomposition of nitrous oxide at high temperature. *Catal. Today* **2011**, *176*, 453–457, DOI: 10.1016/j.cattod.2010.10.068.

(41) Annis, J. W., Fisher, J. M., Thompsett, D., Walton, R. I. Solvothermal Synthesis Routes to Substituted Cerium Dioxide Materials. *Inorganics* **2021**, *9*, 40, DOI: 10.3390/inorganics9060040.

(42) Hirano, M., Hirai, K. Effect of Hydrolysis Conditions on the Direct Formation of Nanoparticles of Ceria–Zirconia Solid Solutions from Acidic Aqueous Solutions. *J. Nanopart. Res.* **2003**, *5*, 147–156, DOI: 10.1023/A:1024482824561.

(43) Ohtake, N., Katoh, M., Sugiyama, S. High thermal-stability ceria synthesized via thermal-hydrolysis route and methane-combustion performance. *J. Ceram. Soc. Japan* **2017**, *125*, 57–61, DOI: 10.2109/jcersj2.16255.

(44) Özkan, E., Hofmann, A., Votsmeier, M., Wang, W., Huang, X., Kübel, C., Badaczewski, F., Turke, K., Werner, S., Smarsly, B. M. Comprehensive Characterization of a Mesoporous Cerium Oxide Nanomaterial with High Surface Area and High Thermal Stability. *Langmuir* **2021**, *37*, 2563–2574, DOI: 10.1021/acs.langmuir.0c02747.

(45) Chuah, G. K., Jaenicke, S., Pong, B. K. The Preparation of High-Surface-Area Zirconia. *J. Catal.* **1998**, *175*, 80–92, DOI: 10.1006/jcat.1998.1980.

(46) Di Monte, R., Kašpar, J., Bradshaw, H., Norman, C. A rationale for the development of thermally stable nanostructured CeO_2-ZrO_2-containing mixed oxides. *J. Rare Earths* **2008**, *26*, 136–140, DOI: 10.1016/S1002-0721(08)60053-8.

(47) Raju, V., Jaenicke, S., Chuah, G.-K. Effect of hydrothermal treatment and silica on thermal stability and oxygen storage capacity of ceria–zirconia. *Appl. Catal., B* **2009**, *91*, 92–100, DOI: 10.1016/j.apcatb.2009.05.010.

(48) Li, H., Zhang, L., Dai, H., He, H. Facile synthesis and unique physicochemical properties of three-dimensionally ordered macroporous magnesium oxide, gamma-alumina, and ceria-zirconia solid solutions with crystalline mesoporous walls. *Inorg. Chem.* **2009**, *48*, 4421–4434, DOI: 10.1021/ic900132k.

(49) Zhang, G., Zhao, Z., Liu, J., Jiang, G., Duan, A., Zheng, J., Chen, S., Zhou, R. Three dimensionally ordered macroporous $Ce_{1-x}Zr_xO_2$ solid solutions for diesel soot combustion. *Chem. Commun.* **2010**, *46*, 457–459, DOI: 10.1039/B915027G.

(50) Cop, P., Maile, R., Sun, Y., Khalid, O., Djerdj, I., Esch, P., Heiles, S., Over, H., Smarsly, B. M. Impact of Aliovalent/Isovalent Ions (Gd, Zr, Pr, and Tb) on the Catalytic Stability of Mesoporous Ceria in the HCl Oxidation Reaction. *ACS Appl. Nano Mater.* **2020**, *3*, 7406–7419, DOI: 10.1021/acsanm.0c00994.

(51) Thommes, M., Kaneko, K., Neimark, A. V., Olivier, J. P., Rodriguez-Reinoso, F., Rouquerol, J., Sing, K. S. Physisorption of gases, with special reference to the evaluation of surface area and pore size distribution (IUPAC Technical Report). *Pure Appl. Chem.* **2015**, *87*, 1051–1069, DOI: 10.1515/pac-2014-1117.

(52) Langmuir, I. The Constitution and Fundamental Properties of Solids and Liquids. Part I. Solids. *J. Am. Chem. Soc.* **1916**, *38*, 2221–2295, DOI: 10.1021/ja02268a002.

(53) Langmuir, I. THE ADSORPTION OF GASES ON PLANE SURFACES OF GLASS, MICA AND PLATINUM. *J. Am. Chem. Soc.* **1918**, *40*, 1361–1403, DOI: 10.1021/ja02242a004.

(54) Brunauer, S., Emmett, P. H., Teller, E. Adsorption of Gases in Multimolecular Layers. *J. Am. Chem. Soc.* **1938**, *60*, 309–319, DOI: 10.1021/ja01269a023.

(55) Barrett, E. P., Joyner, L. G., Halenda, P. P. The Determination of Pore Volume and Area Distributions in Porous Substances. I. Computations from Nitrogen Isotherms. *J. Am. Chem. Soc.* **1951**, *73*, 373–380, DOI: 10.1021/ja01145a126.

(56) Sarkisov, L., Monson, P. A. Modeling of Adsorption and Desorption in Pores of Simple Geometry Using Molecular Dynamics. *Langmuir* **2001**, *17*, 7600–7604, DOI: 10.1021/la015521u.

(57) Rasmussen, C. J., Vishnyakov, A., Thommes, M., Smarsly, B. M., Kleitz, F., Neimark, A. V. Cavitation in metastable liquid nitrogen confined to nanoscale pores. *Langmuir* **2010**, *26*, 10147–10157, DOI: 10.1021/la100268q.

(58) Thommes, M., Smarsly, B., Groenewolt, M., Ravikovitch, P. I., Neimark, A. V. Adsorption hysteresis of nitrogen and argon in pore networks and characterization of novel micro- and mesoporous silicas. *Langmuir* **2006**, *22*, 756–764, DOI: 10.1021/la051686h.

(59) Kube, S. A., Turke, K., Ellinghaus, R., Wallacher, D., Thommes, M., Smarsly, B. M. Pore Size Gradient Effect in Monolithic Silica Mesopore Networks Revealed by In-Situ SAXS Physisorption. *Langmuir* **2020**, *36*, 11996–12009, DOI: 10.1021/acs.langmuir.0c02183.

(60) Cimino, R., Cychosz, K. A., Thommes, M., Neimark, A. V. Experimental and theoretical studies of scanning adsorption–desorption isotherms. *Colloids Surf., A* **2013**, *437*, 76–89, DOI: 10.1016/j.colsurfa.2013.03.025.

(61) Tompsett, G. A., Krogh, L., Griffin, D. W., Conner, W. C. Hysteresis and scanning behavior of mesoporous molecular sieves. *Langmuir* **2005**, *21*, 8214–8225, DOI: 10.1021/la050068y.

(62) Monson, P. A. Understanding adsorption/desorption hysteresis for fluids in mesoporous materials using simple molecular models and classical density functional theory. *Microporous Mesoporous Mater.* **2012**, *160*, 47–66, DOI: 10.1016/j.micromeso.2012.04.043.

(63) Leary, R., Midgley, P. A., Thomas, J. M. Recent advances in the application of electron tomography to materials chemistry. *Acc. Chem. Res.* **2012**, *45*, 1782–1791, DOI: 10.1021/ar3001102.

(64) Ercius, P., Alaidi, O., Rames, M. J., Ren, G. Electron Tomography: A Three-Dimensional Analytic Tool for Hard and Soft Materials Research. *Adv. Mater.* **2015**, *27*, 5638–5663, DOI: 10.1002/adma.201501015.

(65) Hormann, K., Baranau, V., Hlushkou, D., Höltzel, A., Tallarek, U. Topological analysis of non-granular, disordered porous media: determination of pore connectivity, pore coordination, and geometric tortuosity in physically reconstructed silica monoliths. *New J. Chem.* **2016**, *40*, 4187–4199, DOI: 10.1039/C5NJ02814K.

(66) Stoeckel, D., Kübel, C., Loeh, M. O., Smarsly, B. M., Tallarek, U. Morphological Analysis of Physically Reconstructed Silica Monoliths with Submicrometer Macropores: Effect of Decreasing Domain Size on Structural Homogeneity. *Langmuir* **2015**, *31*, 7391–7400, DOI: 10.1021/la5046018.

(67) Hochstrasser, J., Svidrytski, A., Höltzel, A., Priamushko, T., Kleitz, F., Wang, W., Kübel, C., Tallarek, U. Morphology-transport relationships for SBA-15 and KIT-6 ordered mesoporous silicas. *Phys. Chem. Chem. Phys.* **2020**, *22*, 11314–11326, DOI: 10.1039/d0cp01861a.

(68) Couprie, M., Zrour, R. Discrete Bisector Function and Euclidean Skeleton. In *Discrete Geometry for Computer Imagery*; Andres, E., Damiand, G., Eds.; Springer Berlin / Heidelberg: Berlin, Heidelberg, 2005; Vols. 3429, pp. 216–227.

(69) Cheng, X., Föhst, S., Redenbach, C., Schladitz, K. Detecting Branching Nodes of Multiply Connected 3D Structures. In *Mathematical Morphology and its Applications to Signal and Image Processing: 14th international symposium, ISMM 2019 Saarbrücken, Germany, July 8-10, 2019 proceedings*; Burgeth, B., Kleefeld, A., Naegel, B., Passat, N., Perret, B., Eds.; Springer International Publishing: Cham, 2019; Vols. 11564, pp. 441–455.

(70) Hildebrand, T., Rüegsegger, P. A new method for the model-independent assessment of thickness in three-dimensional images. *J. Microsc.* **1997**, *185*, 67–75, DOI: 10.1046/j.1365-2818.1997.1340694.x.

6 Anhang

6.1 Supporting Information:

Development of Pore Morphology During Nitrate Removal by Calcination of Mesoporous $Ce_xZr_{1-x-y-z}Y_yLa_zO_{2-\delta}$ Powders

*Eric Prates da Costa[a,b], Alexander Hofmann[b], Ulrich Göbel[b], Pascal Cop[a], Bernd M. Smarsly[a,c]**

a. Institute of Physical Chemistry, Justus-Liebig University, Heinrich-Buff-Ring 17, 35392 Giessen, Germany.

b. Umicore AG & Co. KG, Rodenbacher Chaussee 4, 63457 Hanau, Germany.

c. Center for Materials Research, Heinrich-Buff-Ring 16, 35392 Giessen, Germany.

KEYWORDS physisorption, mixed oxides, mesoporous, hysteresis scanning

Supporting Information

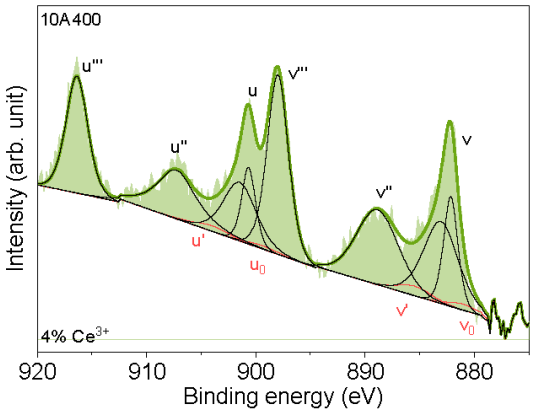

Figure S1. Fitted Ce 3d XPS-spectrum of the fresh sample after calcination at 400 °C for 10 h.

Table S1. Porosity data of the powders.

Sample	S_{BET} (m^2 g^{-1})	V_{Pore} (cm^3 g^{-1})	d_{Pore} (nm)	$L_{Scherrer}$ (nm)
10A400	150	0.14	4.3	3
4A1050	15	0.07	21.4	20

Table S2. Porosity data and crystallite sizes of the heated samples.

Temperature (°C)	S_{BET} (m^2 g^{-1})	V_{Pore} (cm^3 g^{-1})	d_{Pore} (nm)	$L_{Scherrer}$ (nm)
80	125	0.10	4.1	3
250	125	0.11	4.3	3
300	120	0.11	4.3	3
350	155	0.13	4.1	3
400	165	0.13	4.1	3
450	170	0.14	4.1	3
500	170	0.14	4.3	3
550	160	0.14	4.3	3
600	145	0.14	4.6	3
800	90	0.13	5.7	4
1050	30	0.10	11.7	10

Table S3. Comparison of the PSD maxima positions from argon and nitrogen desorption.

Sample	$d_{Pore,\ argon}$ (nm)	$d_{Pore,\ nitrogen}$ (nm)	Δd (nm)
300 °C	4.3	4.9	0.6
600 °C	4.4	5.1	0.7

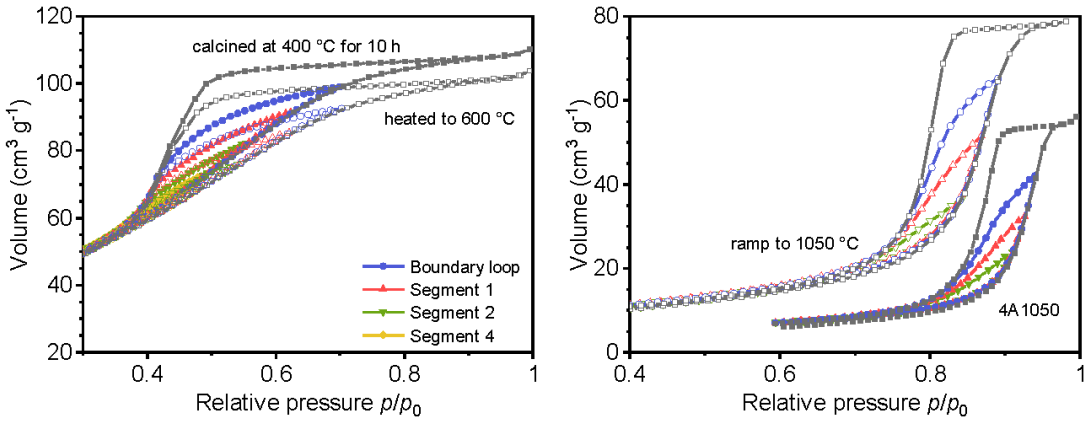

Figure S2. Direct comparison of the hysteresis scans of the sample heated to 600 °C vs. calcined at 400 °C (each after the completion of the nitrate-removal) for 10 h and the sample heated to 1050 °C vs. aged at 1050 °C for 4 h.

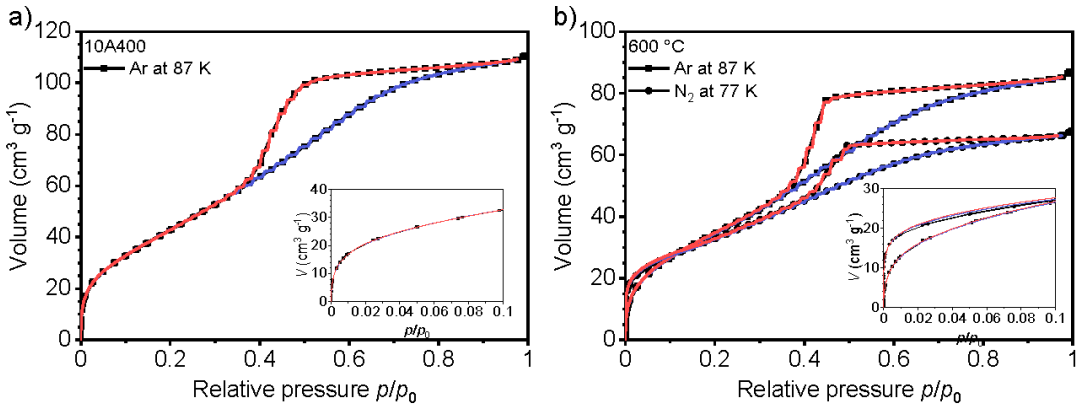

Figure S3. NLDFT-Fit comparison of the fresh sample calcined at 400 °C for 10 h (a) and the sample heated to 600 °C (b) measured with argon and nitrogen.

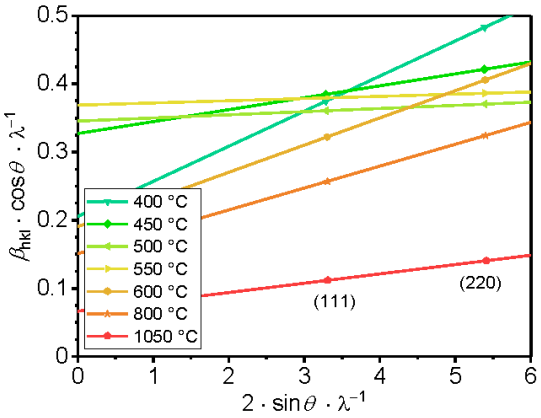

Figure S4. Williamson-Hall-plot obtained from the separable (111) and (220) reflections.

6.2 Supporting Information:

Effects of Hydrothermal Treatment on Mesopore Structure and Connectivity in Doped Ceria Zirconia Mixed Oxides

Eric Prates da Costa[a,b], *Xiaohui Huang*[c,e], *Christian Kübel*[c,d,e], *Xiaoyin Cheng*[f], *Katja Schladitz*[f], *Alexander Hofmann*[b], *Ulrich Göbel*[b], *Bernd M. Smarsly*[a,g]*

a. Institute of Physical Chemistry, Justus-Liebig University, Heinrich-Buff-Ring 17, 35392 Giessen, Germany.

b. Umicore AG & Co. KG, Rodenbacher Chaussee 4, 63457 Hanau, Germany.

c. Institute of Nanotechnology, Karlsruhe Institute of Technology, Hermann-von-Helmholtz Platz 1, 76344 Eggenstein-Leopoldshafen, Germany.

d. Karlsruhe Nano Micro Facility (KNMF), Karlsruhe Institute of Technology, Hermann-von-Helmholtz Platz 1, 76344 Eggenstein-Leopoldshafen, Germany.

e. Department of Materials and Earth Sciences, Technical University Darmstadt, Alarich-Weiss-Str. 2, 64287 Darmstadt, Germany.

f. Fraunhofer-Institut für Techno- und Wirtschaftsmathematik, Fraunhofer-Platz 1, 67663 Kaiserslautern, Germany.

g. Center for Materials Research, Heinrich-Buff-Ring 16, 35392 Giessen, Germany.

KEYWORDS physisorption, ceria, zirconia, mixed oxides, mesoporous, hysteresis scanning, scanning transmission electron microscopy, electron tomography

```python
import porespy as ps
from skimage import io
from skimage import util
from skimage.util import img_as_ubyte
import numpy as np


def find_particle_outline(file_path, radius):
    # import the image file
    image = io.imread(file_path).astype(bool)
    outline = np.zeros(image.shape, dtype=bool)

    # for every slice in the image, determine the outline and add it to
      the slice
    for slice_index in range(image.shape[0]):
        outline[slice_index] = ps.tools.find_outer_region(
            util.invert(image[slice_index]), radius) + image[slice_index]

    io.imsave(f'border_{file_path}', img_as_ubyte(outline))


if __name__ == '__main__':
    # run the outline determination with the file path and radius as
      parameters
    find_particle_outline('your path goes here', 20)
```

Listing S1. Python program used to isolate the pore space from the outer void space.

Table S1. Angular ranges of the collected tils series.

	noHAAT		HAAT	
Parameter	400 °C	1050 °C	400 °C	1050 °C
Min. tilt angle (°)	-74.00	-68.00	-76.00	-76.00
Max. tilt angle (°)	+76.00	+74.00	+74.00	+70.00
Magnification	225kx	225kx	57kx	57kx
Alignment error (px)	0.386	0.596	0.423	0.660

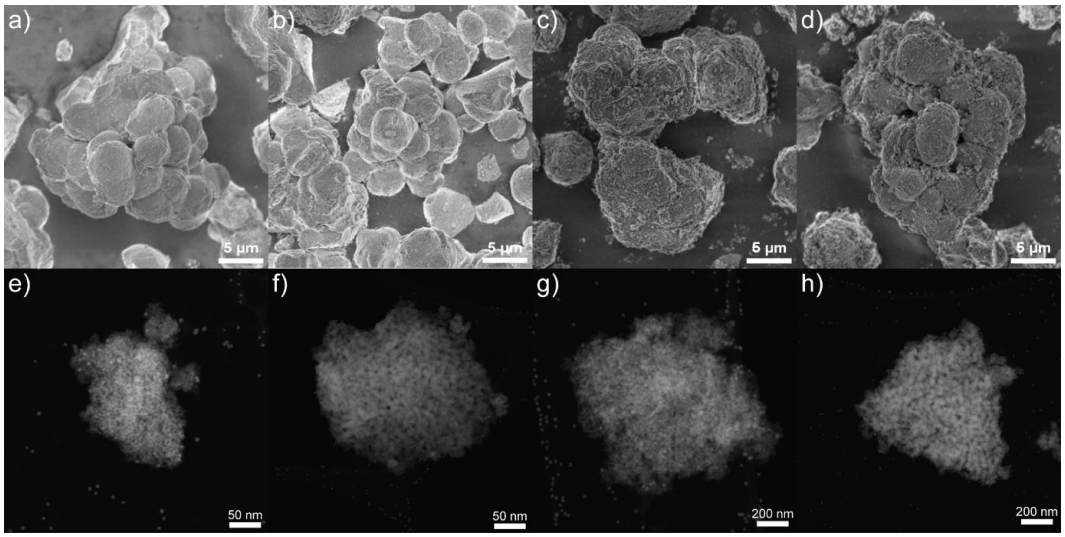

Figure S1. SEM (a-d) and STEM (e-h) images of the investigated materials. a) and e) 400noHAAT; b) and f) 1050noHAAT; c) and g) 400HAAT; d) and h) 1050HAAT.

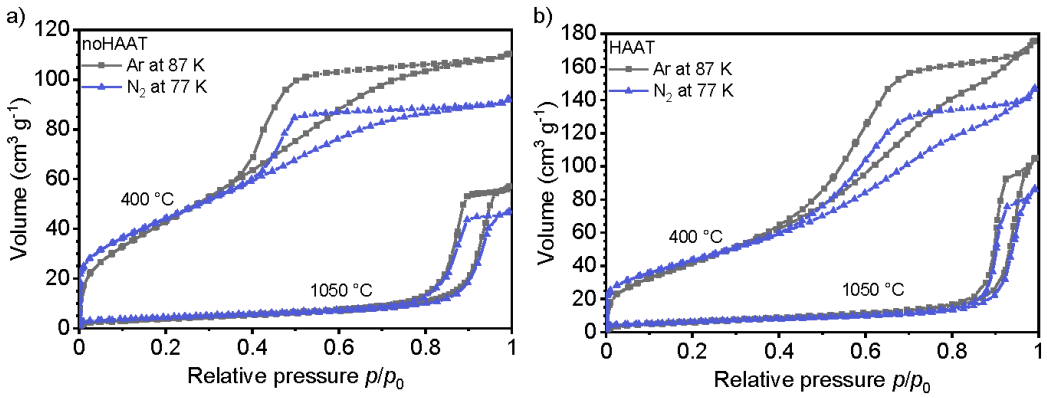

Figure S2. Comparison of Ar and N2 physisorption isotherms.

Figure S2 shows that the measured nitrogen isotherms are like the argon isotherms type IV isotherms. The calcined materials (400 °C) exhibit a H2 hysteresis loop and the aged materials (1050 °C) a H1 hysteresis loop. The agreement of isotherm and hysteresis types verifies the integrity of the obtained data. The most notable is the difference in the total adsorbed volume, which results from different liquid phase densities and are hence to be expected. Another difference is to be found in the adsorbed volume at low relative pressures ($p/p_0 < 0.1$), which

corresponds to the range where micropore filling occurs. However, especially in this range the quadrupole moment of the nitrogen molecule affects the orientation of adsorbed nitrogen and hence introduces inaccuracies in the characterization of micropores.[1]

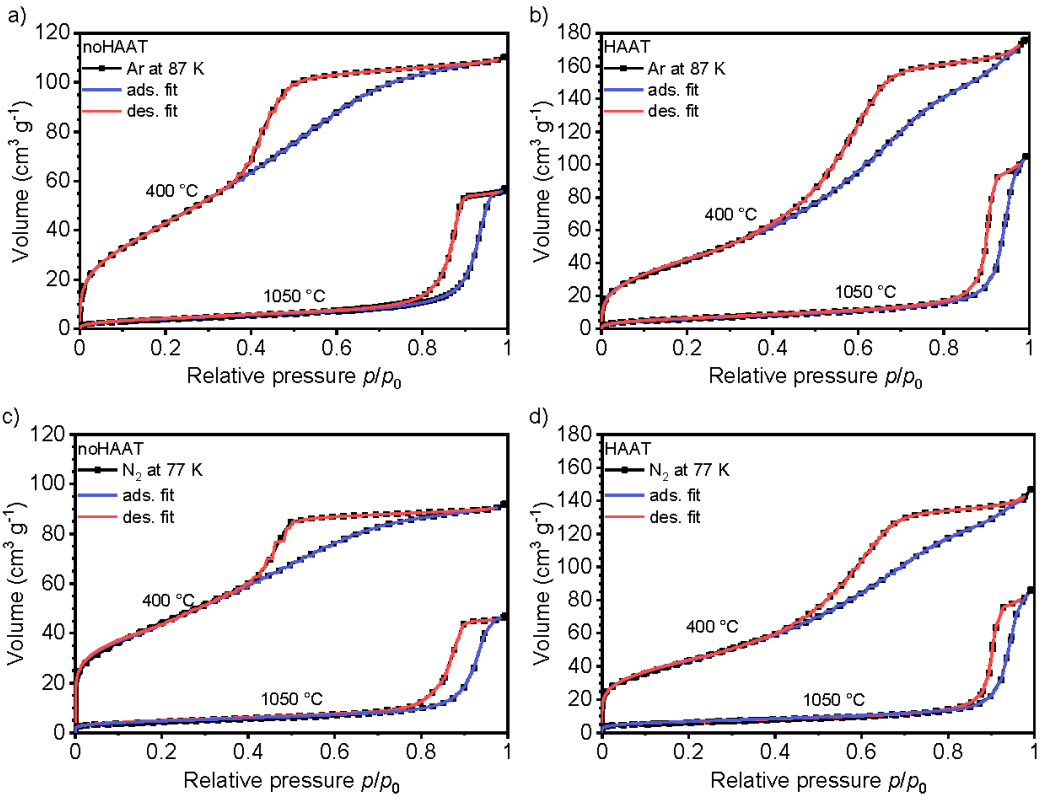

Figure S3. NLDFT-fit comparisons.

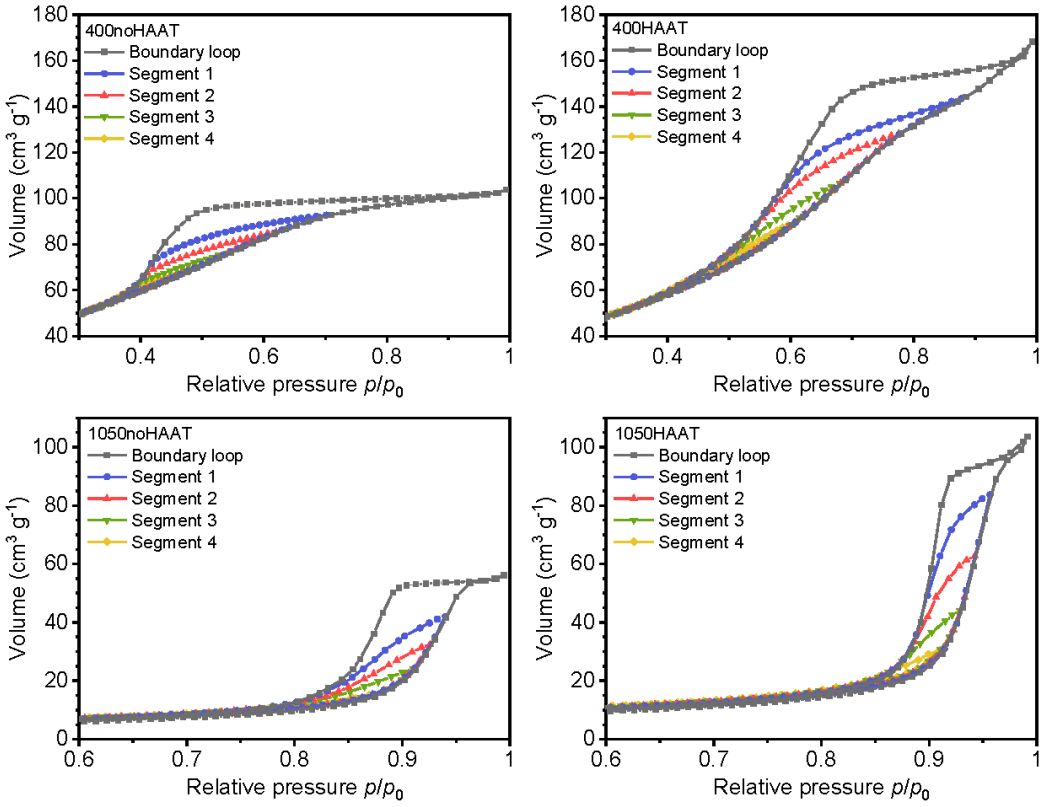

Figure S4. Comparison of hysteresis loops with all adsorption branches included.

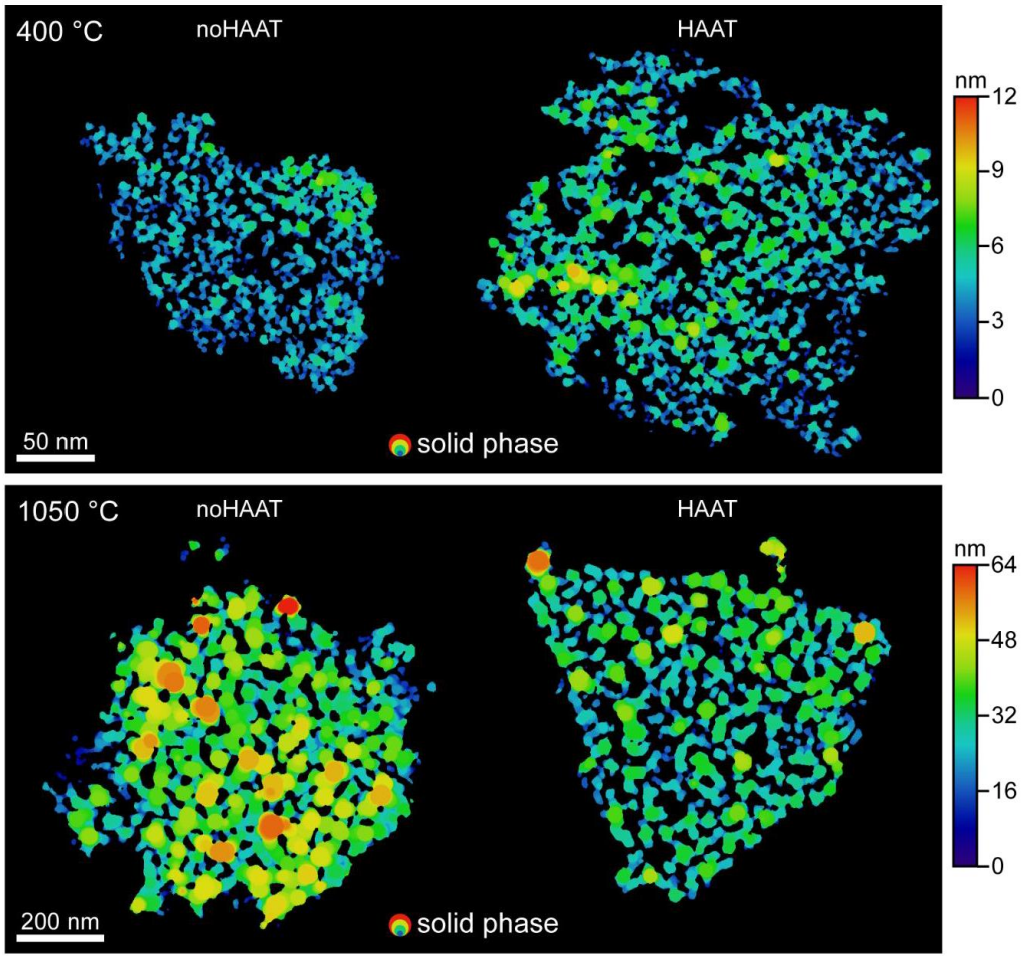

Figure S5. Slices through the 3D reconstructions showing the local thickness of the materials' solid phase.

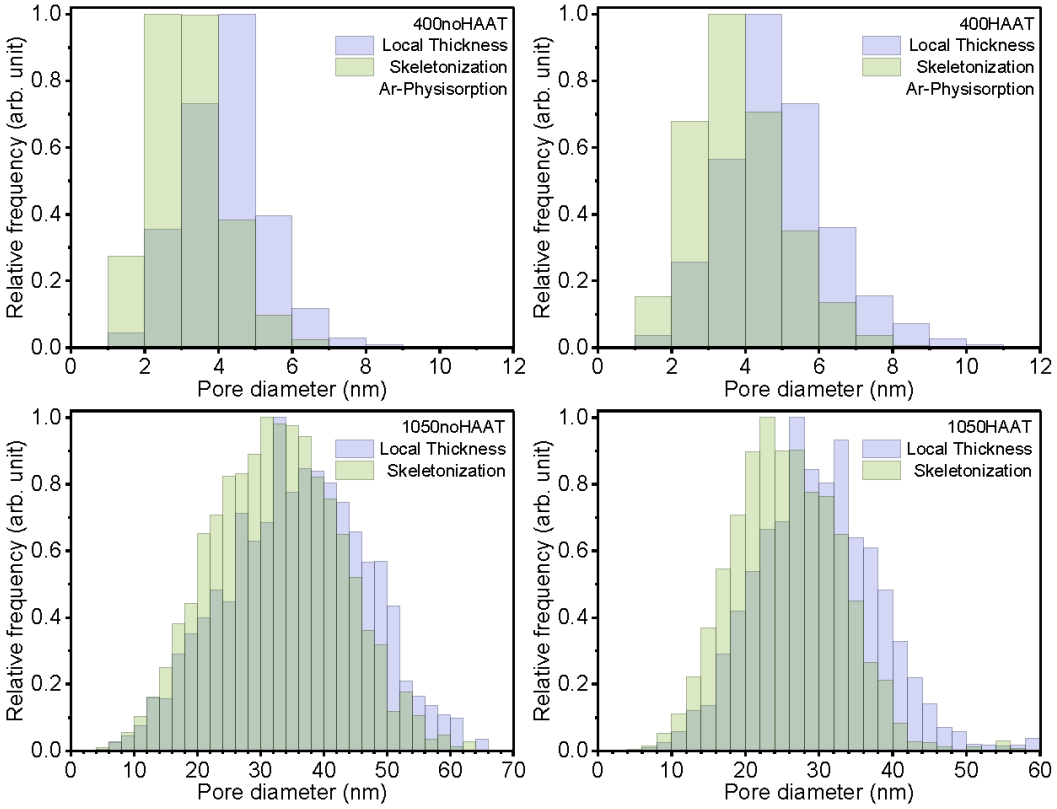

Figure S6. Comparison of wall size distributions determined by local thickness and skeletonization.

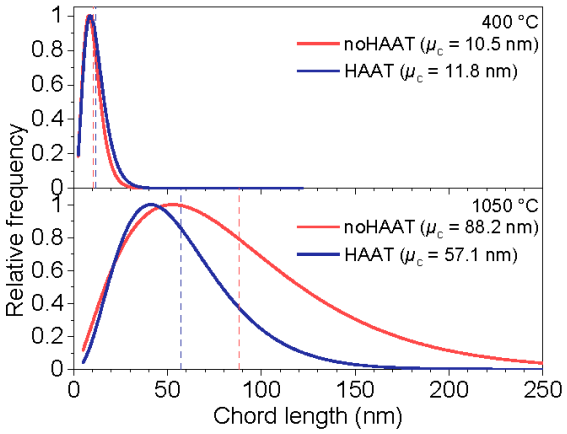

Figure S7. k-gamma fits of the solid phase CLDs.

Table S2. Summary of structural properties.

	noHAAT		HAAT	
Parameter	400 °C	1050 °C	400 °C	1050 °C
S_{BET} (m^2 g^{-1})	150	13	145	20
V_{Pore} (cm^3 g^{-1})	0.14	0.07	0.21	0.13
$d_{Pore, Phys.}$ (nm)	4.3	21.4	5.3	22.1
$d_{Pore, LocThk.}$ (nm)	5.3	22	6.8	26
$d_{Pore, Skel.}$ (nm)	4.2	19	5.2	24
$\mu_{c, Pore}$ *(nm)*	9.9	22.6	11.0	50.4
$L_{Scherrer}$ (nm)	3	20	3	19
$d_{Wall, LocThk.}$ (nm)	4.2	36	4.9	30
$d_{Wall, Skel.}$ (nm)	3.0	32	3.8	26
$\mu_{c, Wall}$ *(nm)*	10.5	88.2	11.8	57.1

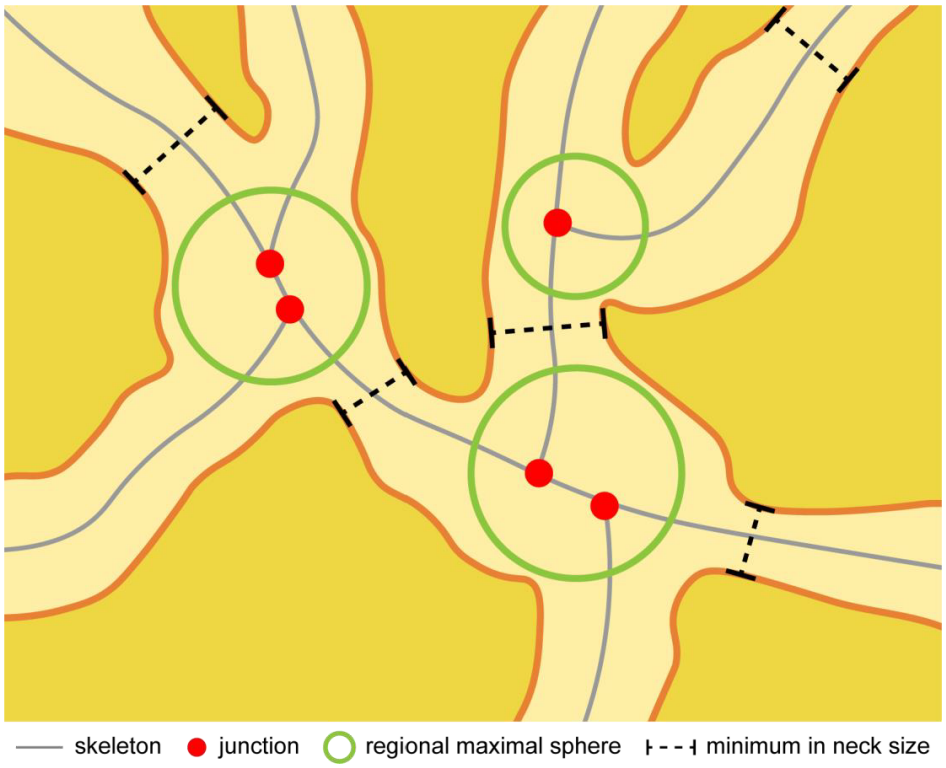

Figure S8. Schematic representation of the pore space and the skeletonization-based neck size analysis.

Neck Size Analysis

The neck size analysis was performed on the basis of the connectivity analysis by Cheng et al.[2], where a set of regional maximal spheres (representing the pores) is determined to obtain a more precise coordination number than by a junction based procedure. To determine the neck sizes of the pores, the branches are assigned to the spheres if exactly one of their end points is located within one sphere. This results in a dataset where every sphere has a list of branches penetrating the sphere's surface, connecting it to a neighboring pore. To obtain the neck size of each branch assigned to a pore, the minimum in the local thickness – sampled along the branch – is determined resulting in a list of neck sizes for each pore, which can be further analyzed. A schematic illustration of the process is shown in Figure S8.

References

(1) Schlumberger, C.; Thommes, M. Characterization of Hierarchically Ordered Porous Materials by Physisorption and Mercury Porosimetry—A Tutorial Review. *Adv. Mater. Interfaces* **2021**, *8*, 2002181. DOI: 10.1002/admi.202002181.

(2) Cheng, X.; Föhst, S.; Redenbach, C.; Schladitz, K. Detecting Branching Nodes of Multiply Connected 3D Structures. In *Mathematical Morphology and its Applications to Signal and Image Processing: 14th international symposium, ISMM 2019 Saarbrücken, Germany, July 8-10, 2019 proceedings*; Burgeth, B., Kleefeld, A., Naegel, B., Passat, N., Perret, B., Eds.; Springer International Publishing: Cham, 2019; Vols. 11564, pp. 441–455.

6.3 Supporting Information:

Tuning Mesopore Accessibility of High Surface Area Doped Ceria-zirconia Mixed Oxides by Hydrothermal Posttreatment

Eric Prates da Costa[a,b], *Xiaohui Huang*[c,e], *Christian Kübel*[c,d,e], *Xiaoyin Cheng*[f], *Katja Schladitz*[f], *Alexander Hofmann*[b], *Ulrich Göbel*[b], *Bernd M. Smarsly*[a,g]*

a. Institute of Physical Chemistry, Justus-Liebig University, Heinrich-Buff-Ring 17, 35392 Giessen, Germany.

b. Umicore AG & Co. KG, Rodenbacher Chaussee 4, 63457 Hanau, Germany.

c. Institute of Nanotechnology, Karlsruhe Institute of Technology, Hermann-von-Helmholtz Platz 1, 76344 Eggenstein-Leopoldshafen, Germany.

d. Karlsruhe Nano Micro Facility (KNMF), Karlsruhe Institute of Technology, Hermann-von-Helmholtz Platz 1, 76344 Eggenstein-Leopoldshafen, Germany.

e. Department of Materials and Earth Sciences, Technical University Darmstadt, Alarich-Weiss-Str. 2, 64287 Darmstadt, Germany.

f. Fraunhofer-Institut für Techno- und Wirtschaftsmathematik, Fraunhofer-Platz 1, 67663 Kaiserslautern, Germany.

g. Center for Materials Research, Heinrich-Buff-Ring 16, 35392 Giessen, Germany.

Supporting Information

Table S1. Electron Tomography Tilt Ranges, Alignment Error, and Reconstruction Resolution.

	Tilt angle			
Sample	Min. (°)	Max. (°)	Alignment error (px)	Pixel size (nm)
400AT80/9.0	-74.00	74.00	0.651	0.28
1050AT80/9.0	-76.0	74.0	0.448	0.80
400AT150/10.9	-76.0	76.0	0.659	0.34

Table S2. Elemental Compositions of the Synthesized Powders as Determined by ICP-OES.

Sample	Composition
noAT	$Ce_{0.20}Zr_{0.63}Y_{0.14}La_{0.03}O_{2-\delta}$
AT80/-0.2	$Ce_{0.22}Zr_{0.77}Y_{0.00}La_{0.00}O_{2-\delta}$
AT80/6.9	$Ce_{0.21}Zr_{0.63}Y_{0.14}La_{0.03}O_{2-\delta}$
AT80/9.0	$Ce_{0.21}Zr_{0.62}Y_{0.14}La_{0.03}O_{2-\delta}$
AT80/10.9	$Ce_{0.19}Zr_{0.63}Y_{0.15}La_{0.03}O_{2-\delta}$
AT80/11.3	$Ce_{0.21}Zr_{0.63}Y_{0.14}La_{0.03}O_{2-\delta}$
AT150/10.9	$Ce_{0.19}Zr_{0.64}Y_{0.14}La_{0.03}O_{2-\delta}$

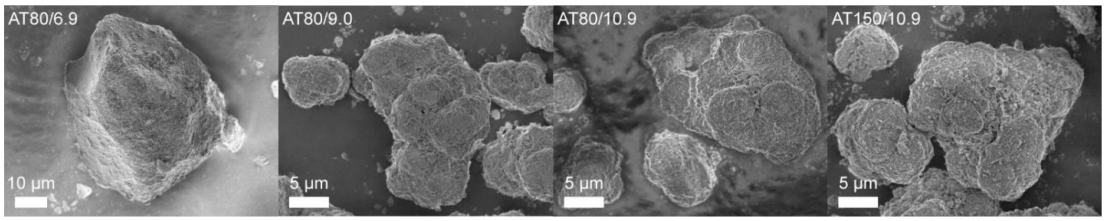

Figure S1. SEM images showing the spherical secondary structure of the synthesized powders.

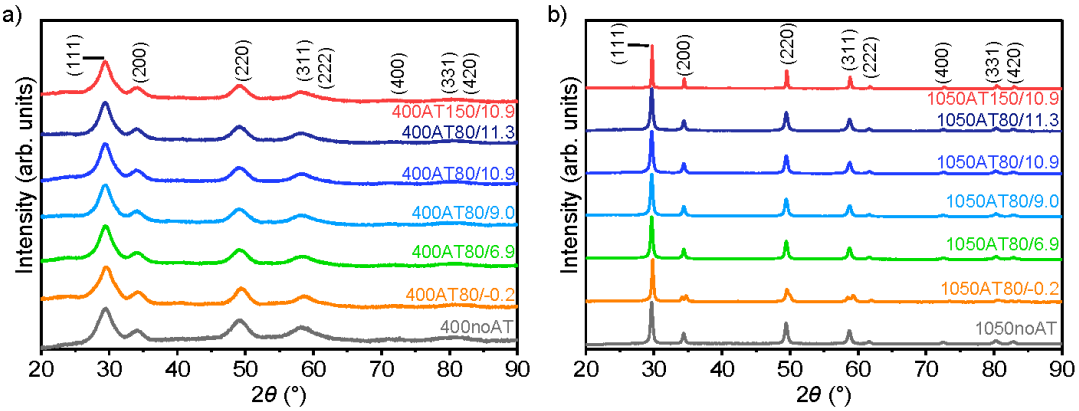

Figure S2. X-ray diffraction patterns of the synthesized powders.

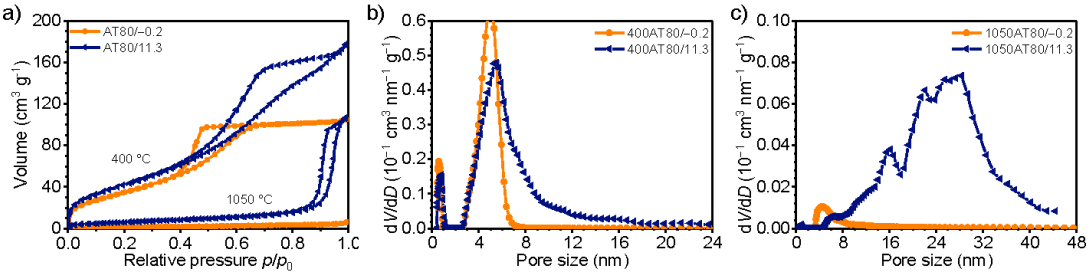

Figure S3. (a) Ar-physisorption isotherms (T = 87 K) of the sample treated under acidic conditions and the sample treated at pH 11.3. (b) Corresponding adsorption-based pore size distributions obtained via NLDFT-analysis after calcination at 400 °C and after aging at 1050 °C (c).

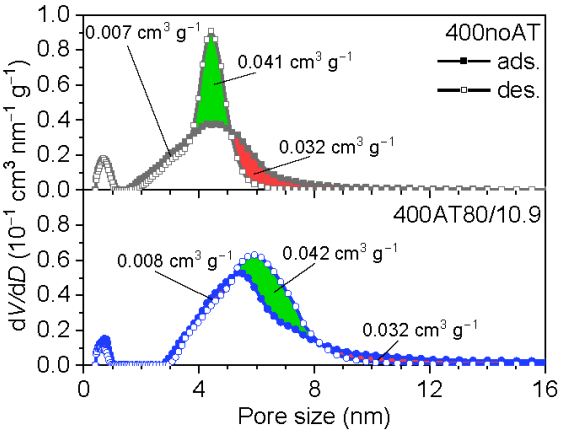

Figure S4. Differences between adsorption- and desorption-based pore size distributions obtained via NLDFT-analysis of the Ar-physisorption isotherms (T = 87 K).

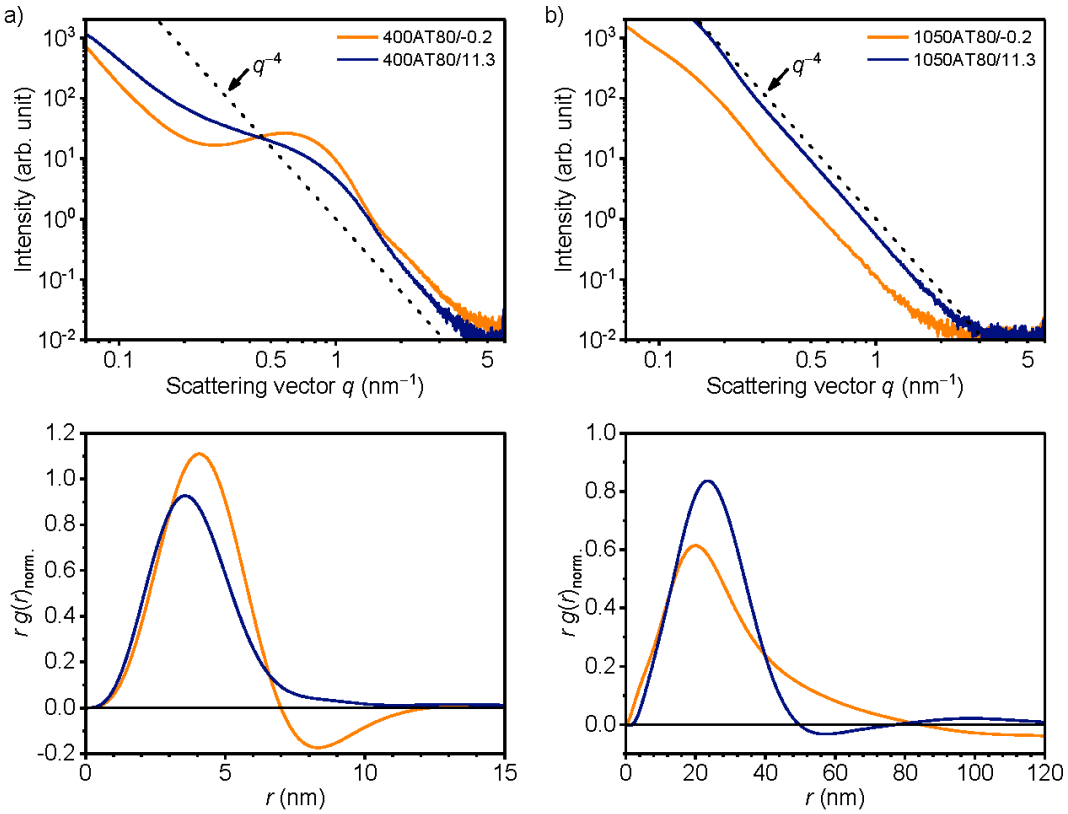

Figure S5. SAXS curves and calculated CLDs of the samples subjected to aftertreatment at different pH at 80 °C after calcination at 400 °C (a) and aging at 1050 °C (b).

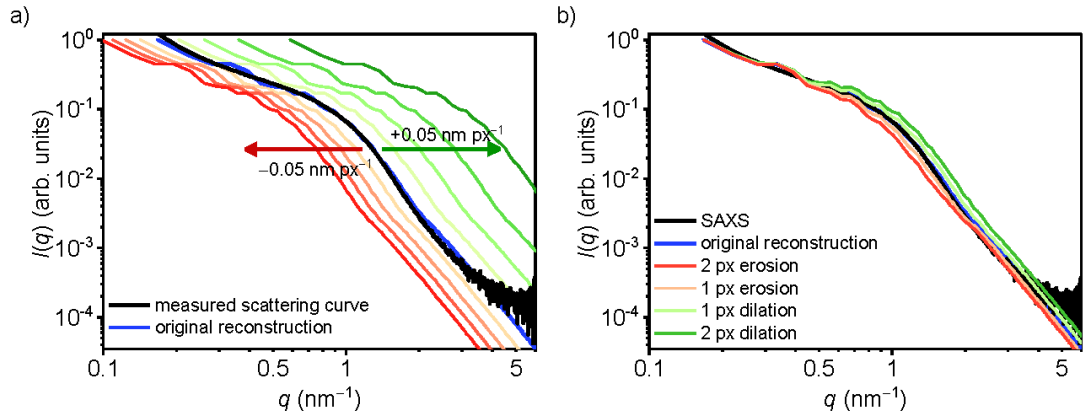

Figure S6. Simulated scattering curves calculated from the electron tomography reconstruction of the sample 400AT80/9.0. (a) Resulting scattering curves of the same reconstruction with a stepwise decrease or increase of the pixel size. (b) Simulated scattering curves of modified reconstructions with the same pixel size but after application of an erosion or dilation filter, removing or adding up to two voxels from or to the solid phase.

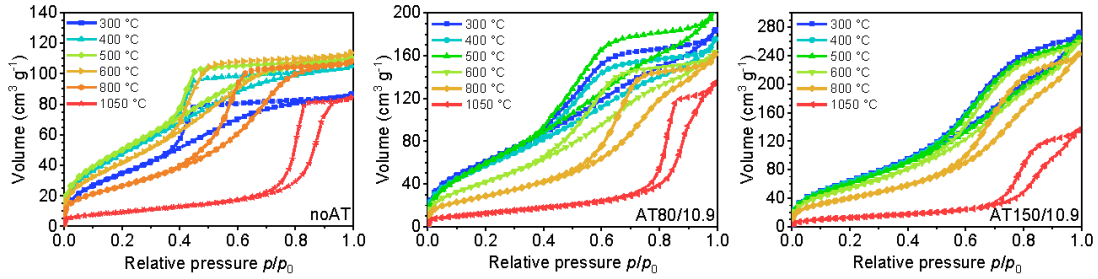

Figure S7. Ar-physisorption isotherms (T = 87 K) for the samples heated to different temperatures during calcination of the dried materials: (a) noAT, (b) AT80/10.9, and (c) AT150/10.9.

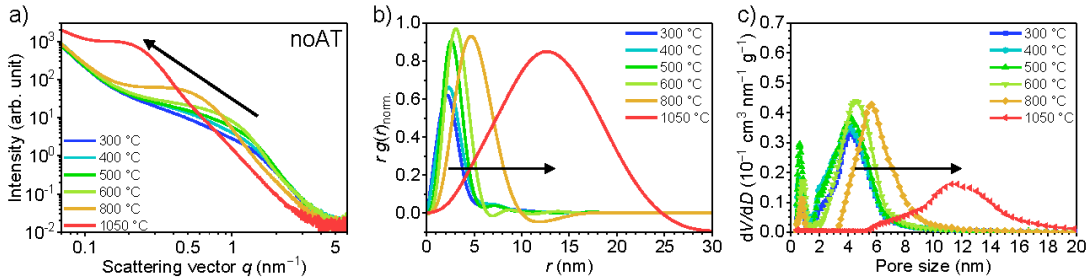

Figure S8. (a) SAXS curves, (b) calculated CLDs, and (c) corresponding pore size distributions obtained from Ar-physisorption (T = 87 K) for different temperatures during calcination of the dried material without additional hydrothermal aftertreatment (noAT).

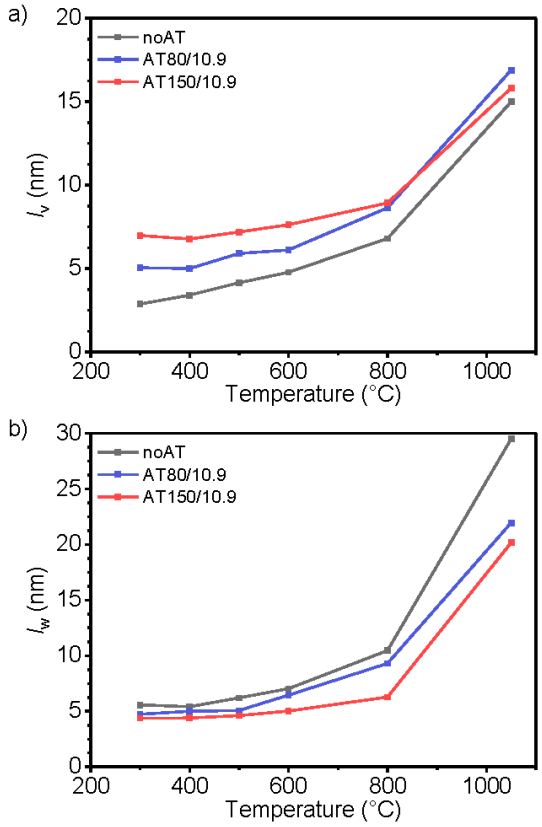

Figure S9. Mean pore and wall sizes according to the CLD analysis of the SAXS data.

Table S3. Mean Pore and Wall Sizes Calculated from the CLD of the Dried Powder noAT.

ϑ (°C)	V_{Pore} (cm^3 g^{-1})	φ_V	l_p (nm)	l_w (nm)	l_v (nm)
300	0.33	0.61	2.68	4.37	6.97
400	0.32	0.61	2.66	4.38	6.76
500	0.32	0.61	2.81	4.61	7.18
600	0.31	0.60	3.02	5.01	7.61
800	0.29	0.59	3.68	6.27	8.93
1050	0.16	0.44	8.86	20.16	15.81

Table S4. Mean Pore and Wall Sizes Calculated from the CLD of the Dried Powder AT80/10.9.

ϑ (°C)	V_{Pore} (cm^3 g^{-1})	φ_V	l_p (nm)	l_w (nm)	l_v (nm)
300	0.33	0.61	2.68	4.37	6.97
400	0.32	0.61	2.66	4.38	6.76
500	0.32	0.61	2.81	4.61	7.18
600	0.31	0.60	3.02	5.01	7.61
800	0.29	0.59	3.68	6.27	8.93
1050	0.16	0.44	8.86	20.16	15.81

Table S5. Mean Pore and Wall Sizes Calculated from the CLD of the Dried Powder AT150/10.9

ϑ (°C)	V_{Pore} (cm^3 g^{-1})	φ_V	l_p (nm)	l_w (nm)	l_v (nm)
300	0.33	0.61	2.68	4.37	6.97
400	0.32	0.61	2.66	4.38	6.76
500	0.32	0.61	2.81	4.61	7.18
600	0.31	0.60	3.02	5.01	7.61
800	0.29	0.59	3.68	6.27	8.93
1050	0.16	0.44	8.86	20.16	15.81